UNIVERSITY OF STRATHCLYDE
Biomedical Engineering

OLIGONUCLEOTIDE BIOSENSING APPLICATIONS OF DISTRIBUTED FEEDBACK LASERS AND SILVER NANOPARTICLES

USING LASERS & SILVER TO FIND BROKEN HEARTS

Glenn McConnell

A thesis presented in fulfilment of the requirements for the degree of
Doctor of Engineering

SEPTEMBER 2019

DECLARATION OF AUTHORSHIP

This thesis is the result of the author's original research. It has been composed by the author and has not been previously submitted for examination which has led to the award of a degree.

The copyright of this thesis belongs to the author under the terms of the United Kingdom Copyright Acts as qualified by University of Strathclyde Regulation 3.50. Due acknowledgement must always be made of the use of any material contained in, or derived from, this thesis.

Name:

Glenn McConnell

Signed:

ACKNOWLEDGEMENTS

The work reported in this thesis was built on the foundations of a thorough investigation by A.M. Haughey in her 2014 thesis, alongside continued support and guidance from others here at the University of Strathclyde. With special mentions to J. Hernsdorf, B. Guilhabert, M. Dawson, L. Maclellan, J Carriera and M. Rodriguez in the Institute of Photonics; the input from R. Black and M. Giardini of the Biomedical Engineering department as well as C. McInness for all her organisational effort with the EngD cohort. O. Kanibolotsky, L. Reichenbach, S. Mabbott and D. Graham, at the time members of the Pure and Applied Chemistry department here at Strathclyde, were also notable contributors to the work presented here. I think it also goes without saying the credit both my supervisors, Drs Glenn Burley and Nicolas Laurand, deserve for their help and guidance (and patience) over the past 3-4 years, it hasn't been easy to make sense of all that's going on in a multidisciplinary project such as this and their experience in their respective fields was a great resource from which to draw insight into the underpinning concepts of the technology. I would probably have broken down and thrown in the towel if it wasn't for the company, care and guidance I've received from a great bunch of people that I've met through my 9 years studying here at Strathclyde (probably 9 and a half by now). Living here in Glasgow, in ways big and small, there was never a dull day.

This work was funded by the EPSRC grant number EP/F50036X/1 and dedicated to my Mother Shirley for raising me with the drive to achieve this milestone and the many more in my future.

T.I.G.

October 2017

P.S. Its now September 2019 and I’m still working on this, I’ve overestimated how easily I could complete a postgrad level thesis could while sofa surfing as a homeless unemployed Doctoral candidate. Its been some interesting albeit much less scientific research.

P.P.S. Its now March 2020, everything’s approved, due to the Corona virus pandemic we can’t hand in hardbound copies till things calm down and I won’t graduate till Autumn.

ABSTRACT

Point of Care devices have helped extend the reach of medical services and improved turnaround times for many traditional laboratory tests. Their development necessitates the development and miniaturisation of novel sensing schemes for rapid monitoring of nanoscale biochemical interactions. Many pathologies such as cardiovascular disease present physical biomarkers in patient samples. By probing at the surface of a thin-film, organic semiconductor, distributed feedback laser a novel biosensing scheme utilizing oligonucleotides has been studied and is reported in this thesis. Using an optical approach, Truxene and BBEHP-PPV DFB lasers are put to the test, assessing their sensing capabilities using laser wavelength shift as the transducing method. Bulk sensitivities of 23 nm.RIU^{-1} (Tr) and 21 nm.RIU^{-1} (BBEHP_PPV) are observed. The Tr-DFB lasers demonstrated higher sensitivity in bulk superstrate and surface material adsorption tests.

As an alternative to wavelength shift, silver nanoparticle labelled oligonucleotide targets were used to influence the threshold fluence required for OS-DFB lasers to achieve laser action. Using this method, a successful immobilisation strategy for oligonucleotide probes on the surface of an OS-DFB laser, for the first time to our knowledge, was confirmed. Target AgNPs were detected by SERS with a 20x objective on a Raman microscope (Gloucestershire, UK) equipped with an excitation wavelength of 514.5 nm and comparative concentration dependant effects on OS-DFB laser threshold fluence down to 11.5 pM. The capture of 40-45 nm AgNP surface bound target oligonucleotides via hydrogen base pair bonding to corresponding probes on the OS-DFB laser surface was shown to be selective down to individual nucleotide. Such detection limits are within diagnostic significance and the protocols have scope for modification to suit a multitude of different applications.

The novel demonstration of a molecular attachment strategy for oligonucleotide biosensor probes to an OS-DFB laser surface and the detection of AgNPs bound by complementary strand hybridisation using SERS and a comparative threshold fluence detection method are of particular note. The text within explores the characteristics of these sensing regimes and compares and contrasts the biosensing technologies involved.

TABLE OF CONTENTS

ABBREVIATIONS

AFM - Atomic Force Microscopy

AgNP - Silver Nanoparticle

AMI - Acute Myocardial Infarction

ApopA-I - Apoliprotein A-I

ApopB - Apoliprotein B

ASE - Amplified Spontaneous Emission

Azido-PEG$_4$-NHS - PEGylated azido N-Hydroxysuccinimide ester

BBEHP-PPV - Poly[2,5-bis(20,50-bis(200-ethylhexyloxy)phenyl)-p-phenylene vinylene]

BNP - B-type natriuretic peptide

CCD - Charge-coupled Device

CMOS – Complementary Metal-oxide-semiconductor.

CVD - Cardiovascular Disease

CQD - Colloidal Quantum Dot

CuAAC - Cu(I) catalysed 1,3-dipolar azide-alkyne cycloaddition

DBR - Distributed Bragg Reflector

DFB - Distributed Feedback

DL - Detection limit

DMSO - Dimethyl Sulphoxide

DNA - Deoxyribonucleic acid

ECG – Elecrocardiogram

FWHM - Full-width Half Maimum

IgG - Immunoglobulin G

InGaN - Indium Galium Nitride

LD - Laser Diode

LED - Light Emitting Diode

LOD - Limit of Detection

MEH-PPV - poly(2-methoxy-5-(2'-ethylhexloxy)-p-phenylene vinylene)

MGITC – Malachite Green Isothiocyanate

MPO - Myeloperoxidase

n_{eff} - Effective Refractive Index

NHS - N-Hydroxysuccinimide

NSA - Non-specific Absorption

OME-PEG$_4$-NHS - O-[(N-Succinimidyl)succinyl-aminoethyl]-O'-methylpolyethylene glycol

OS - Organic Semiconductor

PBS - Phosphate Buffer Saline

PDI - perylene diimide

PEG - Polyethylene Glycol

PFO - Poly(9,9-di-n-octylfluorenyl-2,7-diyl)

PhC - Photonic Crystal

PMMA - Poly(methyl-methacrylate)

POC - point of care

PPL - Poly(phenyl)-Lysine

PPV - Poly(phenylenevinylene)

PS - Polystyrene

PVA - Polyvinyl alcohol

RNA - Ribonucleic acid

SERS - Surface Enhanced Raman Spectroscopy

SNR - Signal to Noise Ratio

SPR – Surface Plasmon Resonance

SY - Super Yellow

TE - Transverse Electric

TM - Transverse Magnetic

TNF-α - Tumour Necrosis Factor alpha

Tr - Tris(terfluorenyl)truxene

WHO – World Health Organisation

LIST OF FIGURES

LIST OF TABLES

Chapter 1

INTRODUCTION: MEDICAL DIAGNOSTICS AT THE POINT OF CARE

1.1 INTRODUCTION

The subject of this thesis sits at the cusp of photonics, biochemistry and health technologies. Photonics is the technology of light, where photons are generated, controlled, made to interact with matter and detected in order to realise a function or a series of functions – akin to electronics but using light instead of electrons. Biochemistry is the science of chemical processes related to biology, and the technology of harnessing these processes. One area where photonics combined with biochemistry continues to enable great advances is the field of medicine, in particular given the context of this work, biosensors for diagnostics.

A biosensor is a device that can detect ('sense') a substance (the analyte) that may be present in a biological sample. For medical diagnostics, the medium is typically blood, urine, plasma or saliva, and the analytes are molecules whose presence correlates with a medical condition, i.e. they are biomarkers. Typically for detection, a bio-chemical reaction must first take place at the sensor/sample interface in order to capture analytes, and therefore the (possibly photonic) sensor must be primed for biomarker detection using biochemistry.

Biosensing for diagnostics is historically done in centralised laboratories. This has benefits in terms of scale as large expensive equipment can be used for multiple markers detection on multiple samples. A trained technician is needed to prepare the sample and tests and to operate the testing equipment. Much of the test equipment is based on light for transducing (see sections 1.7 and 1.8 for background on optical biosensors) and give very high sensitivity and detection limits. A downside of the centralised approach is that results of a test take at best a few hours to, more typically, a few days before being available. There are instances where being able to test for a biomarker or a series of biomarkers rapidly, at the point of care (POC), is critical. While POC diagnostics have been around a long time, current solutions do not yet offer the same performance as centralised laboratory tools, and therefore there is intensive research looking at filling that gap and translating performance to compact, portable devices for point-of-care use.

Specifically, the work described in this thesis is about exploring the feasibility of a compact device platform for medical diagnostics at the POC based on a planar micro-laser (a photonic device) whose surface is functionalised with deoxyribonucleic acid (DNA). The use of the platform is motivated by cardiovascular disease (CVD) biomarker detection and therefore discussed in that context, however it is important to note that its principle can be adapted for the detection of markers for other conditions. The key technical novelties reported are (i) the use of click chemistry, a specific and robust protocol for covalent attachment DNA on surfaces, directly on a laser platform, and (ii) the demonstration of a novel form of transduction for sensing with such a laser platform. (i) and (ii) are combined to demonstrate the principle.

The remainder of this chapter presents the motivations for this work, the concept of biomarkers for CVD, a brief introduction to biosensors, lists the current commercial technologies for POC sensing devices, and discusses some of the biomolecular approaches to sensor functionalization, highlighting the attractiveness of click chemistry. The concept of click chemistry is introduced only briefly but more details on its origin and applications to materials science, in particular for surface functionalization, are found in Chapters 2 and 4. The following also describes (active and passive) evanescent wave resonator sensors, and explains the rationale for the choice of the organic distributed feedback (DFB) microlaser as the detection platform, giving the basic concepts behind it and the state of the art of this particular field of biosensing device.

1.2 MOTIVATION AND CLINICAL NEED

With the rise of stratified medicine and personalised care, tailored to specific patient groups, there is a necessity to take clinical diagnosis out of the laboratory and to the point of care, tailoring treatment specific to the patient's needs [1]. To that end the field of biosensors is developing towards portable, high resolution solutions which can achieve detection at the nanoscale. These devices complement laboratory testing diagnostic routes well for many pathologies including CVD, as untreated cardiac events have a high risk factor and treating quickly can drastically improve the patient's chances [2]. They can also contribute to relieving the cost pressure placed on health systems by inefficient treatments. For example, in an emergency response setting, any patient showing signs of CVD symptoms are immediately treated, even though a proportion of such patients are false positive with symptoms due to less severe reasons. A rapid biomarker analysis would be very useful to confirm the diagnostics and only treat patients that truly need it.

1.2.1 CARDIOVASCULAR DISEASE

CVD is not one condition but a range of different conditions affecting the circulatory system. After the onset of a cardiac event, such as a heart attack or a stroke, of this nature tissue damage causes the release of indicative biomarkers to be released into the patient's blood stream [3]. Biochemical analysis of patients' samples (e.g. blood) in centralised laboratories is commonplace with biomarker detection, but as stated before there is a relatively long turn around. Conversely, POC diagnostic tools allow for rapid, local analysis of a patient without the need for dedicated laboratory space or equipment [4]. Their aim is to allow for a quick and reliable diagnosis for a patient so that the most appropriate treatment can be issued in a timely, and cost effective, manner.

It was stated by the World Health Organisation (WHO) to be responsible for almost 31% of global deaths 85% of which were a result of heart attack or stroke [5, 6]. CVD refers to a range of conditions which affect the heart and circulatory system [6, 7]. These tend to fall into one of the following categories (although this is not exhaustive):

- Atherosclerosis
    - Typified by the accumulation of plaque/debris on the arterial walls, narrowing the blood vessels. Immune cells then swarm the damaged tissue and activated endothelial/immune cells trap a plaque in the vessel wall [8].
- Arrhythmia
    - An irregular or disrupted heartbeat. A cascade of signals emanating from the sinoatrial node control the filling and contracting of the ventricles to pump blood around the body, disruption or irregularities in these signals firing can cause asynchronous pumping and is the predominant cause of arrhythmia [6].
- Heart and Valvular Defects
    - These can be congenital malformations of the valves or even the membranes between the aorta and ventricles putting increased demand on the heart or reducing its function.
- Infections
    - Endocarditis (infection of the inner lining of the heart) and other infections can also cause defects in the Heart and Valve operation leading to CVD

Whether its narrowing blood vessels or malfunctioning hearts these conditions can lead to some fatal CVD events such as heart attacks, strokes, blood clots, embolisms or heart failure. Hardening vessel walls can lead to an increased susceptibility to shear stress leading to tearing [6].

A high throughput, specific biosensor capable of analysing multiple markers simultaneously would be a great asset to the successful diagnosis/treatment of these conditions; as delayed treatment is linked with a dramatic increase in mortality. For CVD diagnosis patients, from the following criteria: elevation of blood biomarker levels; characteristic chest pain; diagnostic electrocardiogram (ECG) alterations, should present with at least 2 symptoms. To make CVD diagnostics more difficult half of the CVD patients admitted to emergency departments show a normal ECG pattern [9]. Thus, it is evident that CVD patients would benefit from more sensitive, reliable, cost-effective diagnostic platforms which can deliver POC diagnostics with real-time detection and monitoring.

1.3 BIOMARKERS

As mentioned, one useful diagnostic tool to help identify and monitor disease pathologies, or to assess patient risk, is the measurement of biological markers (biomarkers). Biomarkers are biologic variables which can be used to indicate certain pathological events or susceptibility to a range of conditions [10-14]. They encompass many forms of measurable factors including concentrations of biological components such as proteins/enzymes [15] or the presence of certain gene alleles.

In 1998 the National institutes of Health Biomarkers Definitions Working Group defined biomarkers as “a characteristic that is objectively measured and evaluated as an indicator of normal biological processes, pathogenic processes, or pharmacologic responses to a therapeutic intervention.” [16]. Other organisations have suggested their own definitions but there is much overlap and generally their definitions extend it to any indicator reflecting the response of a biological system. As the field of medicine has advanced, research has yielded more and more so that now a wide range of different conditions can be monitored and diagnosed by the sensing of biomarkers. These take the form of a range of biological materials such as circulating short length ribonucleic acid (micro-RNA) [17-20], DNA [21-23] and proteins [24-27], which are found in the blood, plasma or other fluids.

With respect to CVD there are a number of biomarkers that can be analysed to assess risk factors [35]; Troponin (helps differentiate between acute myocardial infarction and unstable angina) , D-dimer (indicating a pulmonary embolism), B-type natriuretic peptide (BNP) (shown to have implications in ischemia) [36], ApoB (linked to the formation of atherosclerosis) [37] and CRP (an inflammation marker which has been used as a predictor for coronary heart disease) [37] to name a few. Table 1.1 gives a more comprehensive list of CVD biomarkers and their diagnostic relevance. As is shown in the table some biomarkers require detection levels on the sub-nanoMolar scale.

Troponin, which correlates with Acute Myocardial Infarction (AMI), is used in the UK for triaging patients and safe discharge or treatment in an emergency setting. There exist POC devices for the detection of troponin but they have some drawbacks (see section 1.5.1) and there is a push to reduce the limit of detection (LOD) for the detection of troponin at extremely low levels. There is therefore an incentive to improve existing sensors and to explore alternative platforms

1.4 CONCEPT OF BIOSENSORS

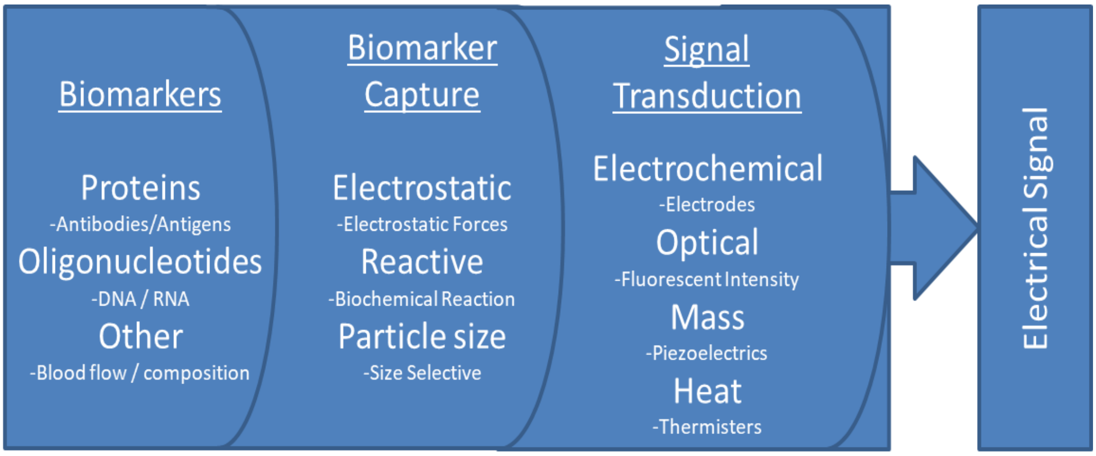

Figure 1.1 - General overview of different biosensing components with examples.

As mentioned in Section 1.1, the role of a biosensor is to detect particular biomarkers, to assess their presence in a sample and their concentration or amount. The latter can be used to build a biochemical picture to help patient diagnosis. The concept of a biosensor (see Figure 1.1) usually relies on immobilising biomarkers, if present, onto or within a sensing device. This biochemical process is then transduced (in a number of different ways) into a physical, readable parameter.

Optical based transduction is heavily utilised in centralised laboratories equipment and in some point-of-care devices. One challenge is to translate the remaining capabilities of such lab based testing strategies into miniaturised sensing tools with short turnaround times delivering results at the point-of-care. Current biosensing technologies include detection using colorimetric,

fluorescence, surface plasma resonance (SPR) and fibre optics/bio-optrode (optically); complementary metal-oxide semiconductor (CMOS) and Si chips (acoustically); potentiometric, amperometric and impedimetric transducers (electrochemically); or magnetic-based biosensors [3, 6].

1.5 CURRENT TECHNOLOGIES

While standard biomarker detection is carried out in centralized laboratories, approaches to medicine for early disease prevention [2], triaging and chronic disease management [38] necessitate the development of point-of-care diagnostic technologies to provide rapid results in non-laboratory settings [39, 40]. Several technologies have been developed for virus detection utilizing optical, electrical, and acoustic sensing methods such as SPR, Photonic Crystal Resonators (PhC), nanowires, and impedance analysis [41-45]. Full Electronic or amperometric methods are well suited for miniaturisation and integration on chips but usually require labelling strategies to achieve detection. Optical methods are gold standards in centralised labs but miniaturisation is more difficult, although now with progress in the field some platforms are now showing promises to realise it.

Biomarker	**Use**	**Cut Off Levels**
Troponin I (cTnI) [28]	Detection of AMI	0.4pM-4pM
Troponin T (cTnT) [28]	Detection of AMI	1.2pM-2.5pM
C-Reactive Protein (CRP) [29]	Early Detection of inflammation and cardiac risk factors	< 9.5nM, Low Risk; > 28.6nM, High Risk
Cretine k muscle/brain (CK-MB) [30]	Early Detection of AMI	119pM
B-Type natriuretic peptide (BNP) also NT-ProBNP) [31]	Detection of acute coronary heart diseases, congestive heart failure, ventricular overload	BNP: 28.9pM/NT-proBNP: 142.9pM
Myeloperoxidase (MPO) [32]	Detection of inflammation	2.3nM
Apoliprotein B and Apoliprotein A-I (ApopB and ApopA-I) [33]	Prognostic, risk of prediction for myocardial infarction	ApopB/ApopA-I >1
Myoglobin [34]	Detection of acute myocardial infarction	12.0nM

Table 1.1 – CVD Biomarker uses and diagnostically relevant concentrations, adapted from Table 1 Honikel, Lin [6]

Some studies have reported success with optical technologies developing biosensors which could prove useful to this need in point-of-care diagnostics[46-49], combining evanescent sensing platforms with antibody protein or nucleic acid (DNA sensing) bio-recognition approaches. The current technologies are subject to limitations, discussed herein in more detail, some of which the protocol presented in this text hopes to address.

1.5.1 POINT OF CARE DEVICES

POC [50, 51]tests have been widely used in medicine for a long time now but there is a long way to go in translating full laboratory capabilities to the site of patient care. The introduction of the blood glucose monitor dating back to the 1960's saw a handheld, battery powered device to allow for quick and easy testing of glucose levels in blood samples [52]. Previous POC testing for glucose monitoring had been in the form of a tablet reagent to estimate the glucose levels in urine. Since then a variety of POC diagnostic tests and devices have been created and in some instances have become more prevalent than the lab based tests they have replaced. Biosensor technologies have been a key part in the development of POC devices, their implementation involving the use of physiochemical biomarker detectors [53]. There are a variety of different types of sensors and ways of implementing them, which convert the biological variables into detectable signal variations. Commercial POC devices that can target one or a few biomarkers related to CVD are based on a few different, long established detection technologies: fluorescent labelling of analytes, electrochemical interactions or chemiluminescent detection (see Table 1.2).

However, translating the full capabilities of centralised laboratories to POC has proved elusive so far. Current POC devices do not combine all of the desirable characteristics (multi-markers detection, sensitivity, fast response and low cost) [54]. To improve on this and accelerate adoption, alternative sensing technologies, like those developed in this work, are needed. Additionally, a reduction in the cost of biomarker assays for POC devices (such as immunoassays discussed in section 1.6) is important. Currently, all POC devices for CVD make use of an antibody based immunoassay approach, which presents challenges in achieving such a reduction.

POC device	Biomarkers	Assay time	Detection Method	Multiplexing Capability
i-STAT (Abbot Point of Care)	Troponin CK-MB BNP	≈10 min	Amperometric	No
Triage MeterPro (Alere)	Troponin Myoglobin CK-MB	≈15 min	Fluorescence Intensity	Yes
Cobas h232 (Roche Diagnostics Ltd.)	Troponin Myoglobin CK-MB D-Dimer NT-ProBNP	8-12 min	Fluorescence Intensity	No
Decision Point (Nexus Dx)	Troponin Myoglobin CK-MB	≈15 min	Chemiluminometric	No*
RAMP Reader (Response Biomedical Corp.)	Troponin Myoglobin CK-MB NT-ProBNP	≈15 min	Fluorescence Intensity	No
Stratus CS Acute Care Diagnostics System (Siemens)	Troponin Myoglobin CK-MB NT-ProBNP	14 min	Fluorescence Intensity	No
AQT90 FLEX (Radiometer)	Troponin CK-MB Myoglobin NT-ProBNP Procalcitonin CRP D-Dimer βhCG	11-21 min	Fluorescence Intensity	Yes

Table 1.2 - Commercially available POC devices for CVD diagnostics

Like for optical biosensors in general, there are 2 core components in any POC device: a transducer to convert the biological signal into a measurable variable and a method for achieving specificity for the target biomarker. Examples of these are shown in the following section.

1.6 BIOSENSING SURFACE CHEMISTRY

Devices currently available in the field work by way of immunoassays to bind antibodies and antigens [4]. These pairings have high specificity and the antigens are usually the analyte molecule captured from the patient sample. Generally a sandwich immunoassay is performed; a surface coated with the antibody is exposed to the patient sample capturing any antigens, the surface is then washed over with a second antibody "sandwiching" the antigen between them [55]. Labels can be attached to one or both of the antibodies to allow optical or electrochemical detection of the binding; this principle is depicted in Figure 1.2(a).

Antibodies are proteins and cell cultures are needed to produce them in industrial quantities; this process is labour intensive and costly due to the high level of environmental controls required to achieve reproducible cultures. Proteins are very susceptible to denaturing as a result of temperature fluctuation and genetic variations can cause structural differences between different batches [56].

An alternative to the immunoassay protocols is to consider single stranded oligonucleotides as the analyte and capture them by the process of hybridisation; binding with their complementary strand as shown in Figure 1.2(b) (based on the hydrogen bonding between nucleotide base pairs) [57]. Oligonucleotides are strands of DNA or RNA like molecules with many bases.

These oligonucleotide biomarker-probe pairings have much more scalable, specific and simpler, less costly fabrication techniques. The recent introduction of Aptamer probes, folded oligonucleotides that bind protein analytes, can also be used. Since oligonucleotide probes are more stable than protein antibodies, POC devices based on oligonucleotide protocols would be more suitable for warmer climates and places which lack access to cold storage facilities [4].

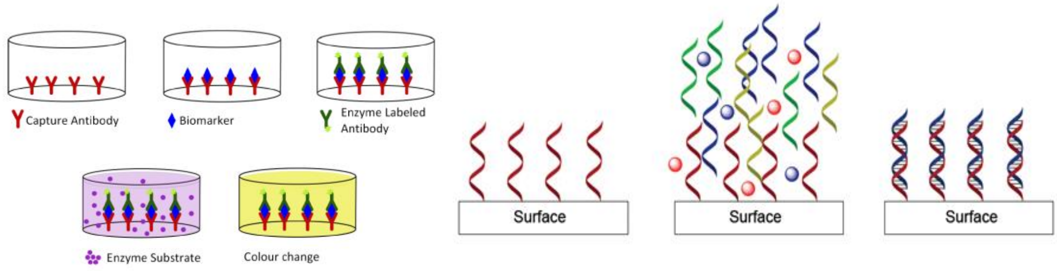

(a) (b)

Figure 1.2 - (a) Sandwich immunoassay binding antigens into antibody-antigen-antibody sandwiches labelled for detection. (b) Nucleotide sequences binding hybridising to immobilised complementary strands.

1.6.1 BIODETECTION PROTOCOLS

Another aspect of biosensor design is the choice of detection strategies. These can be optical, as with fluorescence [58] and chemiluminescence based strategies [59], or electrochemical [60, 61] as with the amperometric / potentiometric / chronoamperometric / impedimetric sensors [6]. Many cardiac biomarker POC devices operate by measuring either the absorption or the fluorescence of labelled sandwich assays. The detection involves some processing to label the antigens before the detection of the binding event is performed (Figure 1.3(a)&(b)). A label-free system should allow for a faster diagnosis and simpler, less costly devices.

In emission based optical systems fluorophores are used as labels on the antibody proteins. These are excited by a light source and their emission is used as the measurand. By comparing the emission before and after the binding of the second fluorophore labelled antibody, the success of binding events can be determined. In contrast to this, in an absorption based detection strategy, the absorbance of fluorophore labelled antibodies captured in the sandwich immunoassay is used as the measurand to detect successful antibody-antigen-antibody binding events [4].

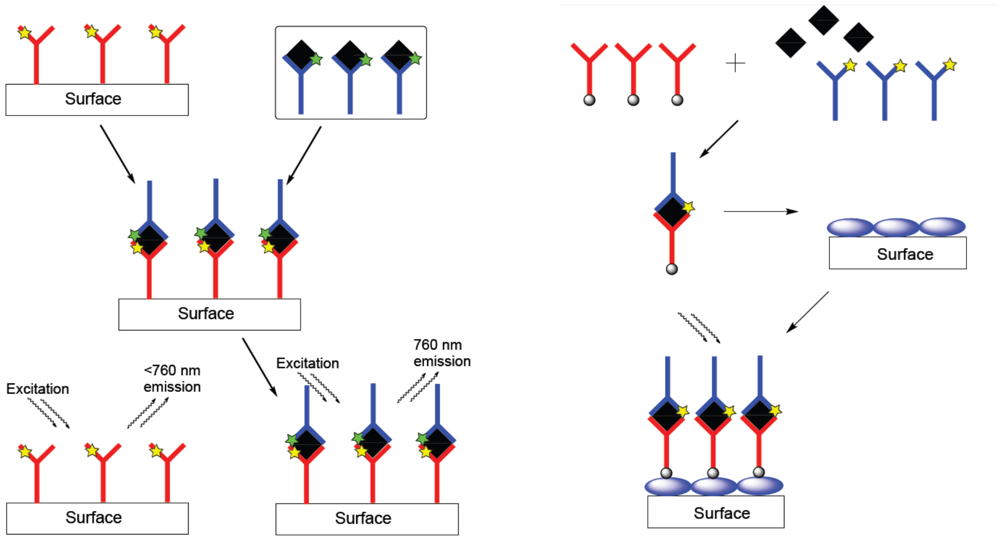

(a) (b)

Figure 1.3 – Fluorophore (stars) labelled antibody-antigen (black rhombus)-antibody sandwich immunoassay detection strategies (a) emission based optical detection of sandwich immunoassay (b) absorption based optical detection of sandwich immunoassay

Chemiluminescence refers to luminescent emissions as a result of chemical reactions, it can be employed as a detection strategy where a chemical reaction causes a colour shift [62] and is used in many POC devices and immunoassays. For chemiluminescent cardiac biomarker detection there is the Decision Point ® POC, which works similar to the protocol in Figure 1.3(a) but the binding of the antibody-antigen complex causes a region of a test strip to change colour above diagnostically relevant concentrations. Systems such as this benefit from simplicity but lack the accuracy of other devices, with a somewhat binary output; they also present no improvement in turnaround time in comparison to other POC devices shown in Table 1.1.

Electrochemical detection [63] relies on labelled antibodies similar to optical systems; the labels take the form of enzymes which catalyse a redox reaction and generating current which can be read by amperometric methods. Electrochemical sensors are suited to miniaturisation due to the microfabrication techniques employed in the transduction elements. As the enzyme is bound to the surface and a substrate fluid is added to the chip and incubated the resulting redox reaction can be detected as a change in current flow through the electrode.

1.6.2 OLIGONUCLEOTIDE BIOSENSORS

In contrast to the sandwich assay based approaches discussed so far, oligonucleotide approaches to biosensing could employ less complex procedures as the target biomarkers will bind to surface probes and don't require the extra processing like that of the sandwiching antibody protein binding to the target antigen as seen in Fig 1.3.

Oligonucleotide based biomarker probes are far more cost-effective than corresponding antibody-based platforms and can increase the possible applications of a POC device employing such strategies; they allow the diagnostics to be performed in wider variety of places away from climate controlled environments like centralised laboratories. Most of the existing oligonucleotide based approaches to biosensing rely on the fluorescence [64-66] based approaches discussed in the previous section. These lack the resolution which photonic resonator based approaches have the potential to deliver by monitoring molecular interactions at the interface of the device and the sensing medium.

1.6.2.1 Nanoparticles

Metal nanoparticles have been used to enhance the signal to noise ratio (SNR) of Raman spectroscopy in Surface Enhanced Raman Spectroscopy (SERS) [67], this results from photonic interaction with surface plasmons of the nanoparticles and is discussed further in Chapter 4. Nanoparticles are nanoscale masses of atoms. Most current technologies used in POC biosensors involve some form of labelling strategy. While the ideal protocol would circumvent the need for a labelling strategy unlabelled detection is less likely to provide detection at extremely low, nanomolar or even sub-nanomolar, concentrations. By enhancing the protocols detection with nanoparticles it might be possible to lower the LOD to diagnostically relevant limits.

1.6.3 SURFACE BOUND PROBES

Here the basic principles of some specific biochemical interactions that can be used for biomarker capture have been introduced. To function well a biosensing paradigm must ensure that these interactions occur at the sensor so they can be detected. Amine ligation strategies present a wealth of ligation partners while the robust and specific, click chemistry, approach has many advantages for surface functionalization. The term click chemistry in general refers to chemical reactions which are orthogonal, in the sense that there are no chemical groups that can interfere with the reactions and create side products, and can proceed under mild and simple conditions with high yields [68]. Click chemistry has appeared less than 20 years ago but, as a consequence of its simplicity and versatility, it has already pervaded organic synthesis and material science, in particular for modifying/functionalising nanomaterials and surfaces for a range of applications including lithography, assembly and sensing. For example, used for immobilisation on electrochemical sensors [69], click chemistry provides an ideal strategy for immobilising oligonucleotide probes on a sensor surface. In this work, it was utilised (for the first time to the author’s knowledge) for oligonucleotide probe immobilization on a laser. In consequence, click chemistry is discussed further in Chapter 2. It is also discussed in later chapters as it has been used extensively with oligonucleotides. Used for immobilisation on electrochemical sensors click chemistry provides an ideal strategy for immobilising oligonucleotide probes on a sensor surface.

1.7 PHOTONIC (OPTICAL) RESONATOR BIOSENSORS

Optical biosensors are already an established technology with several different approaches to signal transduction utilised in laboratory settings. For ease of discussion, these can be classified in two broad families: (i) Fluorescence and absorption sensors and (ii) evanescent wave sensors. This is slightly arbitrary as some evanescent wave sensors fall within both categories. Thereby, consider here an evanescent wave sensor where there is a resonator acting as a frequency selective element for the transduction process. Furthermore, evanescent wave/resonator sensors can be divided as passive and active resonators. Passive resonators such as PhC and SPR approaches, in contrast with active resonator structures like DFB lasers, have all been demonstrated for biosensor development. As with other biosensors these different approaches come with a myriad of different advantages and disadvantages; making them each suitable for different applications as discussed in the following text. Fluorescence detection has been briefly covered in previous sections [6, 70, 71]. The following introduces so called resonator sensors with examples.

1.7.1 EVANESCENT WAVE SENSING

During waveguiding of electromagnetic (E-M) waves at a material interface an evanescent field (a spatially localised field of E-M energy) is generated surrounding the event. This is the case in optical fibre waveguides and in structures like DFB lasers. This field extends into the regions surrounding the material interface and causes the refractive index of those regions of space to exert an effect on the incident E-M wave as it propagates away from the interface. By monitoring the optical properties affected by such events (wavelength, phase shifts, etc.) it is possible to model the waves behaviour in such a way that you can relate the shift in these properties to the effective refractive index observed by the waveguide or laser mode in these regions.

Employed as sensors, devices whose operation rely on such interactions can be designed so that molecular interactions occur in regions where the evanescent field strength is such that they produce a measurable shift in the output. The resolution of such devices is defined by the smallest shift that the output will respond to in a measurable way while the sensitivity represents the shift produced relative to the physical property being transduced. The detection limit ($DL = R/S$) of such a device is defined as the resolution divided by the sensitivity. Optical sensors are typically characterised by their sensitivity, measured in wavelength shift with respect to change in refractive index (typically nm.RIU^{-1}). Discussing further, bulk sensitivity, whereby the change of refractive index in the sensing medium is measured, and surface sensitivity which is the sensitivity of the sensors to detect molecular interactions localised to the interface between the sensor and the sensing medium, are considered.

1.7.2 PASSIVE RESONATOR SENSOR

Passive resonator biosensors operate whereby the resonator output is passed through a medium in which biomolecular interactions cause a shift in optical properties causing measurable changes in the output. The basic principles of SPR and PhC are outlined in the following text but these are just 2 examples, others such as resonant waveguide gratings [72, 73], have also demonstrated potential biosensing capabilities.

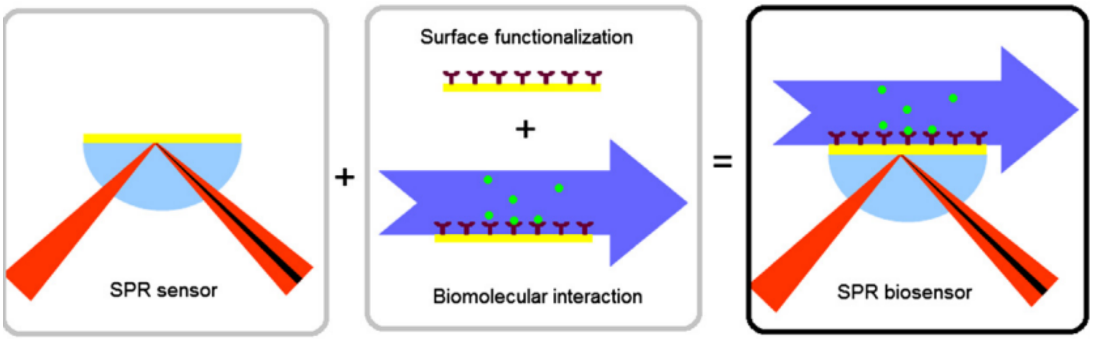

Figure 1.4 - SPR biosensor schematic reproduced from Figure 7 of Wijaya, Lenaerts [74] 2011 paper

1.7.2.1 SPR

Surface Plasmon Resonance (SPR), where light incident at the resonance angle is confined at a dielectric interface of opposing permittivity, has been used in biosensing since 1982 [75]. The technology operates by measuring the resonance angle observed from plasmonic vibrations at a metal surface where this angle is dependent on optical properties at the interface. Compared to fluorescent or other labelling paradigms; it can measure the kinetics and affinity of biomolecular binding in real-time without the need to label the target biomarker while these take place in nanoscale detection space superstrate to the boundary of reflection [76].

The technology has been the foundation for many studies [74, 77] and has even spawned some commercial products and current work is geared towards tuning the sensitivity and device structure for specific applications. Figure 1.4 shows the basic principles of the technology; light is focused to a point of investigation and the reflected light is captured at a detector. The total reflection of the incident light is affected by biomolecular interactions on the surface of the sensor altering the refractive index such that it is detectable in the output.

1.7.2.2 Photonic Crystal Resonators

Photonic Crystal (PhC) biosensors like those used by Gallegos et al. [78] in a smartphone biosensor system utilise PCs which operate blocking, by reflection, a narrow band of wavelengths. Biochemical interactions at the surface of these devices will shift the reflected band due to changes in the dielectric permittivity at the interface between transducer substrate and liquid media [42, 79-82]. First demonstrated in a 2002 paper by Cunningham, et al. [83] to be a viable biosensing strategy, the low-loss dielectric materials of a PC optical resonator enable sub-nanometre bandwidths with 95%+ reflectivity resonances. PhC based biosensors benefit from being highly tuneable across the UV, visible and infrared portions of the spectrum [83-86] and have been demonstrated on a wide variety of materials, so they can be easily modified to be specific for application [87].

1.7.3 ACTIVE RESONATOR SENSORS

In comparison to passive resonators, active resonator sensing involves the molecular interactions being coupled into the evanescent field produced by the confinement of the laser mode while maintaining high resolution due to the coherence of the laser light. In this way active resonators enable higher resolution * sensitivity product and allow for a simpler design as there is no need for precise alignments to inject light into the sensing dielectric. The DFB (Distributed Feedback) laser is such a resonator sensor. The following section will outline the basic principles of DFB laser biosensors and go on to present an overview of the state of the art.

1.8 DFB LASER BIOSENSORS

DFB lasers employed as evanescent sensors [15, 88] have been shown to be responsive to changes in refractive index due to material absorption down to the nanoscale [89] and encapsulation experiments [90] have shown that the threshold of the DFB lasers are also responsive to changes in material adsorbed onto the device surface. Devices with a narrow linewidth, they operate as active resonators that can be adapted to biosensor applications.

Work by Anne-Marie Haughey [4, 91-95], explored in detail the biosensing potential of DFB lasers and laid the foundations for a biofunctionalization strategy to utilise the lasers as oligonucleotide biosensors. Other groups [15, 96, 97] have demonstrated the biosensing capabilities of the technology probing for antibody/antigen biomarker pairs. As discussed in the following chapter DFB lasers can operate as evanescent sensors. Material adsorption and biochemical interactions at the interface between the surface of the device and the sensing medium will alter the refractive index as seen by the laser mode. The basic concept and elements of a DFB laser sensor are discussed next but more details on the design and theory can be found further in Chapters 2 and 3.

1.8.1 CONCEPT

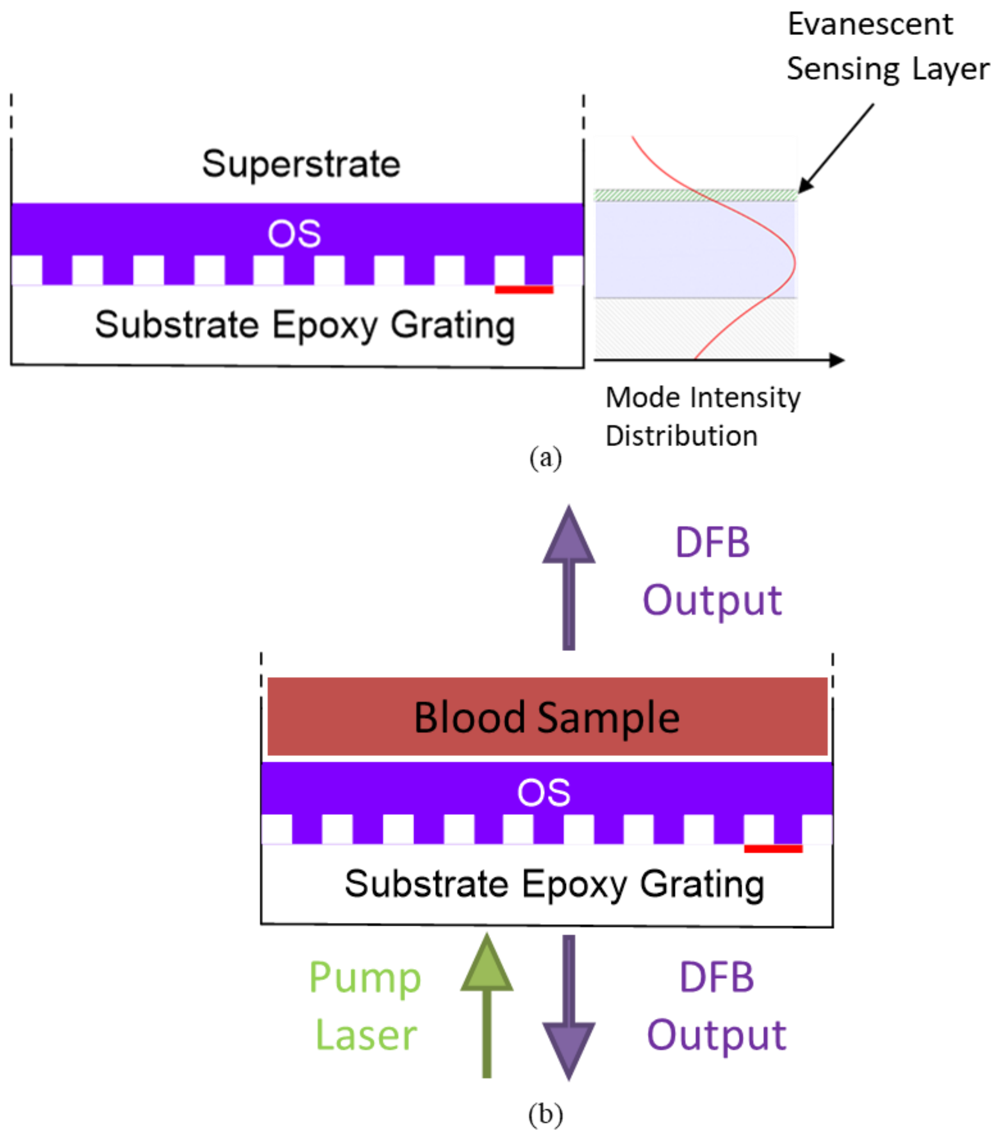

Figure 1.5 - Schematic of evanescent sensing paradigm based on DFB laser biosensor (a) schematic of laser showing evanescent field distribution vertically through laser cavity. (b) schematic of 2nd order DFB laser employed as biosensor

Distributed feedback lasers are typically formed of an active gain material waveguide with an imprinted grating structure which creates a cavity producing optical feedback at a narrowband of wavelengths. When the optical gain material is optically pumped with sufficient energy, the structure effectively generates laser action. 2nd order DFB lasers are designed such that a laser beam is emitted perpendicular to the plane of the waveguiding structure. Seen in Figure 1.5 are basic schematics of a DFB laser biosensor, the substrate region is comprised of a low refractive index optical epoxy imprinted with a grating structure coated with a thin film of optically active gain material. In Figure 1.5(a) the red graph on the right represents the transverse intensity distribution of the laser mode throughout the structure.

By design, the device will respond to changes in the refractive index in the sensing layer (the thin green band at the bottom of the region superstrate to the DFB laser structure). In this way, molecular interactions as a result of exposing the DFB laser surface to a blood sample, as shown in Figure 1.5(b),will shift the DFB output. The gain layer is fabricated to only hundreds of nanometres in depth (or less) so the evanescent tail of the mode confined in the cavity will interact with this region (this process is explained further in Chapter 2). The DFB output can be collected by a fibre and analysed by a spectrometer to observe the wavelength shift.

1.8.2 GAIN MATERIALS

Two main candidates are primarily used as gain materials in DFB laser fabrication, Dyes [88, 98] and thin-film Organic Semiconductor(OS) materials [88]. In their early implementation DFB laser biosensors were fabricated with Dye based materials. While boasting broad spectra and tuning capabilities across the visible spectrum, Dyes cannot compete with thin film OS materials in terms of the quantum yield of neat films; emissions are quenched in the solid state by non-radiative relaxation of the excited electrons. To overcome this quenching Dyes are suspended in a transparent matrix at low concentrations. Rhodamine 590 [99], Coumarin 503 [88] and Pyrromethane [100] have been previously used for DFB laser biosensor fabrication. Section 1.8.3 will discuss further the use of Dyes in these early DFB laser biosensors where it is demonstrated that OS based devices are more suitable to the application since the matrix suspension of dyes affects key design considerations for DFB laser sensors; namely laser threshold and the gain material’s refractive index.

OS gain materials are comprised of conjugated molecules with overlapping orbitals which result in their semiconductor properties. Polymers, conjugated dendrimers and Spiro-compounds are a few of different semiconductors which can be used as lasing materials for DFB laser fabrication [98]. PPV Poly(phenylenevinylene) [101, 102] derivatives are conjugated polymers with alternating single and double bonds which allow delocalized electrons to flow, BBEHP-PPV (poly[2,5-bis(2',5'-bis(2"-ethylhexyloxy)-phenyl)-p-phenylenevinylene]) [89, 90] and MEH-PPV (poly(2-methoxy-5-(2'-ethylhexloxy)-p-phenylene vinylene)) [97] have been the most widely researched PPV derivatives in such applications. A commercially available SY (Super Yellow) PPV derivative was also assessed as an evanescent sensor due to attractive optical and photonic properties [103], the design of these molecules can be tailored for application. Side chains for example can be used to optimise luminescence efficiency and chromophore density [98], overcoming the localised quenching which dye based neat films suffer from.

The tris(teruorenyl)truxene (Tr) [92] oligomer is another OS which has been demonstrated as a gain material for DFB lasers [89]. Rather than a long chain polymer of repeating units a film of conjugated oligomers is comprised of a number of discrete macromolecules units with arms of repeating units surrounding a chromophore [98]. An exploration of the optical properties of the OSs used in this work can be found in Section 2.2.3. The next section will cover the progress to date in DFB laser biosensing.

1.8.3 STATE OF THE ART

The first organic DFB laser biosensor to be demonstrated towards label free biosensing was in 2008; comprised of a one-Dimensional, second order DFB laser using Coumarin 503 doped Poly(methyl-methacrylate) (PMMA) for the gain material [88]. The laser had a threshold pump fluence of 180 J.cm^{-2} (10ns pump duration) and a bulk sensitivity to refractive index of 16.6 nm.RIU^{-1} where RIU is the refractive index unit with a 500nm emission wavelength in air. Since this initial implementation, investigations have demonstrated improvements in this sensitivity value. The introduction of a 30nm TiO_2 (Titanium Oxide) cladding layer to a DFB laser with a Pyrromethane doped Ormocomp gain layer [100] managed to achieve a bulk sensitivity of 99.58 nm.RIU but a lasing threshold fluence of 870 µJ.cm^{-2} (compared to 170 µJ.cm^{-2} for unencapsulated Rhodamine 590 doped SU-8 DFBs [104]) at 590 nm emission wavelength.

The higher sensitivity of the neat Rhodamine 590 doped SU-8 DFB laser when compared to the Coumarin 503 doped PMMA can be attributed to the higher refractive index of the gain material; 1.58 vs 1.48 respectively. The higher refractive index results in a greater confinement of the laser mode within the gain layer. With the introduction of the high refractive index TiO_2 layer photons leak into the cladding layer, this is why the threshold increases. This is also a source of greater sensitivity however as the confinement of the laser mode in the cladding region causing the evanescent field to overlap more with the superstrate sensing region. While a high sensitivity is ideal for low concentration sensing applications as is required for diagnostically relevant POC devices, a low lasing threshold fluence is also beneficial for minimising the pump source required and ultimately the efficiency and potential portability of the device itself. To minimise the lasing threshold with a TiO_2 encapsulated Pyrromethane 597 doped Ormocomp DFB laser a layer thickness of 20 nm was identified [105], in this configuration a bulk sensitivity of 95 nm.RIU^{-1} was demonstrated with a film thickness of 20-35 nm [100]. At thicknesses above 20 nm the high index TiO_2 layer would raise the mode confinement within the cavity so as to reduce overlap with the gain region; in turn raising the lasing threshold.

A TiO_2 nanorod cladding layer of thickness of 22 nm was demonstrated as optimal as this provided close to twice the sensitivity of a solid TiO_2 cladding layer of 30 nm when monitoring Poly(phenyl)-Lysine (PPL) surface adsorption [106]. Since the porous structure of the layer increased the surface area for adsorption the drop in refractive index between solid and nanorod structures (2.10 to 1.82 respectively) for the TiO_2 layer had negligible effect [106]. For biosensing applications, the surface sensing due to material absorption is a more accurate indicator of performance since this will resemble the shift observed due to biomolecular interactions with patient samples than bulk refractive index of superstrate material. TiO_2 nanorod cladding layer thicknesses showed a maximum sensitivity increase of 6.6x compared to an unencapsulated Rhodamine 590 doped SU-8 DFB at 90 nm but as previously discussed this resulted in a trade-off with lasing threshold energy increasing with thicker cladding layers. While these show a marked improvement in performance compared to the original demonstration of the technology one key benefit of DFB lasers is the ease of fabrication and this encapsulated fabrication technique does add extra complexity; the fabrication could no longer be handled by solution processing. TiO_2 coated Pyrromethane 597 doped Ormocomp DFB lasers have also been used to demonstrate single molecule diffusion imaging of sucrose molecules by focusing the output onto a charge-coupled device (CCD) camera and scanning a small area of the laser surface with the pump beam [107].

As was discussed in section 1.8.2 OS materials, including BBEHP-PPV and Tr gain materials are much less prone to quenching effects than their dye based counterparts and can be fabricated into DFB laser biosensors as neat films rather than incorporated into transparent matrixes [89].This allows the gain material to have higher refractive indices leading to greater confinement of the laser mode within the gain material and a greater overlap with the sensing region without the need for encapsulation [92]. Pumping OS DFB lasers with laser diodes has been demonstrated [90, 108] suggesting miniaturisation of the technology to be possible with off the shelf components which is preferable in the development of POC devices. In this implementation a transparent polymer is UV cured into a 2nd order DFB grating and the solution processable OS (with refractive indices 1.7-1.8) spincoated onto the surface producing a thin film 80-350 nm thick, determined by atomic force microscopy (AFM) which is discussed further in section 2.2.3. These achieved bulk refractive index sensitivities around

20 nm.RIU^{-1}. The properties of these materials and their biosensing capabilities are discussed further in the later Chapters of this text.

F8BT/MEH-PPV DFB lasers have also been demonstrated by depositing a thin film (130 nm) with an emission wavelength of 630 nm and a threshold of 92 nJ and a bulk refractive index sensitivity of 154 nm.RIU^{-1} [97]. This represents a huge leap in the sensitivity from that of a non-encapsulated dye based DFB laser. With a gain layer thickness of 130nm and a refractive index >1.8 (compared to 1.5-1.6 for Dye doped materials) these materials are well suited for improved surface sensing capabilities by way of raising the confinement of the laser mode to overlap more with the sensing region. Taking advantage of the “Vernier effect” organic distributed Bragg reflector (DBR) lasers [109], distinct from the common DFB implementations in that laser action relies on a standing wave forming between two reflector gratings, have been very recently incorporated into microfluidic channels [110]. Using a Poly(9,9-di-n-octylfluorenyl-2,7-diyl) (PFO)/MEH-PPV mixture as a gain layer (with thickness 120-135 nm), employing the Foster energy host/guest transfer system, a DBR laser has been demonstrated with a bulk refractive index sensitivity of 80-120 nm.RIU^{-1} [110]. Microfluidic channels are ideal for POC development as they can be incorporated into Lab-on-chip toolkits which make for simple sample processing and analysis tools.

Surface sensing demonstrations with DFB lasers show their potential for biosensing applications. Human Immunoglobulin G (IgG) was detected on a Rhodamine laser encapsulated by a 30 nm TiO_2 cladding layer, functionalised with a layer of Protein A, with a binding site for IgG, down to 3.2 nM [99]. With a cladding layer of 10 nm the group also demonstrated the detection of Tumour Necrosis Factor alpha (TNF-α),using surface bound TNF-α antibody, down to 3.5 pM which is within diagnostically relevant biomarker levels as presented in Table 1.1, assuming these levels to be typical of other antigen detection limits.

The biotin-avidin model has been used in multiple studies to demonstrate specific sensing at organic DFB laser surfaces. With a biotinylated surface F8BT/MEH-PPV DFB lasers demonstrated detection down to 373.1pM in an initial study[97], while similar experiments with a Tr-DFB laser yielded a LOD of 14.9 pM. Modelling work to investigate the potential sensitivity increase of a TiO_2 cladding layer on this protocol suggested a LOD as low as 4.4 pM could be achieved [89]. These results, as with the Dye based implementations suggest OS have the potential to detect diagnostically relevant levels of biomarkers. A perylene diimide (PDI) doped Polystyrene (PS) DFB laser was also used for label free detection of human ErbB2 protein down to 75.7pM, PDI is both a dye and an semiconductor

To further improve on sensitivities studies have demonstrated the detection of wavelength shifts down to 1.5 pm through the use of signal processing methods using statistical methods applied to averages of multiple independent measurements [111]; Previous work done with the Tr and BBEHP-PPV DFB lasers have operated under spectral resolutions 100x higher than this.

1.9 CONCLUSION AND PROJECT OUTLINE

As DFB lasers have already been demonstrated to operate as biosensors and amine presenting polyelectrolytes have been shown to deposit on their surface producing measurable shifts in the central emission wavelength and enabling further bioconjugation, they are a promising candidate for biosensor development. The highly reactive nature of the amino group in a polyelectrolyte such as PPL deposited onto the surface of an OS-DFB laser allow for a variety of surface modifications for probe immobilisation. The reaction partners traditionally used in amine ligations are not commercially available with oligonucleotide probes but click chemistry has been shown to be an effective protocol for DNA/RNA modification and immobilisation strategies.

In that context, the main objective of this project is to demonstrate an OS-DFB laser sensor using click chemistry. If achieved, this would pave the way for a novel oligonucleotide detection platform with great potential for robust CVD diagnostics at the POC, and contribute to the overarching aim of this research, which is to advance the field of OS-DFB laser biosensing with a POC laser biosensor for rapid and inexpensive detection of CVD.

By using the amine reactive cross-linker chemistry to modify a surface layer of PPL on an OS-DFB laser to present azido/alkyne groups; oligonucleotides modified with the opposing click chemistry reaction partner could be immobilised on the surface. Exploiting the specificity of the biochemistry related to oligonucleotides; these probes on an OS-DFB laser surface should allow biochemical interactions with target biomarkers to be detected in a sensing region localised to the OS-DFB laser surface.

Chapter 2 goes in more details in the concepts and the theoretical biosensing capabilities of OS-DFB laser sensors. The gain materials are presented and the surface functionalization approach discussed before a theoretical model, used in the discussions of later Chapters, is presented.

Chapter 3 outlines the experimental work done to characterise OS-DFB lasers fabricated of different OSs and assess them as potential biosensors building on work by A.M. Haughey [4, 89]. The experimental set-up for optical pumping is described before the results of assessing the effects of OS-DFB laser immersion and surface biochemical interactions on the wavelength and threshold fluence of devices is explored in detail.

Chapter 4 goes on to detail the surface functionalisation protocols used to employ OS-DFB's as biosensors and the use of SERS and silver nanoparticles (AgNPs). The previously unconfirmed functionalisation protocol is outlined and a confirmation study using SERS is presented along with an analysis of an AgNP labelling strategy to employ OS-DFB lasers as Oligonucleotide biosensors.

Chapter 5 concludes this thesis with an overview of the work and some suggestions on future avenues of research to improve the technology.

Chapter 2

ORGANIC SEMICONDUCTOR DFB LASERS: CONCEPTS, FUNCTIONALIZATION AND MODELLING

2.1 INTRODUCTION

While SPR and Photonic Crystal Resonators discussed in Chapter 1 are passive structures the OS-DFB laser is an active resonator which can be used for sensing applications. DFB lasers have been seen in both industrial [112-114] and biosensing applications [15, 111, 115, 116]. In work presented by Lu et al. [88]. an organic gain material imprinted with a grating structure forms the basis of an organic DFB laser biosensor that changes emission wavelength in response to shifts in refractive index in the environment of the DFB laser cavity. By functionalising the surface with probes specific to a desired biomarker, the OS-DFB laser output can detect binding events when the surface is exposed to samples containing the biomarker(s) of interest. The main design considerations for these devices to be used as biosensors is their sensitivity to the refractive index shifts being experienced, their resolution and the pump fluence which is required to achieve lasing. The resolution of a laser sensor is high thanks to the coherent, narrow emission of such a device. And as mentioned in Chapter 1, a laser resonator sensor enables maximisation of the sensitivity without compromising on the resolution. The higher the sensitivity and the better the resolution, the lower the LOD will be. The lower the pump fluence the less power will be required to run the OS-DFB which has implications for efficiency and the miniaturisation, hence for the portability of the device.

In this Chapter, the laser material and device concept are first discussed. The OS materials used as gain materials in OS-DFB lasers studied in later Chapters, and their characteristics relevant to laser sensing, are listed. Then, approaches to surface functionalization are briefly presented. In particular, the concept of the click chemistry approach is explained in more details than in Chapter 1, and the rationale for its use as the functionalization approach for the OS-DFB laser is given. Finally, the analytical model of the DFB laser biosensor, used in discussions of the results of Chapters 3 and 4, is explained

2.2 DISTRIBUTED FEEDBACK LASERS

The DFB laser platform in this work, schematized in Figure 2.1, is an optically pumped grating structure imprinted into a planar waveguide made of an optical gain medium. The grating satisfies the Bragg condition for laser oscillation so the grating coupled waveguide with the optical gain produces laser action. These devices have been shown to be sensitive to changes in the refractive index in regions surrounding their grating/waveguide cavity. This effect occurs as the evanescent field of the laser mode extends spatially to the surrounding region very close to the surface (see Figures 1.5 and 2.1 where this region is called the superstrate). In this manner DFB lasers can be employed as evanescent sensors [15, 89, 117] for biosensor development. Primarily, the lasers consist of a Bragg grating formed from a corrugated interface [118] on a planar waveguide providing 180-degree reflection to waveguided light in a narrowband of wavelengths relative to the periodicity of the grating denoted by a red Λ. In this work the corrugation is at the gain material/substrate interface.

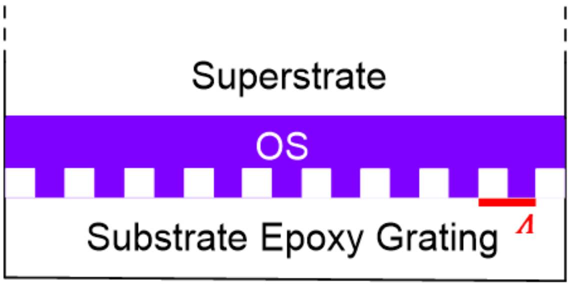

Figure 2.1 OS-DFB schematic showing the superstrate layer, thin film slab waveguide OS gain layer, substrate epoxy layer and a red bar marking the grating periodicity Λ.

The layers above and below the OS gain material must have lower refractive index to produce a slab waveguide. Ignoring the grating structure at the substrate interface, some of the light generated within the OS thin film is guided by total internal reflection, following a repetitive path, e.g. as described in Chapter 2 of Foucher's Thesis [119], and confined within the OS film. In this ray representation, a ray that can propagate is called a transverse mode. The number of such modes is discrete because there is a condition on the phase of the field (the transverse interference condition), and these modes, if they exist, are either transverse electric (TE) or transverse magnetic (TM) polarized. Each mode is also characterised by an effective refractive index, denoted $\boldsymbol{n_{eff}}$, which depends on the thickness of the gain material, the wavelength and the refractive indices of the planar structure (substrate/OS/superstrate).

The film thickness of the gain material must be sufficient so that it provides propagation of at least 1 transverse mode at a wavelength within the OS gain spectrum to produce laser action. When the refractive index of the substrate and superstrate are not equal then there is a cut-off thickness below which no transverse mode is guided and the OS-DFB structure will not produce laser action. Increasing the thickness way above this cut-off will allow multiple modes to be supported for waveguiding and make interpreting the output spectra more complex. There is therefore a balance to be found on the thickness so that only one or a few propagating modes exist, and single-mode laser oscillation is favoured.

2.2.1 OPTICAL GAIN AND LASER OSCILLATION

A guided mode is able to interact with the gain material. Consider the OS as a 4-level system (see Figure 2.2). There are 2 electronic energy levels of the material, $\boldsymbol{E_1}$ and $\boldsymbol{E_2}$, defining the laser transition. Spontaneously emitted photons at this transition have the frequency $\boldsymbol{\upsilon_0}$ defined as in Eq. 2.1 [120], the difference between the Energy levels divided by Plank's constant $\boldsymbol{h}$.

$$\boldsymbol{\upsilon_0 = (E_2 - E_1)/h} \qquad \textbf{Eq. 2.1}$$

Some of the spontaneously emitted photons couple to the guided mode and can then be amplified by stimulated emission as they are waveguided in the gain medium. These incident photons of frequency $\boldsymbol{v_0}$ have a finite probability to force the decay of an OS molecule in the E_2 state to E_1 emitting identical photons (same frequency $\boldsymbol{v_0}$, same polarization and same direction) in the process. Of course, photons can also be absorbed by the same transition. For the cascade effect of optical gain as the photons travel in the gain medium, stimulated emission needs to be more likely to happen than absorption. This is the case when the so-called condition of population inversion is satisfied. Defining the population of electrons in these two different Energy levels as N_1 and N_2 the condition of population inversion is given as $[N2 < N1]$[120].

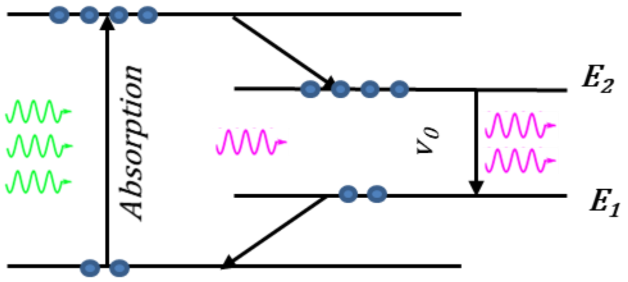

Figure 2.2 – Schematic representing a 4 level energy system where the laser emission transition occurs between the 3rd (E_2) and 2nd (E_1) levels

With pumping into a higher energy level (see Figure 2.2), this population inversion can be created and maintained and stimulated emission will amplify the waveguided spontaneous emission (optical gain). The optical gain is proportional to the population inversion $N2 - N1$. This leads to amplified spontaneous emission (ASE) and, used in combination with the grating-coupled waveguide principles to reflect light back and forth within the gain material, will produce laser emission. In this manner a thin film of gain material with an ASE peak wavelength matched to the waveguiding Bragg condition for an imprinted grating structure forms a DFB laser. This theory also holds for a 3-level system where the lasing transition occurs between the 2nd and 1st levels.

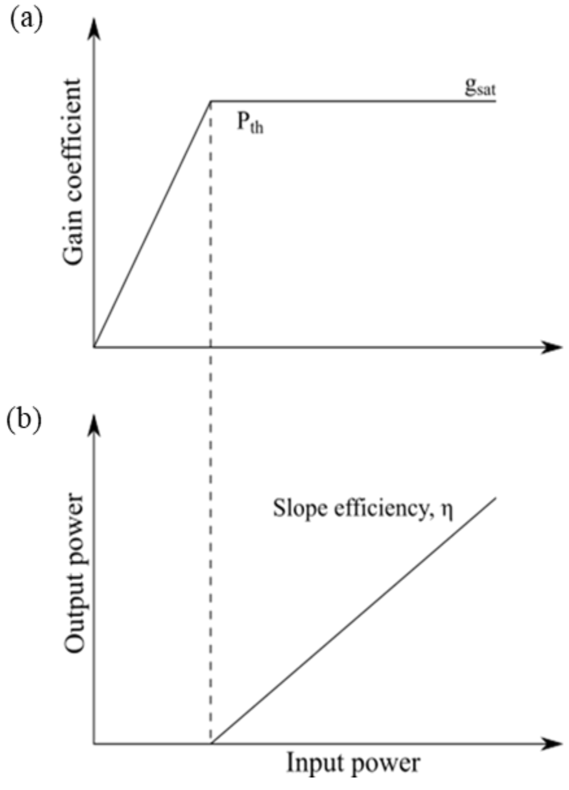

Figure 2.3– (a) Optical gain coefficient versus pump power or energy and (b) laser output versus Pump (Input) level, showing the slope efficiency above threshold.

The pump energy needed to reach laser oscillation is higher than the one leading to the population inversion condition because losses, including cavity losses needed for the laser output (outcoupling), are also present. The pump energy for which the optical gain compensates for these losses is called the laser threshold. At this point the overall gain of the mode (the net gain) becomes positive. Below threshold the population inversion and therefore the optical gain increases linearly with the pump excitation. Just at or above threshold the mode intensity increases exponentially as it resonates in the cavity to a point, called gain saturation, when it becomes strong enough to deplete the population inversion. Therefore, to a first approximation, the optical gain clamps at threshold. Above threshold, any additional pump energy is transferred to the laser emission. This explains the typical transfer function of a laser as shown in Figure 2.3(b), where the slope of the curve is the laser output versus the pump energy above threshold. At threshold, the emission spectrum also narrows dramatically (compared to the luminescence spectrum of the gain material below threshold) due to the combination of the frequency selective optical cavity and the effect of stimulated emission. As noted, this narrow laser emission is advantageous for sensing. As will be seen in this thesis, the threshold can also be used as an indicator for sensing

2.2.2 *BRAGG GRATINGS*

The DFB lasers in this work are so-called 2nd order DFB lasers and emit vertically. A 2nd order DFB laser operation is governed by the Bragg Equation of Eq. 2.2, where $\boldsymbol{n_{eff}}$ denotes the effective refractive index of the DFB structure seen by the laser mode with wavelength of operation ($\boldsymbol{\lambda}$).

$$\boldsymbol{n_{eff}\lambda = 2\Lambda\sin\theta} \qquad \textbf{Eq. 2.2}$$

When optically pumped with fluence greater than the threshold energy (sufficient to generate a population inversion within the gain material and to compensate for the cavity losses), the devices emit a laser beam with a wavelength of $\boldsymbol{\lambda}$ given by Eq. 2.2. By changing the thickness of the layer of gain material and so tuning the effective refractive index of the transverse modes, OS-DFB lasers can be fabricated for single-moded operation. In a 2nd order DFB the light is diffracted at $\theta = 90°$ to the plane of the interface (the outcoupled laser emission therefore exits the cavity vertically and $\sin\theta$ can be ignored) and also at 180º for feedback.

Different approaches can be taken to make a DFB laser sensor. Early implementations of the technology used dye incorporated polymer lasers [121-123] and more recently gratings imprinted in optically active OS gain materials. Spin-coating solution processable semiconductor material onto an epoxy grating (as was done in this work) allows the fabrication of flexible, low threshold devices sensitive to superstrate shifts in refractive index resulting from material adsorption. Depending on the material being used a solution of the gain material was dropped onto a polymer grating and then spin-coated across the grating at the appropriate speed to produce a thin film of the desired thickness.

As discussed in Chapter 1, implementations for sensing using dye-doped polymers as the gain material and achieved a threshold pump fluence of 180 $\mu J.cm^{-2}$ (10ns pump pulses) and a bulk sensitivity (measured in nm/refractive index unit, RIU) of 16.6 $nm.RIU^{-1}$ [88]. This sensitivity was improved upon with the inclusion of a TiO_2 cladding layer, >154$nm.RIU^{-1}$ [97], and the use of dye materials with a higher refractive index, 32nm.RIU^{-1} [47], although the addition of the TiO_2 cladding layer this caused a rise in the threshold pump fluence that would be disadvantageous for miniaturisation of a device

2.2.3 ORGANIC SEMICONDUCTORS

Organic semiconductors (OS) are another class of organic gain material [98] which have been used for fabricating DFB lasers [92]. These include for example materials such as Tr [91], a star shaped oligomer which forms a monodisperse layer in the solid state, and conjugated polymers such as the PPV derivatives BBEHP-PPV and the commercially available SY. Without the incorporation of a top cladding layer Tr-DFB lasers by Haughey et al. have achieved a sensitivity of 20 nm/RIU for a pump fluence as low as 60 μJ.cm^{-2} which is an improvement on their dye based counterparts. Immersing the laser in water was found to lower this threshold further to 30 μJ.cm^{-2}.

In general, OSs have higher refractive indices which should result in greater confinement of the evanescent field around the gain layer and make them more appropriate for surface sensing applications. This is because a greater confinement enables, with careful choice of the waveguide thickness, an increase of the modal field strength in the region very close to the laser surface. SY, BBEHP-PPV, and Tr were the OSs primarily investigated as part of this thesis and their main characteristics are listed in the following sections comparing and contrasting their properties in the context of suitable OS-DFB gain layer material. AFM measurements, where a small cantilever drags across the surface of a sample measuring the force between the probe tip and the surface, can be used to investigate thickness variations, were used to measure the thicknesses of the OS gain layers.

2.2.3.1 Super Yellow

The chemical structure of Super Yellow (SY), a PPV derivative from Merck, can be seen in Figure 2.4(a). SY has an absorption spectrum peak, shown in Figure 2.4(b), around 450nm which is the emission wavelength of an efficient InGaN Laser Diode (LD). SY is stated to have a refractive index of around 1.8 [124] which is closer to that of Tr [125] than the lower 1.64 of BBEHP-PPV [126] which, according to the model (see section 2.4), indicates that that OS-DFB laser based evanescent sensors fabricated with SY would have a higher sensitivity than those of BBEHP-PPV for a film of similar thickness.

Experiments with the SY material in a similar fashion to BBEHP-PPV and Tr based OS-DFB laser protocols proved to be difficult as the material was not as easily soluble as the alternatives and tended to form a gel which was unsuitable for the spin-coating fabrication of single-moded OS-DFB lasers. L Maclellan [103] was able to fabricate single moded SY-DFB laser using Dimethyl Sulphoxide (DMSO) in place of Toluene as the OS solvent but the linewidth and beam profile in preliminary experiments with these devices weren't suitable for repeatable and reliable analysis required for the development of a biodetection platform.

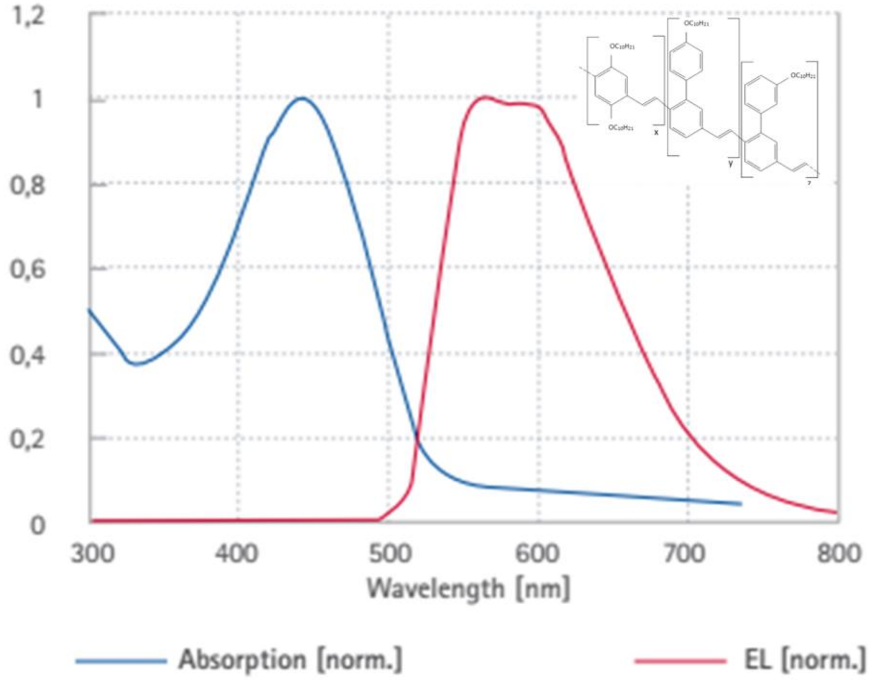

Figure 2.4 - Absorption and emission spectra of SY material from Merck SuperYellow datasheet. Inset showing chemical structure of SY

2.2.3.2 BBEHP-PPV

Recent work with poly[2,5-bis(20,50-bis(200-ethylhexyloxy)phenyl)-p-phenylene vinylene] (BBEHP-PPV, obtained from the Skabara group formerly of University of Strathclyde) has shown that it is a more suitable candidate for LD-pumping [127, 128] than other OS gain materials. The plot of the absorption spectrum of BBEHP-PPV along with the emission spectrum (photoluminescence) is shown in Figure 2.5, the second peak in the PL curve is actually one of several attributed to exitonic vibrations, which gives rise to several distinct peaks separated by a factor related to the frequency of the vibration, separated by 4.41 aJ. The absorption peaks in the blue spectral region, which matches the output of InGaN LDs (typically 405 nm or 450 nm). The absorption is higher in this region than for Tr and, as a result, the threshold energy (E_{th}) required for lasing under LD excitation will be lower.

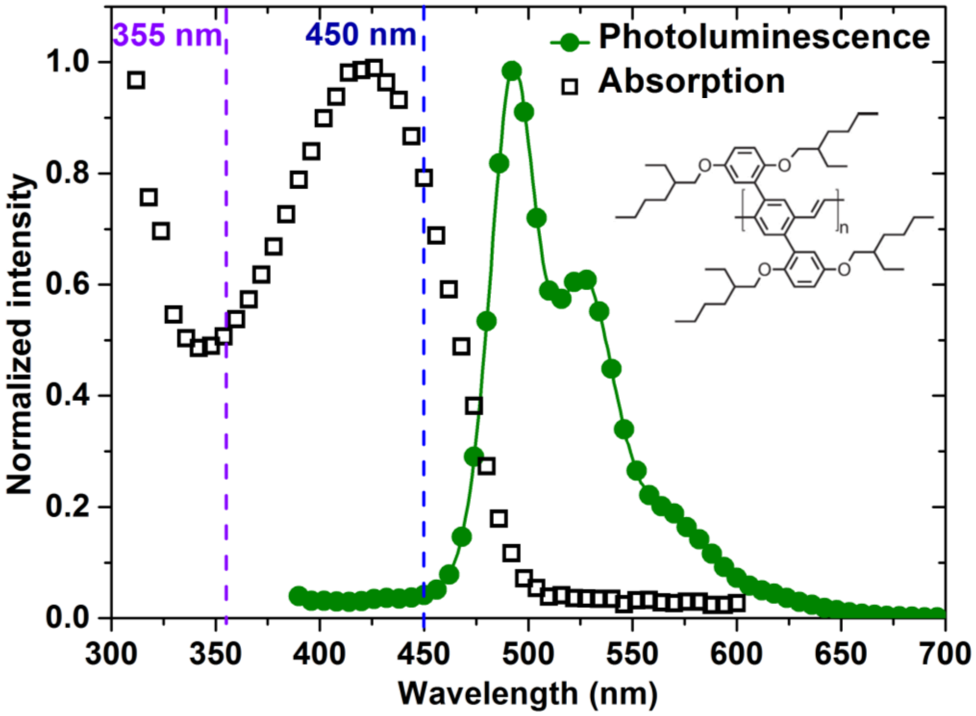

Figure 2.5 - Absorption and PL spectrum for BBEHP-PPV polymer, obtained from thin film samples, with Nd:YAG (355 nm) and InGaN (450 nm) pump wavelengths marked and an inset showing the chemical structure.

BBEHP-PPV-DFB lasers in this work were fabricated by forming 100-300nm thick nanofilm of the neat, green emitting, π-conjugated polymer (with a refractive index of 1.64 [126]) on an epoxy grating with a periodicity Λ = 350 nm and a 5mm by 5mm surface area. The film was obtained by spin-coating, at 1.5-6.0 krpm, 25 μl of a 20mg.ml^{-1} Tr in toluene solution.

2.2.3.3 Truxene

Oligofluorene Tr, monodisperse star-shaped oligomers with high photoluminescence quantum yields and peak absorbance at 370 nm, has previously been used for the OS layer in OS-DFB based biosensors [24]. The structure and the PL/absorption plot can be seen in Figure 2.6. The multiple peaks of the PL curve can be attributed to excitonic vibrations as discussed for BBEHP-PPV separated by 9.93 aJ.

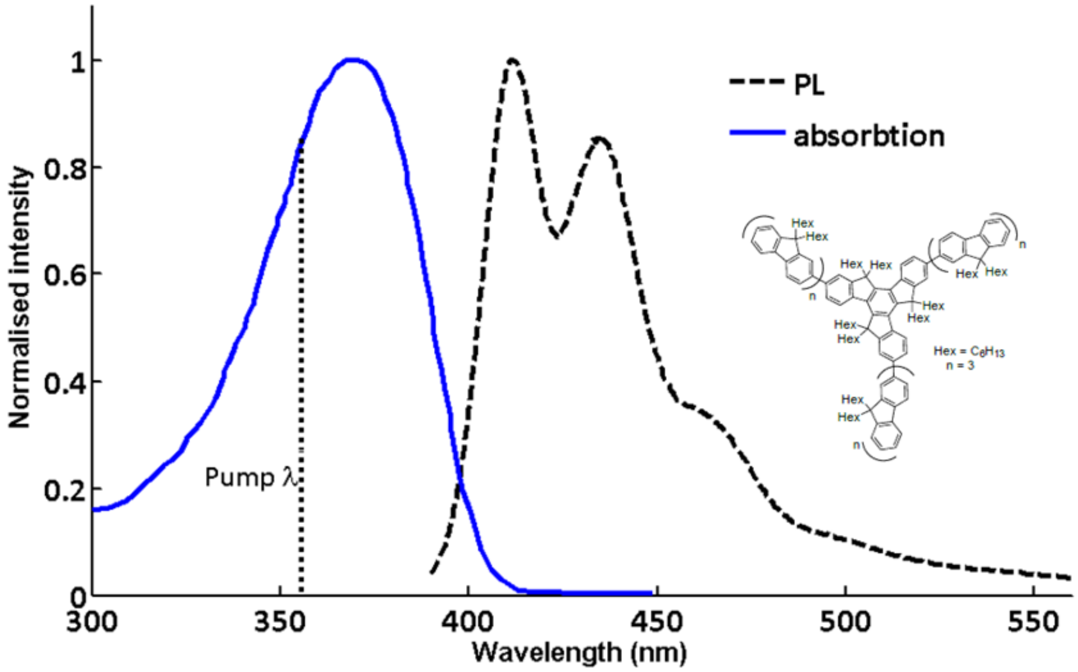

Figure 2.6 – Triflourene Tr moleculelar structure inset over Photoluminesence (PL) and absorption spectra, investigated in Tr thin films, with a dotted line indicating the Pump wavelength within the absorption peak.

Tr-DFB lasers were fabricated by forming ≈80 nm thick nanofilm of neat T3 oligofluorene-truxene star-shaped macromolecules, consisting of truxene core and three terfluorene arms [129, 130] (Tr) onto an epoxy grating with a periodicity $\Lambda = 276$ nm and a 5mm by 5mm surface area [92]. The film was obtained by spin-coating, at 3.2 krpm, 15 µl of a 20 mg.ml^{-1} Tr in toluene solution. The properties of Tr-DFB lasers are explored in work by A.M. Haughey but they typically produce lasers at 430 nm with a Full-Width Half-Maximum of 0.3 nm or less. Having reported threshold fluence of 60 µJ.cm^{-2} or 30 µJ.cm^{-2} immersed in water.

Like BBEHP-PPV, Tr was obtained from Skabara's group, formerly part of the Pure and Applied Chemistry Department, University of Strathclyde synthesised by attaching oligoflourene arms to the truxene core [131]. The thickness of Tr film produced by different batches as well as the surface morphology would vary. After a few weeks or months of use the lasers produced using the material would produce higher wavelength, less sensitive lasers with multimode samples also becoming more common. This is thought to be due to degradation from exposure of the Tr to the environment when weighing out material for DFB fabrication. Separating Tr into smaller batches so that there was only enough in each tube to make a few Tr-DFB lasers would save repeated exposure of unused material to the degradation from environmental conditions.

2.3 METHODS OF SURFACE FUNCTIONALISATION

Biomarkers such as micro-RNA [17-20], DNA [21-23] and proteins [24-27], are typically nanoscale molecules and the sensing strategies employed therefore have to operate at such scales. In order to do this, nanoscale molecular probes are typically anchored to a surface capable of detecting the biomolecular interactions which facilitate biosensor operation. In this section, explained briefly are methods used in the steps of surface functionalisation of the DFB laser and discuss click chemistry in more details.

2.3.1 ELECTROSTATIC & HYDROPHOBIC FORCES

Using localised charges at the surface of large molecules, coatings can be adsorbed onto sensor surfaces. The opposing charge of the surface material and localised regions of charge on the coating molecules can be exploited to deposit a surface coating from solution onto a device. In this way polyelectrolyte coatings have been deposited onto DFB lasers in experiments with stacked layers of oppositely charged polyelectrolytes while using the laser as an evanescent sensor detecting the material adsorption [89].

Physical adsorption can also be obtained on neutral surfaces due to spatially localised charges and/or by attractions of hydrophobic segments. Tr gain layers are electrostatically neutral but hydrophobic regions of the surface of a protein in solution will be driven together with hydrophobic regions of a surface due to the thermodynamic driving force which pushes to reduce the hydrophobic surface regon exposed to the solvent [132]. In Chapter 3 an amine presenting polyelectrolyte layer is deposited on a Tr-DFB laser surface in this manner and terminal amines are used to covalently anchor click chemistry reactive groups via amine ligation with N-Hydroxysuccinimide (NHS) esters. The following sections will outline these covalent strategies.

2.3.2 COVALENT STRATEGIES

Stronger than electrostatic and hydrophobic attractions are covalent bonds. These involve mutual attractions of atomic nuclei to the orbital electrons and are much harder to overcome than electrostatic forces on molecular surfaces. Explored in this work are methods for thin film surface modification using commercially bought chemicals. Unless otherwise stated all materials were purchased from Sigma-Aldrich or Thermo Fischer.

2.3.2.1 Amine Reactive Cross-linkers

Amine reactive cross-linkers are well-documented, commercially available, covalent attachment strategies [133, 134]. Amino groups are known to be very reactive and naturally make ideal reaction sites for side chain modifications in organic chemistry. There are a number of different reaction partners which can be chosen. NHS esters will react to form amide bonds, as seen in Haughey's work with NHS-biotin, in slightly alkaline conditions. This same mechanism has been used for the investigation presented in Section 3.4.1 of this thesis. There is also a class of sulfo-NHS esters which have increased water solubility [133], while this could potentially allow for a simplified attachment strategy of the oligonucleotide probes directly onto the amine presenting PPL layer there is currently no commercially available sulfo-NHS labelled oligonucleotide sources. The esters involved typically react with the amino branches found in lysine to form amide linkages.

2.3.2.2 Click chemistry

Click chemistry has become a useful paradigm in material science. It is used to form, functionalise and control the structure of a range of materials from the nanoscale to the macro-scale enabling, among other things, surface functionalization for biosensing. The idea of click chemistry is based upon the optimisation and simplification of robust chemical reactions. Reactions that can happen under mild conditions and which are orthogonal, i.e. that do not create unwanted side products.

The spark that has driven the development of click chemistry has stemmed from a desire to simplify the process of synthesising robust organic compounds as the desire for increasingly more complex compounds arose [135]. While many of the click reaction families have been used in small molecule synthesis in some way or another, they have also been seen to be of great benefit to the field of material science. The versatility of the protocols has proven them valuable assets in material synthesis and surface/material/polymer modifications. Each reaction that falls within the scope of click chemistry comes with its own mechanism of operation and advantages and disadvantages to consider.

Click chemistry was first coined in 2001 [135]; really taking off as a field of investigation after 2 publications [136, 137] in 2002 describing CuAAC (Cu(I) catalysed 1,3-dipolar azide-alkyne cycloaddition), the click chemistry used in this work, where Cu(I) catalyses the reaction, forces the synthesis of the 1,4-regioisomer (see Figure 2.7, reaction (1)). Other than this 6 main click chemistries are identified in a paper by Xi, Scott [68], depicted in Figure 2.7; namely, (2) Diels-Alder addition, (3) Thiol-vinyl addition(also known as Michael addition), (4) Thiol-yne, (5) Thiol-isocyanate, (6) Oxime/Hydrazone formation, (7) 1,3 Dipolar cycloaddition a more general form of (1).

Diels-Alder cycloaddition [138] forms a cyclohexene adduct from the reaction between a diene and a dienophile as shown in reaction (2) in Figure 2.7. The most widely used of the click chemistries for applications from block copolymer synthesis to self-healing materials [68]. The drawback of the Diels-Alder cycloaddition is that typical reactions require temperatures in excess of 100 ºC for long periods of time to achieve a good yield. A bioorthoganal approach is reported by Blackman et al. [139] which involves the reaction of a tetrazine and a strained alkene/alkyne, known as the inverse electron demand Diels-Alder reaction.

Reaction (3) in Figure 2.7 is a common thiol-ene click chemistry reaction between a thiol and a vinyl [140]. With the introduction of radicals, a carbon centred radical is formed from the addition of a thiyl radical to a vinyl. This carbon centred radical abstracts a hydrogen from a thiol to produce a thioether product and a thiyl radical. This, ideally, creates an alternating sequence of addition and hydrogen abstraction reactions [68]. This reaction is very sensitive to environmental conditions however if carefully selected allow for a robust click reaction which has many applications [68]. Low initiator concentration, 1 or 2 orders lower than the functional group, uniform light intensity with little attenuation, no solvents prone to chain transfer reactions, extremely low oxygen levels and choosing the -ene to reduce homoplymerization [141].

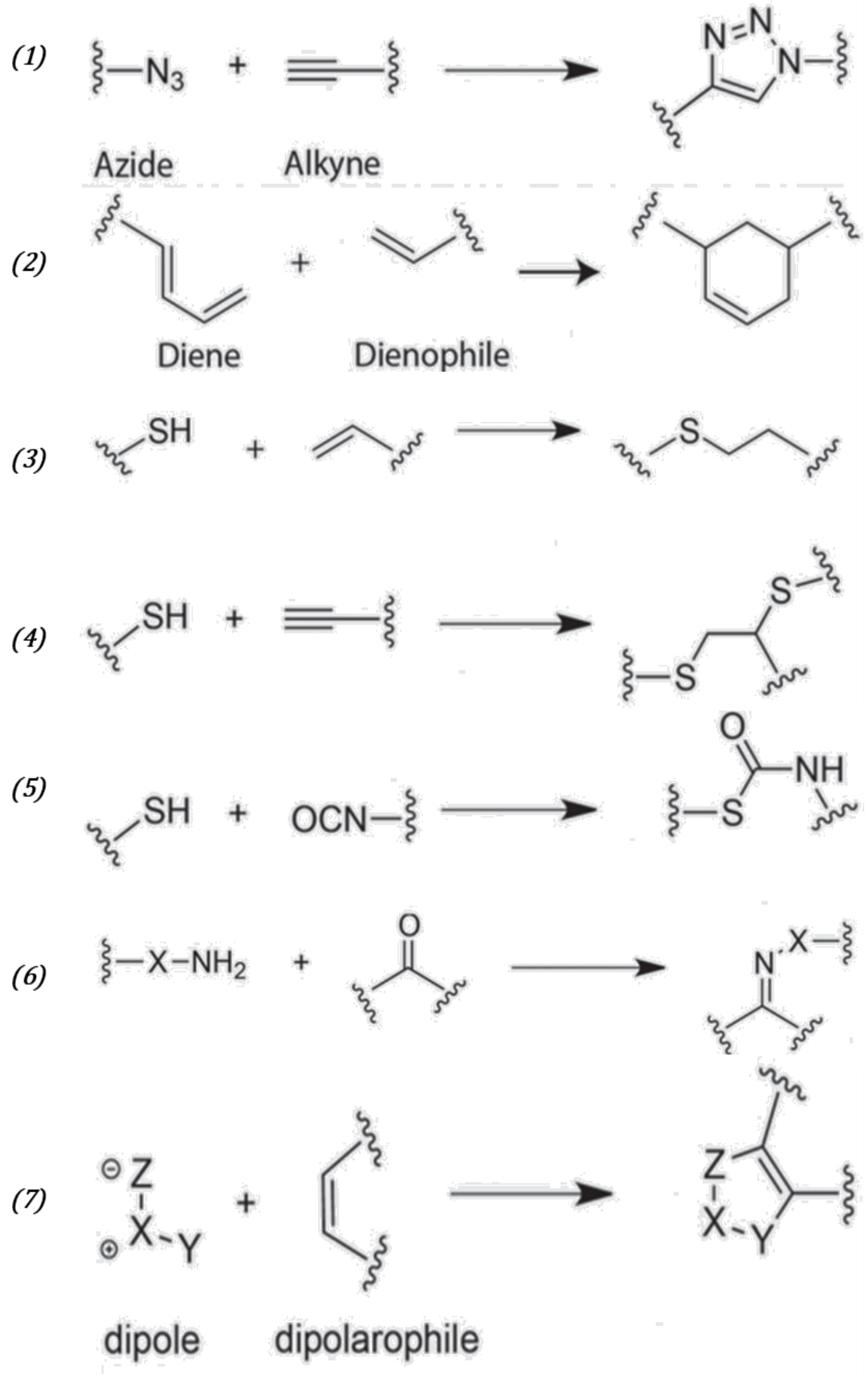

Figure 2.7 – 7 basic reactions of different click chemistries (1): Azide-alkyne cycloaddition, (2): Diels-Alder addition, (3): Thiol-vinyl addition, (4): Thiol-yne, (5): Thiol-isocyanate, (6): Oxime/Hydrazone formation (7): 1,3 Dipolar cycloaddition.

Reactions (4) and (5) in Figure 2.7 are also thiol based click chemistry reactions. The mechanisms which define (4) are very similar to (3) except the alkyne is capable of reacting with two thiols and so they must be reacted in a 2:1 ratio [142]. These reactions result in an increased network connectedness in comparison to the thiol-ene counterparts, however, for certain alkyne structures there is no second thiol addition [68]. Reaction (5) is the thiol-isocyanate addition which is classified under the click chemistry banner due to its high yields under moderate reaction conditions [143]. This decades old thiol reaction can work with many substrates but at the expense of orthogonality as it can produce unwanted products, however this can be controlled via catalyst selection, reaction order and conditions.

Reaction (6) from Figure 2.7, Oxime/Hydrazone formation reactions form reversible imine bonds from the condensation reaction between a aldehyde/ketone with nucleophilic amines [68]. The reaction is chemoselective and will proceed with other functional groups in biomolecules, the rate can be enhanced by protic or nucleophilic catalysts [68]. (7): 1,3 Dipolar cycloaddition has been shown to proceed rapidly in a few minutes under photoactivation with UV, modifying a protein and demonstrating bio-orthogonality [144]. A reaction of this kind utilizing nitrile oxides quickly achieved complete conversion at ambient temperatures in DNA modification. Nitrile oxides are highly reactive and their inclusion in a protocol could result in the loss of selectivity and orthogonality [68].

In this work, click chemistry refers to the reaction between an azido (N_3) and an Alkyne (C≡C) group creating a strong and reactively stable covalent bond. Traditionally performed in the presence of Cu(I) ions known to catalyse the reaction between the 2 groups, other protocols have shown that a copper free alternatives are possible [138, 145-147], due to Cu(I) toxicity these provide a bio-orthogonal alternative to CuAAC.

CuAAC is commonly performed using Cu(II) ions in the presence of reducing agents as a source of Cu(I) ions, since Cu(I) is unstable. An alternative source, Cu(I) halides, have been demonstrated to increase the yield of unwanted side products [148]. Stabilizing ligands can also be used to inhibit the oxidation and disproportiation of the ion without preventing catalysis of the azide-alkyne cycloaddition [149]

Using this protocol for surface immobilisation the desired modifier, labelled with either an azido or alkyne group, can be covalently immobilised on a surface presenting the other. In this manner the specificity of click chemistry protocols is much greater than alternative covalent attachment strategies. Amine Ligation for example lacks specificity since terminal amine groups are highly reactive with a number of different partners [134]. The necessity for tight controls on the reaction conditions can also be considered a drawback but work continues to develop more environmentally stable derivations of the protocol while maintaining the specificity of the azide-alkyne pairing.

DFB lasers employed as evanescent sensors [15, 88] have been shown to be responsive to changes in refractive index due to material absorption down to the nanoscale [86] and encapsulation experiments [90] have shown that the threshold of the DFB lasers are also responsive to changes in material adsorbed onto the device surface. Devices with a narrow linewidth, they operate as active resonators that can be adapted to biosensor applications. While this could be achieved through other strategies click chemistry benefits from a specific reactant pairing and in this work the Hiusgen [3+2] CuAAC reaction between a terminal alkyne and an azide [150] is used to anchor probes into the sensing region of an DFB laser.

2.4 DFB LASER MODELLING

A (Mathcad) matrix based model [89] of planar waveguide operation was used to calculate the wavelength and sensitivity of the laser mode in bulk refractive index sensing. This matrix based model was extended to investigate the intensity profile of the laser mode in order to understand and explore the optimisation of devices. A full mathematical description of the model is described elsewhere [151] but a brief summary of the key details are provided here.

To optimise the film thickness and sensitivity of the OS-DFB lasers; Mathcad was used to model the relationship between the refractive indices of different components of the OS-DFB laser and the effective refractive index of the structure. The relationship to both the wavelength of the laser action through the effective refractive index and the distribution of the evanescent field throughout the laser structure were also investigated.

Tr and BBEHP-PPV were the gain materials used to investigate the biosensing application of OS-DFB lasers. The Tr layer of an OS-DFB has a refractive index (n_{Tr}) at λ_o of $n_{Tr}\approx 1.81$ [125] and the grating periodicity used experimentally was 276nm selected as a result of Bragg's Law relating the effective refractive index of the whole structure (n_{eff}) to the periodicity and wavelength of operation ($\boldsymbol{\lambda_o}$) in the 430nm region where a PL peak for Tr is found (it is also the wavelength at which ASE preferentially develops in Tr thin films). BBEHP-PPV on the other hand has a refractive index of 1.64 [126] with a PL peak (and its ASE peak) around 540nm. Manufacturers data determined the Norland epoxy substrate to have a refractive index determined by the Cauchy formula [152] shown in Eq. 2.3,

$$\boldsymbol{n(\lambda) = B + \frac{C}{\lambda^2} + \frac{D}{\lambda^4} + \cdots} \qquad \textbf{Eq. 2.3}$$

Here the **B**, **C** and **D**…. values correspond to coefficients determined by fitting the equation to measured values at known wavelengths.

2.4.1 *ACTIVE LAYER THICKNESS*

The wavelength of operation $\boldsymbol{\lambda_o}$ of an OS-DFB laser sensor in the presence of 2 different superstrates from bulk sensing experiments allowed calculation of expected $\boldsymbol{\Delta\lambda}$ induced at varying active layer thickness. Using the refractive index of the various layers of the DFB structure and the sensing medium the effective refractive index ($\boldsymbol{n_{eff}}$) in response to changes in the active layer thickness was calculated as seen by different TE and TM modes. The calculated $\boldsymbol{n_{eff}}$ values could then be substituted into the Bragg equation to determine the wavelength of operation for the supported modes at different active layer thicknesses. As previously discussed in Section 2.2.2, the $\boldsymbol{sin\theta}$ term in Eq. 2.2 for operation of a 2nd order DFB laser equates to 1, rewriting here the Bragg condition for mode $\boldsymbol{m}$ in Eq. 2.4 is

$$\boldsymbol{m\lambda = 2n_{eff}\Lambda} \qquad \textbf{Eq. 2.4}$$

By modelling the output of the laser in response to gain layer thickness, grating periodicity, refractive index of the superstrates/gain layer/substrate, the expected wavelength of operation and the sensitivity of it in response to refractive index variations could be determined to optimise the device fabrication.

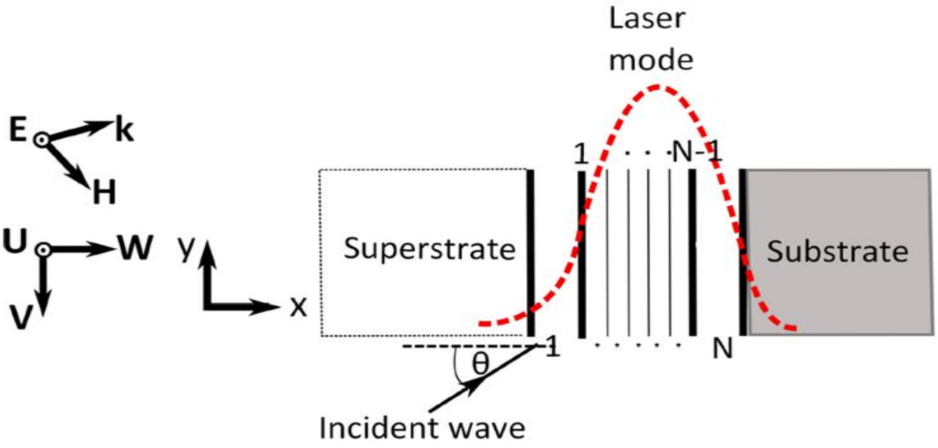

Figure 2.8 - Multilayer stack of N thin films bound by practically infinite substrate and superstrate layers. Laser mode distribution across the structure is represented with N representing the active layer.

2.4.2 *MODE DISPERSION MATRIX*

The OS-DFB laser is represented as a multi-layer structure in Figure 2.8. A laser mode can be approximated as a waveguide mode of this multi-layered structure oscillating at the frequency of maximum gain provided by the laser material. The laser gain layer and any other layers adjacent to the gain layer (with layer 1 being the topmost layer adjacent to the superstrate and layer N being the Tr layer) are enclosed between semi-infinite superstrate and substrate layers. This multilayer approach enables to model a DFB laser sensor, where the OS gain and adsorbed material (probes and/or biomarkers) each corresponds to a layer.

The boundaries between layers 1 to N are numbered 1 to N−1. The direction cosines are given by $\boldsymbol{\alpha} = \boldsymbol{n}\,\boldsymbol{cos}\,\boldsymbol{\theta} = (\boldsymbol{n}^2 - \boldsymbol{\beta}^2)^{1/2}$ and $\boldsymbol{\beta} = \boldsymbol{n}\sin\boldsymbol{\theta}$ as indicated in Figure 2.8, and where $\boldsymbol{\beta}$ is the propagation constant. Properly designed OS-DFB lasers oscillate on the fundamental TE_0 mode and therefore the model is designed to solve for the TE_0 mode only, although it can equally be applied to other modes, including TM modes. The plane of incidence is the xy plane and the interfaces between the layers of the OS-DFB laser are parallel to the yz plane. Therefore, the only material variation for the stack of layers occurs in the x-direction. For a TE wave, E_x and E_y, and therefore H_z, are equal to zero and E_z, H_y and H_x are given by

$$\boldsymbol{E_z = U(x)e^{i(k\beta y-\omega t)}} \quad \textbf{Eq. 2.5}$$

$$\boldsymbol{H_y = V\,(x)e^{i(k\beta y-\omega t)}} \quad \textbf{Eq. 2.6}$$

$$\boldsymbol{H_x = W(x)e^{i(k\beta y-\omega t)}} \quad \textbf{Eq. 2.7}$$

The relationship between the transverse amplitudes of the field components, ***U(x)*** and ***V(x)***, is given by the following equations where $\boldsymbol{\gamma}$ ($\boldsymbol{\gamma = \frac{ncos\theta}{z0}}$) can be defined as $\boldsymbol{\gamma = \frac{\alpha}{c\mu}}$ in non-magnetic media, where $\boldsymbol{c}$ is the speed of light and $\boldsymbol{\mu}$ is the magnetic permeability. At the boundary between two adjacent layers the tangential components of the electric and magnetic fields (**U** and ***V***) are continuous and ***W***, the amplitude of the component normal to the boundary between the layers, is proportional to ***U***. The total field can therefore be specified using the pair of simultaneous equations for ***U*** and ***V*** given by

$$\boldsymbol{\frac{dU}{dx} = \frac{ik\alpha}{\gamma}V} \quad \textbf{Eq. 2.8}$$

$$\frac{dV}{dx} = ik\alpha\gamma U \qquad \text{Eq. 2.9}$$

The knowledge of U and V at any boundary of the multilayer is sufficient to describe the entire transverse field using a transfer matrix M. The particular components of matrix M for the stack of N layers between position x_n and x_{n-1} are given by matrix M_n in Eq. 2.10 where Φ is the phase thickness of the layer and is given by $\Phi_n = k\alpha_n (x_n - x_{n-1})$.

$$M_n = \begin{pmatrix} \cos\Phi_n & \frac{-i}{\gamma_n}\sin\Phi_n \\ -i\gamma_n \sin\Phi_n & \cos\Phi_n \end{pmatrix} \qquad \text{Eq. 2.10}$$

Each of the N layers of the multilayer stack is described by a matrix resembling Eq. 2.10 The transfer matrix (M) combining all of the N layers is given by the product of each of the matrices for the respective individual layers,

$$M = \prod_{n=1}^{N} M_n = \begin{pmatrix} m_{11} & m_{12} \\ m_{21} & m_{22} \end{pmatrix} \qquad \text{Eq. 2.11}$$

Eq. 2.11 enables the determination of the guided modes, i.e. the waves that are guided inside the multilayer structure in the y-direction. In the OS-DFB laser model presented here, the lowest order waveguided modes represent the laser mode (it overlaps the gain region, propagates in the y-direction and interacts with the grating resulting in the feedback required for laser emission). A wave propagating within the stack of N layers, as depicted in Figure 2.8, is confined between the substrate and superstrate layers by total internal reflection. For waveguided fields, M must relate the field at the boundary between the superstrate and the layer $N = 1$; to the field at the boundary between the active layer and the substrate. Therefore, the fields at the stack boundaries are required to satisfy Eq. 2.12 where the subscripts sub and sup represent the substrate and superstrate, respectively,

$$\begin{pmatrix} U_{sup} \\ V_{sup} \end{pmatrix} = M \begin{pmatrix} U_{sub} \\ V_{sub} \end{pmatrix} \qquad \text{Eq. 2.12}$$

As the laser modes guided within the OS-DFB laser are bound between the semi-infinite substrate and superstrate layers, the field is evanescent in both the superstrate and the substrate, as shown in Figure 2.8. It is this evanescent part of the mode that is used to probe the region close to the laser surface for sensing. The waves are negative-going in the substrate and positive-going in the superstrate (radiation condition) such that $\boldsymbol{U = U_{sup}e^{(-ik\alpha_{sup}x)}}$ and $\boldsymbol{U = U_{sub}e^{(-ik\alpha_{sub}(x-x_{sub}))}}$ respectively. For waveguided modes, $\boldsymbol{\alpha_{sup}}$ and $\boldsymbol{\alpha_{sub}}$ are imaginary. Solving Eq. 2.12 for positive and negative traveling waves results in the modal-dispersion function $\boldsymbol{(\chi(\beta))}$ for bound modes,

$$\boldsymbol{\chi(\beta) = \gamma_{sup}m_{11} + \gamma_{sup}\gamma_{sub}m_{12} + m_{21} + \gamma_{sub}m_{22} = 0} \qquad \textbf{Eq. 2.13}$$

Eq. 2.13 can be solved numerically for $\boldsymbol{\beta}$, which is equivalent to the effective refractive index of the laser mode in the case of the OS-DFB laser described in Figure 2.8. Each solution of Eq. 2.13 corresponds to a waveguided mode, with the highest solution representing the lowest order waveguided mode for multilayer OS-DFB lasers. Once the effective refractive index of the TE_0 mode is found, the field distribution throughout the OS-DFB laser structure and the stack of N layers can be traced. To do this, one of the field amplitudes may be arbitrarily chosen at one point and Eq. 2.14 can be used to calculate the field amplitudes at other points of the structure relative to the initial chosen amplitude

$$\boldsymbol{\begin{pmatrix} U_{n-1} \\ V_{n-1} \end{pmatrix} = M_n \begin{pmatrix} U_n \\ V_n \end{pmatrix}} \qquad \textbf{Eq. 2.14}$$

Knowing the amplitudes at each of the layer interfaces, the mode profile, $\boldsymbol{E(x)}$, is calculated through the OS-DFB laser structure and the N layers, where $\boldsymbol{U(x)} = \mathbf{E(x)}$, for the TE mode.

2.4.2.1 Modelling Surface Sensing

Many molecular biomarkers can be probed using oligonucleotides; with complementary pair Hydrogen bonding for DNA/RNA or aptamers for proteins. Due to the evanescent sensing capabilities of OS-DFB lasers, if these probes were on the surface, they could theoretically capture specifically target biomarkers from a patient sample and by measuring the characteristics of the OS-DFB laser output it should be possible to observe biomolecular interactions as they are modifying the refractive index of regions localised where the evanescent field extends.

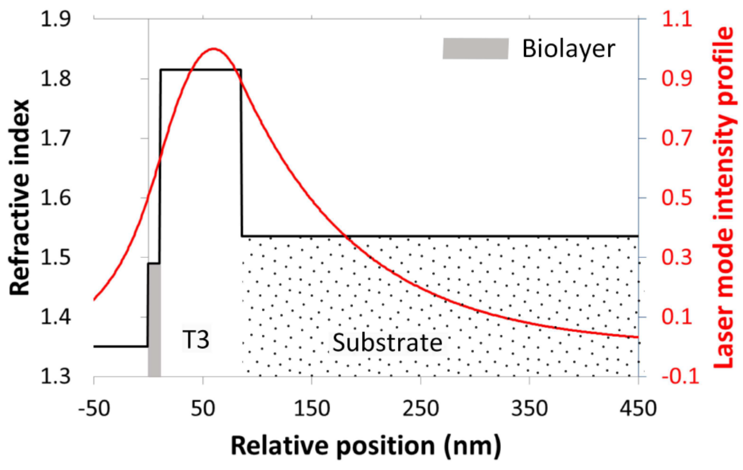

Figure 2.9– Refractive index of different layers of a Tr (T3) DFB laser with a 10mm biolayer, The evanescent field distribution through the structure is shown in red.

The resulting mode profile can be plotted against the refractive index of the structure and stack of layers, as shown in the example in Figure 2.9, where a Tr-DFB laser (n = 1.81) is represented with a 10 nm biolayer (n = 1.49) on the Tr surface. The laser mode field intensity is proportional to the square of the field amplitude and the contribution to the field for a particular layer can be determined. Eq. 2.15 is an example of the calculation of the laser mode intensity overlap (Γ_{bio}) with a biomolecule layer on the laser surface, that extends from x = 0 to x = 10 nm (for a 10-nm thick layer)

$$\boldsymbol{\Gamma_{bio}} = \frac{\int_0^{10} |\boldsymbol{E(x)}|^2 \boldsymbol{dx}}{\int_{-\infty}^{+\infty} |\boldsymbol{E(x)}|^2 \boldsymbol{dx}} \qquad \textbf{Eq. 2.15}$$

The shift in laser wavelength due to changes in bulk refractive index are modelled by varying the refractive index of the semi-infinite superstrate layer. For a Tr laser, the semi-infinite substrate layer had a refractive index of approximately 1.52 and a gain layer index of approximately 1.81 (1.64 for BBEHP-PPV) and a thickness approximated by averaging over the grating period to account for the effect of the periodic modulation of the gain layer thickness. When modelling the response of the laser to the adsorption of nanolayers at the OS-DFB laser surface, the index and thickness of the layers were set to average values.

2.5 CONCLUSIONS

Optical sensors dominate in the field of biosensing, simple fabrication techniques and highly tuneable designs make them attractive for research and the development of compact, high resolution POC diagnostics. While SPR and PhC are well established and currently being developed for specific application. In a much earlier stage are active resonator DFB lasers, studies have demonstrated the potential for their employ as evanescent sensors and modelling work presented in this chapter demonstrates some of the core concepts for OS-DFB laser sensor fabrication and potential.

In contrast to dye based implementations the OS thin film DFB lasers, described in this chapter, achieve greater sensitivity and low-energy solutions. Using a Mathcad model, the various materials and configurations of DFB laser were assessed in terms of the resulting DFB output and the distribution of the evanescent field. Comprised of a thin nanolayer of OS material deposited on an epoxy grating with a matched grating period to the OS photoluminescence they are responsive to changes in the refractive index in regions localised to the thin film. Higher evanescent field distribution over a sensing biolayer allows for greater sensitivity and higher distribution over the gain layer would lower the threshold energy required to produce laser action. The refractive index of the layers of the DFB laser were the key factor in determining the field distribution.

Surface adsorption techniques along with covalent attachments in the form of amine ligation and click chemistry can be used to immobilise probes at a surface. With the wealth of biomarkers which present themselves for CVD patterned lasers with multiple isolated pump spots could be used to form multiplexed devices giving a more comprehensive diagnosis. Compared to PhC and SPR based devices there is still development needing done to realise OS-DFB lasers as a biosensing platform and Chapter 3 will discuss the experimental work done to this end while comparing and contrasting some different candidates for the OS gain material.

Chapter 3

LASER SENSOR EXPERIMENTAL METHODS

3.1 INTRODUCTION

As discussed in previous chapters traditional biosensing strategies involve the labelling of the target biomolecule with (typically) an optically/electrochemically active, reporter. This reporter is the actual measurand being quantified by the output transducer. For obvious reasons a biosensor which can detect the presence of an unlabelled biomarker present in a patient sample is a more attractive solution; less processing required on the patient sample and less complexity in the bio-detection paradigm with potential cost reductions as well.

Label free optical biosensors [153] in their implementation typically operate due to the response of evanescent wave interactions with analyte molecules [94]. A balancing act occurs as the sensing of these devices is reliant on the strength of the interaction between the analyte and the evanescent wave as well as the resonant bandwidth of the output and optimising both can be difficult as they are so closely linked. Using an organic laser sensor this trade-off can be mitigated as devices such as OS-DFB Lasers [99] or Photonic Crystal active resonators [154] achieve narrow emission bandwidths through coherent laser action without sacrificing the field interaction with analytes.

OS-DFB lasers are an attractive option as their simple and inexpensive fabrication techniques allow for a high degree of tunability in the laser characteristics. Building on work described by Haughey [4], this thesis demonstrates OS-DFB lasers can be functionalized with surface biochemistry for oligonucleotide capture and detection. An assessment for such a device employed as an evanescent sensor is reported in this Chapter to illustrate the main experimental concepts. Furthermore, a report on and exploration of different OSs for DFB lasers at different emission wavelengths (the specifics of these are detailed in section 2.2.3), Tr and BBEHP-PPV demonstrating the most promise is presented. Tr is the same material as the first OS-DFB laser sensor reported. BBEH-PPV is a conjugated polymer, which has the advantage of having an optimum absorption at in the blue region of the spectrum and therefore lends itself to diode laser or even light emitting diode (LED) pumping.

Presented in this chapter are the experimental methods and results for the development of a label-free oligonucleotide biosensor with an OS-DFB laser at its core. Primarily, wavelength monitoring is investigated as the transduction method. Lasing threshold energy is also briefly mentioned but is investigated further in Chapter 4.

3.2 OPTICAL SET-UP

To assess the OS-DFB lasers for implementation as biosensor transducers they need to be pumped by a laser with sufficient energy to induce lasing from a DFB laser structure; the output is collected for analysis using a spectrometer. The work presented in this thesis used as a pump source a Nd:YAG frequency tripled 355nm 10Hz Q-switched Minilite desktop laser output which is linearly polarized. A series of optical equipment as shown in Figure 3.1 was used to control the pump energy and focus the pump beam onto DFB lasers like the one in Figure 3.2(a) fixed to the bottom of a well-plate as shown in Figure 3.2(b).

The functions of the optical elements were as follows. The first two were used to expand the elliptical pump beam to be of 2.5 mm diameter from a 1 mm diameter at the source. Immediately after this, the first flip mirror can be used to redirect the beam to an energy meter to take readings needed for determining the pump energy incident on the DFB laser, and by calculation the threshold fluence. A halfwaveplate enables the rotation of the linear polarisation of the pump beam before a polariser. This waveplate/polariser combination

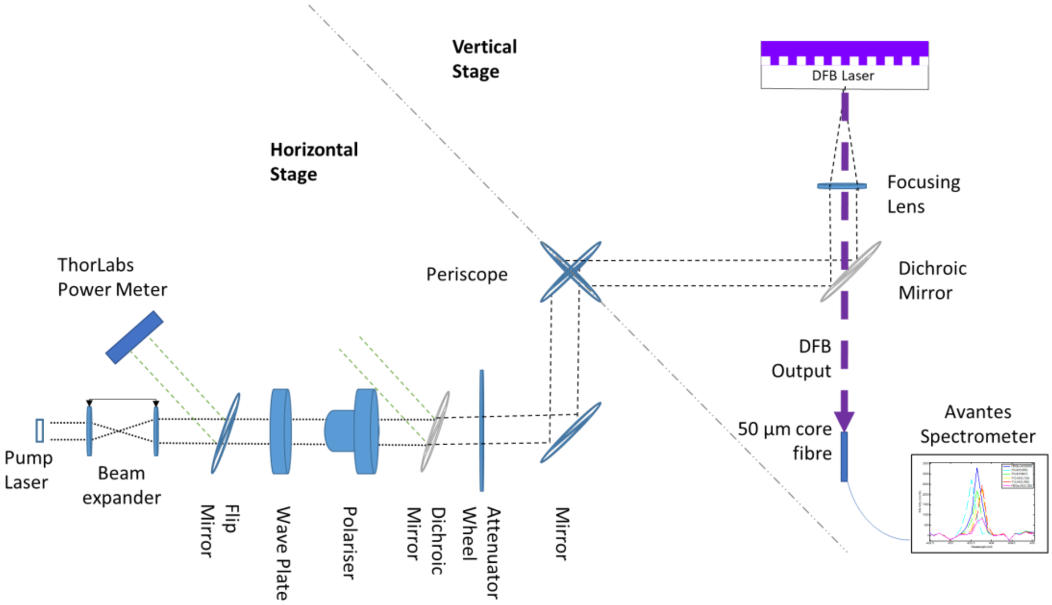

Figure 3.1 - Schematic of table top set-up for DFB laser pumping, A horizontal stage performs beam shaping, power regulation and a flip mirror can be used to redirect the source beam for power readings. After a periscope translates the beam vertically into a vertical stage which focuses the pump beam onto samples and filters it from the DFB laser output before ithe laser output is coupled into a 50µm core fibre to be analysed by a spectrometer.

enables the controlled attenuation of the pump beam energy. Following this, a dichroic mirror operates as a lowpass filter blocking any unwanted wavelengths of light; passing through only the 355 nm pump photons. An attenuator wheel is then used to further control the pump energy.

The pump beam is next redirected across the table with mirrors to the vertical stage where another dichroic mirror separates the pump laser beam from the DFB laser output. The pump beam is focused onto DFB laser samples and the DFB laser output is emitted down, passing through the dichroic mirror to be collected by the 50µm core fibre.

A well plate was fixed in a table-top stand (shown in Figure 3.2(c)) and the pump beam focused on DFB lasers; the reflected pump beam was then separated from the DFB laser output with a dichroic mirror. A free moving table top stand was used to hold well plates containing DFB laser samples. A mechanical stage could be used to hold the samples closer to focus but with a very limited range of horizontal movement making the free moving stand better for testing multiple samples. A change in the style of well plates from the supplier meant that modifications to the stands would be needed if the samples were to be pumped at the exact focus of the lens; the latter was translated fully upwards in the current set up.

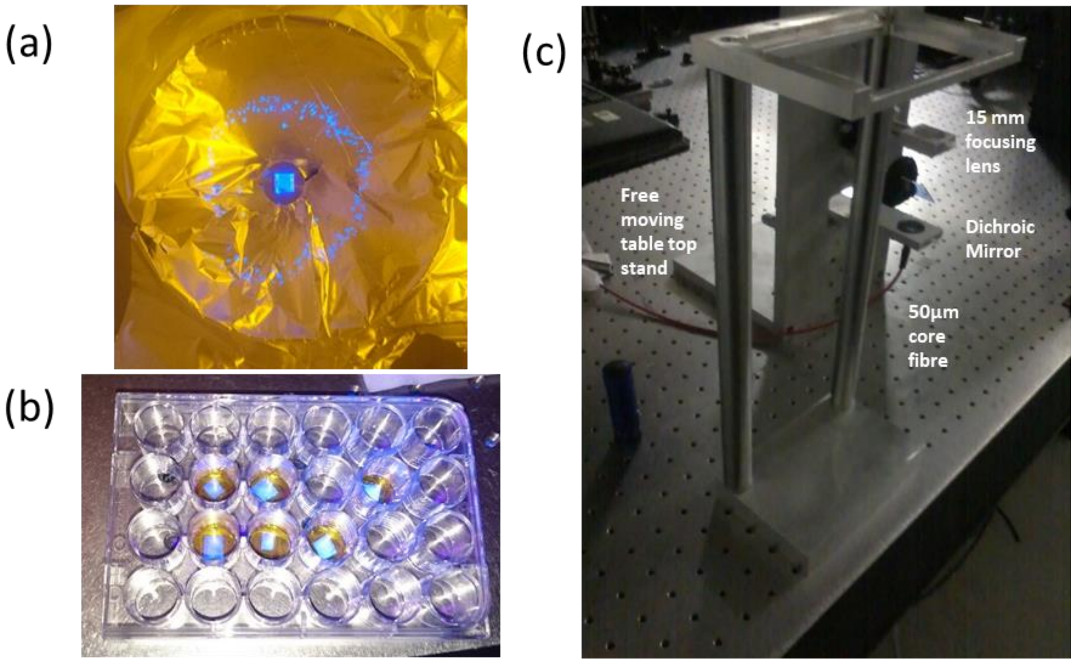

Figure 3.2 - (a) DFB laser in spincoater illuminated by UV (b) DFB lasers taped to the bottom of a microtitter wellplate (c) Free moving table-top stand, for securing wellplates, and the vertical stage with 50µm core fibre, dichroic mirror and 15 mm focusing lens

The DFB laser emission was coupled into a 50µm core fibre (these can be seen in Figure 3.2(c)). The fibre guided the collected DFB laser output to an Avantes grating-coupled CCD spectrometer with a 0.13nm resolution and using Avasoft software the raw spectral data was exported for processing.

3.2.1 *PUMP BEAM CHARACTERISATION*

Using a ThorLabs CCD Camera Beam Profiler, 350nm-1100nm detection range, and a ThorLabs PM100D energy meter, the characteristics of the pump laser source could be analysed for the calculation of the fluence. The fluence is calculated as the incident energy divided by the area of the pump spot ($E / \pi r_x r_y$, where $\pi r_x r_y$ is the area of an ellipse with r_x and r_y the radii along the x and y axes at the $1/e^2$ intensity cut-off of the Gaussian pump beam).

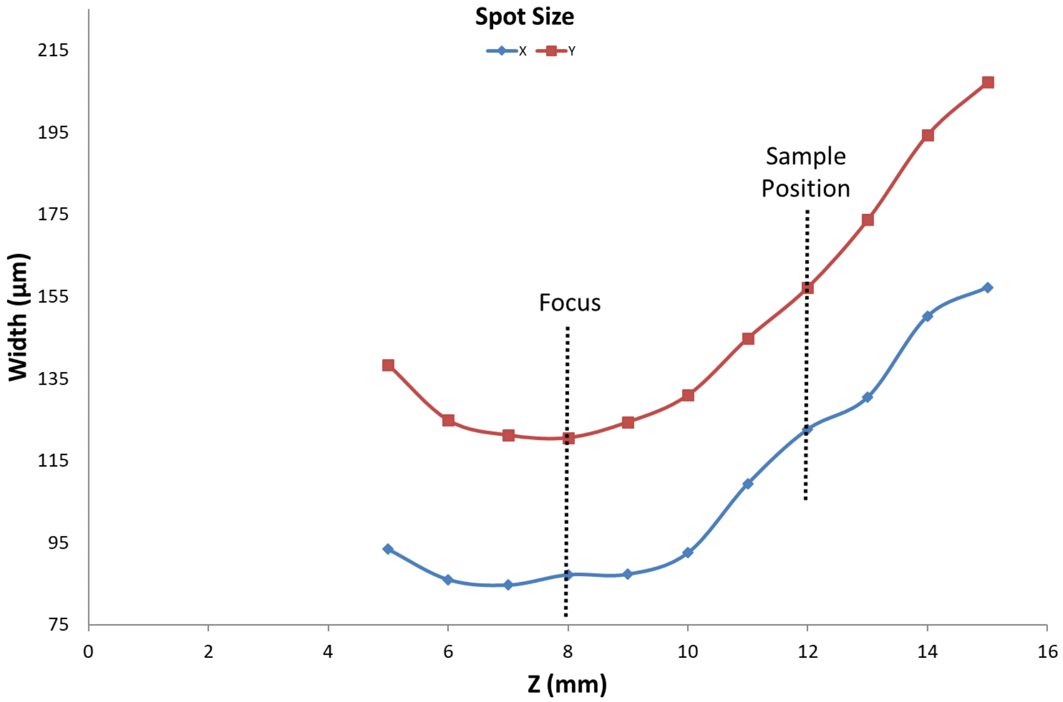

Figure 3.3 - x and y diameter measurements for pump beam width at a range of heights surrounding the focal point of the lens in the vertical stage at z = 8mm DFB samples in the well plate holder were found at z = 12 mm $1/e^2$ cut off used for width estimation.

To determine the pump energy incident on the DFB lasers, the pump energy output after the initial beam expander was first determined statistically with the ThorLabs power meter averaging the output over 1 min. Then using calibration data representing the attenuation and polarisation filters transfer function the energy incident at the DFB laser could be obtained. The pump spot size is also needed for the calculation of the pump fluence (energy intensity) incident on the DFB lasers. A ThorLabs beam analyser was used to measure the pump beam diameter, using micrometre stages to translate the beam analyser vertically through the focus of the pump beam and determine the averaged diameter of the beam striking the DFB lasers.

Gaussian optics describe the beam propagation of lasers and their transformation through optics [155]. When focused by a lens, the beam expands (diffracts) on each side of the focus point. The evolution of the beam (as characterized by its width along the X and Y axis at the $\mathbf{1/e^2}$ diameter) around the focus in the X and Y directions as measured by the Beam Profiler can be seen in Figure 3.3 it is observed to be elliptical and measurements show that the samples are being pumped 4 mm above the focal point of the vertical stage lens. Later in section 3.3 it is discussed how depth variations across the surface of DFB lasers increases the noise observed when analysing the spectrum of OS-DFB laser outputs. One way to mitigate this noise is to use a sharper/smaller spot when optically pumping the device; as over a smaller area it is easier to find a smoother surface region to pump resulting in a narrower linewidth and a more regular spectral shape for sensing applications.

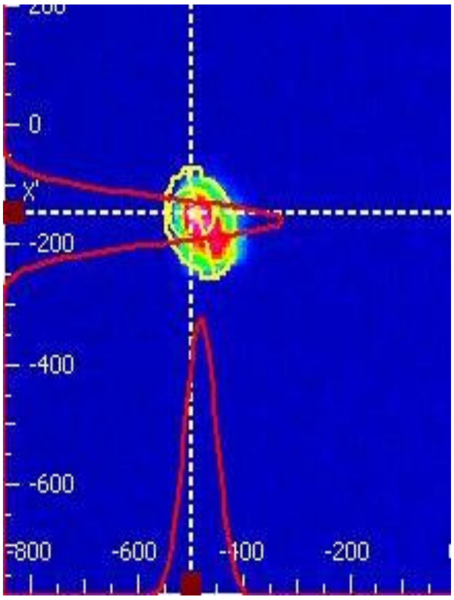

Figure 3.4 - Pump beam profile of Nd:YAG frequency tripled Q-switched 355nm laser imaged using a ThorLabs Beam Analyser. The vertical and horizontal cross-section are a fitted with Gaussian (red curves) from which the 1/e^2 intensity radii are obtained.

However, reducing the spot size too also increases the threshold. The pumping conditions used were sufficient for the work done as part of this investigation, however future investigations could require more accuracy and modification of the vertical stage for more precise alignment and shaping of the pump beam (for example a narrow stripe should in principle enable narrow linewidth without compromising threshold performance).

Figure 3.4 shows the pump spot's 2D beam profile incident on the DFB laser samples. The pump spot was found to have diameter in the x direction, $d_x = 120$ µm, and diameter in the y, $d_y = 160$ µm. Measured with an initial energy (before attenuation) of 34 ± 7% µJ. In previous work Tr lasers optimised for sensing were found to have a threshold pump fluence of 60 µJ.cm^{-2} but, discussed later in Section 3.3.1, DFB lasers measured in this set up had a typical threshold pump fluence in the 80-100 µJ.cm^{-2} range. While lasers in this work were optimised for sensitivity and not threshold fluence the elliptical pump spot could also mean inefficient energy coupling is responsible for the suboptimal threshold fluence found in this work.

3.2.2 DFB LASER FABRICATION

Distributed Feedback (DFB) Lasers are optically pumped grating structures imprinted into an optical gain medium satisfying the Bragg condition for laser oscillation (Chapter 2). The waveguide formed by the grating coupled with the optical gain produces laser action. They have been shown to be sensitive to changes in the refractive index in regions localised around the DFB laser as the evanescent field of the laser mode extends spatially to the surrounding spatial regions; the mode profile is dependent on the indices of the surrounding materials. In this manner vertically emitting DFB lasers can be employed as evanescent sensors as has been shown by Lu et al. [99]; Haughey et al. [89] and Retolaza et al. [15] for biosensor development.

Epoxy gratings were fabricated as shown in Figure 3.5(a), imprinting a Norland NOA65 epoxy (1) with a silica master grating (made by e-beam lithography) compressed by pressing down an acetate backing(2) and UV curing for 50 s under a UV lamp for a dosage of 300 J.cm^{-2} (3). Peeling off the acetate backed epoxy gratings (4) they would then be post cured for 1 h to stabilize the structure. Master Gratings were cleaned in a beaker of acetate in an ultrasonic bath for 2 mins to reduce build-up of epoxy.

To manufacture OS-DFB lasers an optically active gain medium formed of an OS is spin-coated onto the epoxy optical grating with a periodicity chosen so that the resonance matches the ASE peak wavelength of the OS material. The spin-coating speed can be modified to tune the thickness of the nanolayer of OS deposited on top of the grating. As previously discussed the response of the laser mode to the refractive index of the surrounding materials means this thickness is important in tuning the effective refractive index (n_{eff}) and in turn the number of supported modes, sensitivity and the output wavelength of the DFB laser. The specific fabrication procedures for preparing OS-DFB lasers on epoxy gratings with Tr and BBEHP-PPV are discussed in section 2.2.3. OS-DFB Lasers were each incorporated into the bottom of a well in a well plate as shown in Figure 3.5(b) to be optically excited using the set up discussed in section 3.2. This arrangement enabled easy immersion of the lasers for the different steps of surface functionalization, bio-hybridization and characterization, as detailed throughout the remainder of this text.

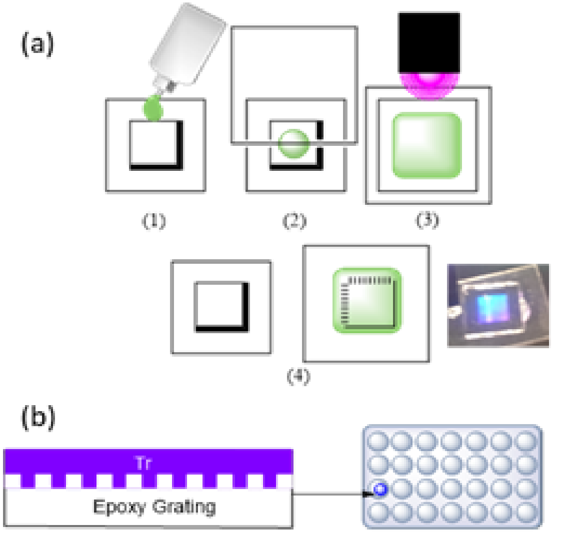

Figure 3.5 - (a)Epoxy grating fabrication steps with image of fabricated grating with light diffracting through it (b) Tr-DFB laser is taped into the bottom of a microtitter wellplate for optical pumping and immersion investigations.

3.3 DFB LASER SENSOR

Herein is discussed the investigation of the sensor applications of OS-DFB lasers as described in section 3.2. Illustrating the main concepts using two different OS materials for the gain region, respectively the Tr macromolecules and the conjugated polymer BBEHP-PPV. OS-DFB lasers in comparison to early dye based implementations of DFB lasers typically

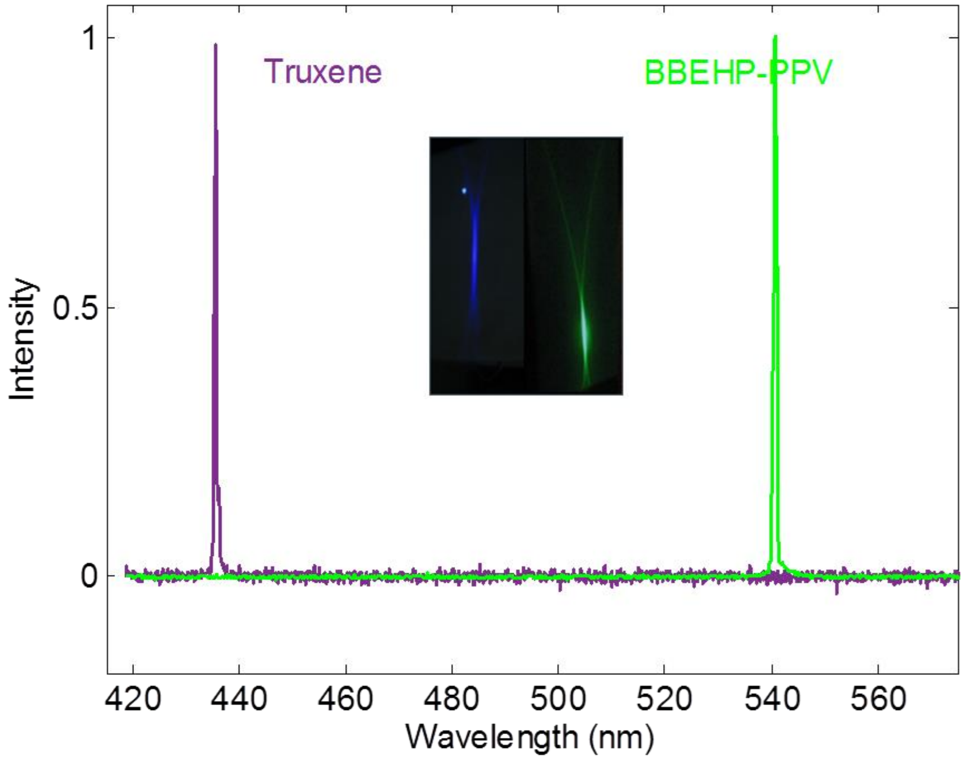

Figure 3.6 - Typical output Spectrum for Tr and BBEHP-PPV DFB lasers with inset showing typical OS-DFB laser fan shaped output

require lower energy optical pumping to produce laser oscillation, without encapsulation [92]. The Tr DFB laser technology has utilized crystal lasers (a desktop size Nd:YAG, Q-switched, frequency tripled, 355nm Minilite laser in this work) because of the absorption spectrum of Tr peaking in the UV. These can be made palm size but typically the overall system will have limited portability. For point-of-care diagnostic tools a portable and miniaturized device is much more suitable and smaller solid-state lasers could be used in their place. Since Foucher, Guilhabert, et al. [87] have shown success with a 450nm laser diode pumping Polyvinyl alcohol (PVA) encapsulated BBEHP-PPV DFB lasers have been investigated as alternatives to Tr DFB lasers which previous work focused on [89].

3.3.1 THRESHOLD, SPECTRUM AND OUTPUT BEAM

Figure 3.6 shows the typical output spectrum above threshold for both Tr and BBEHP-PPV DFB lasers operating at around 435 nm and 540 nm respectively. These are at the lower end of single moded vertically emitting 2nd order DFB lasers fabricated with their respective material and fabrication conditions (described in section 2.2.3). BBEHP-PPV DFB lasers would typically produce devices with a narrower linewidth than those of Tr. This could be explained by BBEHP-PPV forming smoother films. The inset of Figure 3.6 shows the typical output beam of these two lasers. The laser beam is a line because of the 1-dimensional DFB grating used in these lasers, resulting in feedback and photon confinement in only one direction. Less intense fan-shape lobes can also be seen and correspond to ASE diffracted out of the structure by the grating.

The 2 different OS materials required pumping at different pump fluences. The Avantes spectrometer data was processed in Matlab. Using functions described by Herrnsdorf [156] a Gaussian curve could be fitted to the spectral data (*peakdecomposition*) and used to estimate properties such as the central peak wavelength of operation of the device and the full width half maximum (FWHM) of the output. With this spectral data, integrating over the wavelength could be used to evaluate the relative output intensity as a function of the pump fluence, and in turn to determine the threshold. The results of doing as such are shown in Figure 3.7 plotted alongside a curve fitted to the data. The BBEHP-PPV-DFB lasers tended to have lower thresholds than Tr-DFB lasers as can be seen, although this would vary even at different pump spot positions on the same DFB laser.

Plotting this against the pump energy and fitting the data to Eq. 3.1, suggested by Boucher and Féron [132] to model a micro-resonator laser behaviour, it was possible to determine the lasing threshold (*softthresholding*). I_{sat} is the saturation intensity, F_P is the pump fluence, F_{Th} is the pump threshold for optical gain and κ accounts for the coupling of spontaneous emission into the laser mode [156]. Automating the spectrometer data analysis towards developing a diagnostic device, the functions described by J. Herrnsdorf were incorporated into some Matlab scripts described in Appendix I: MATLAB CODE.

$$I_{laser} = \frac{I_{sat}\kappa F_p/F_{Th}}{1 + I_{laser}/I_{sat} - F_P/F_{Th}} \qquad \textbf{Eq. 3.1}$$

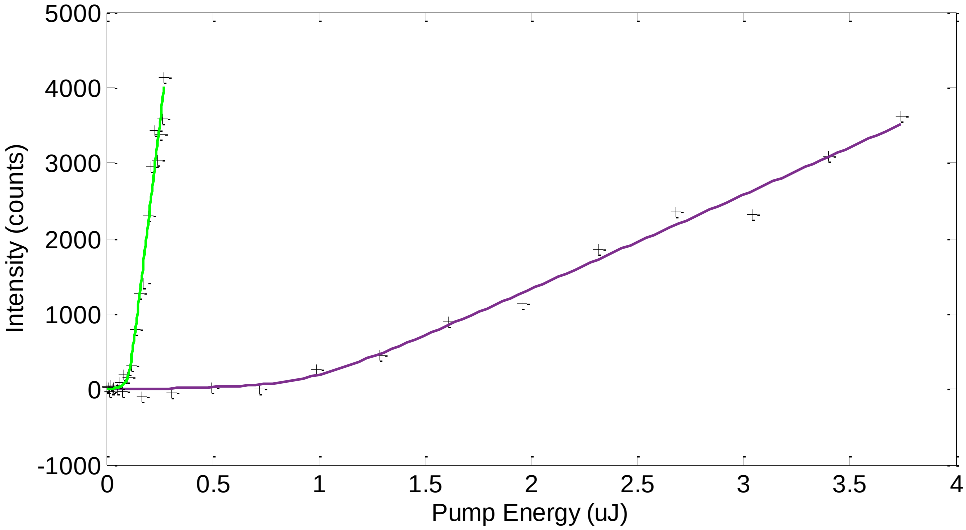

Figure 3.7 - Typical laser transfer functions (threshold curve data points shown as crosses) along with fits using Eq. 3.1 for a Tr-DFB laser (Purple) and a BBEHP-PPV-DFB laser (Green)

SY, also investigated, proved to be a much more difficult material to work with as the spincoating solutions were too viscous to reliably fabricate single moded SY 2nd order DFB lasers. McLellan [103] however reports on SY DFB lasers central emission wavelengths 570nm-590 nm, depending on the devices. Initial bulk sensing experiments however highlighted multimode and photostability issues which would need to be addressed before it could be utilized as an effective biosensing DFB laser platform.

3.3.2 IMMERSION EFFECTS ON WAVELENGTH AND THRESHOLD

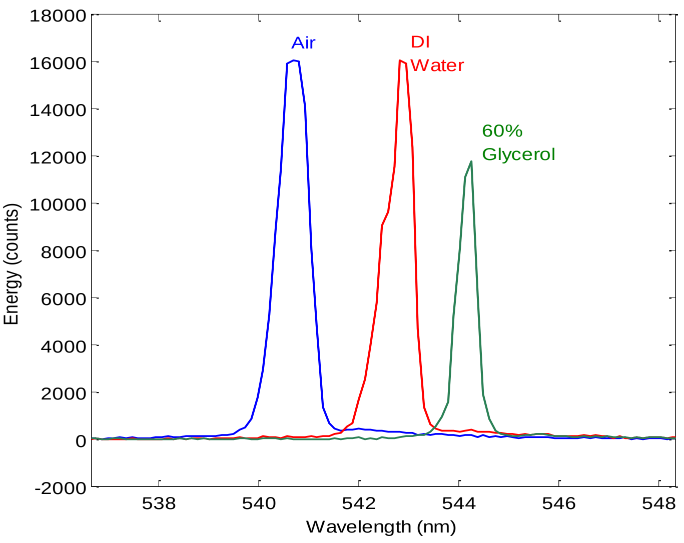

Figure 3.8 - Output Spectra from Avantes spectrometer of a BBEHP-PPV -DFB laser with different superstrates to demonstrate bulk refractive index sensing.

The choice of DFB laser gain material can affect the sensitivity since, as discussed, this property is dependent on the refractive index of all materials defining the laser cavity. In work determining the bulk sensitivity of these OS lasers, different concentrations of glucose were serially diluted from a 99% glucose solution and used to immerse DFB lasers while taking spectral readings. The resulting shift in wavelength (Δλ) from the immersion determined the bulk sensitivity measured in nanometres per refractive index unit (nm.RIU^{-1}). This is discussed in more detail in section 3.3.3. However, as an illustration, the spectrum of an OS-DFB laser output in air (n=1), water (n=1.33) and a glucose solution (n=1.42) is shown in Figure 3.8; the central emission wavelength (λ_e) red-shifts with immersion in a medium of higher refractive index. The transduction of bulk superstrate refractive index is understood through n_{eff}: the parameter related to Δλ by the Bragg equation calculated from the refractive index of the different layers in the structure, scaled by an overlap factor with the evanescent field of the laser mode

The model discussed in section 2.4 describes the multimode capabilities of OS-DFB lasers. As can be seen in there are minor variations in the spectral shape observed when the laser is immersed in different semi-infinite superstrates; this effect can be mitigated if a suitable pump spot is used and the linewidth is reduced below the spectrometer resolution. There are a number of factors which together result in this effect. First and foremost, the surface roughness of the OS nanofilm which forms the gain region of the DFB laser means that the OS layer thickness (shown in section 2.4 to effect the output wavelength) will vary across the pump spot. Surface roughness leads to a higher degree of variation in the output spectrum and in some cases the thickness can support multimode laser operation producing distinct shoulder (or even secondary) peaks in the spectrum.

One more factor which can contribute to variations in the spectral shape is that between immersion steps the fill/wash/drain cycle used (more detail in section 3.4.2) can initially remove small amounts of material from the OS nanofilm. Experiments into this effect have shown the variation due to the removal of loose material has a diminishing effect with each subsequent immersion since each time there is less loose material to begin with. These changes/variations in the surface morphology and by extension the optical properties of the DFB laser structure have an observable effect on the spectra of the OS-DFB lasers. On another note the fill/wash/drain cycle can cause minor changes to the alignment, precise perpendicular pumping of the samples can mitigate this as the angle of pumping affects the power coupling into the DFB laser and the fibre. Microscale movement of the samples during these processes are also a factor and ensuring your samples are as secure as possible is very important. As has been shown by the model (see section 2.4) and reported in encapsulation studies [90, 105, 157], introducing a layer of higher refractive index superstrate to the core DFB structure can shift the mode profile as well as affecting the overall n_{eff} value seen by the laser mode. Designed correctly this can result in more of the energy being concentrated in the active layer; modifying the mode profile facilitating a lower threshold energy. Surface variations like those discussed so far in section 3.3 can alter the observed spectral shape from the DFB laser output after immersion in a solution of higher refractive index as higher order modes are supported. Care needs to be taken during the analysis of the spectral data to account for these effects and correctly identify the effects on the mode seen in single mode operation.

Change in refractive index (e.g. by immersing the laser in a liquid) also affects the threshold. Because of this, and as is reported in a particular case in Chapter 4, the threshold could also in principle be used as a measurable variable for biodetection.

Table 3.1 shows the result of introducing water (n=1.33) superstrate to the DFB laser, in replacement for air (n=1), as can be seen the threshold is reduced as the laser mode is shifted higher in the cavity. More of the evanescent field is therefore focused in the OS gain layer, this means a lower pump energy can be used to achieve laser action. This effect can be seen in all 3 experiments; 2 & 3 were performed at different pump spots on the same sample. The variation in the energy values demonstrates the importance of keeping the pump spot alignment consistent throughout analysis.

Test	Air E_{th} / μJ	Water E_{th} / μJ	E_{th} reduction
1	0.43	0.36	16%
2	0.88	0.21	76%
3	0.30	0.16	47%

Table 3.1 - Threshold variance in OS-DFB samples with different superstrates Tests 2 & 3 performed on the same DFB sample

During initial experiments with AgNPs (confirming the surface chemistry was successful in lieu of confirmation by evanescent sensing as explained in Chapter 4) an obvious drop in the output intensity could be seen as AgNP bound target oligonucleotides were captured by probe oligonucleotides covalently linked to an adsorbed polyelectrolyte layer superstrate to the DFB laser surface. The surface chemistry used to achieve this and the effects of AgNPs on OS-DFB laser thresholds are detailed in section 4.3.3.

3.3.3 BULK REFRACTIVE INDEX SENSING

As discussed, OS-DFB lasers can be fabricated and implemented as sensors sensitive to changes in refractive index that could be measured in the wavelength of the laser output. The bulk sensing capabilities of BBEHP-PPV DFB lasers was assessed by exposing the laser to varying concentrations of glucose solution with calculable refractive indices

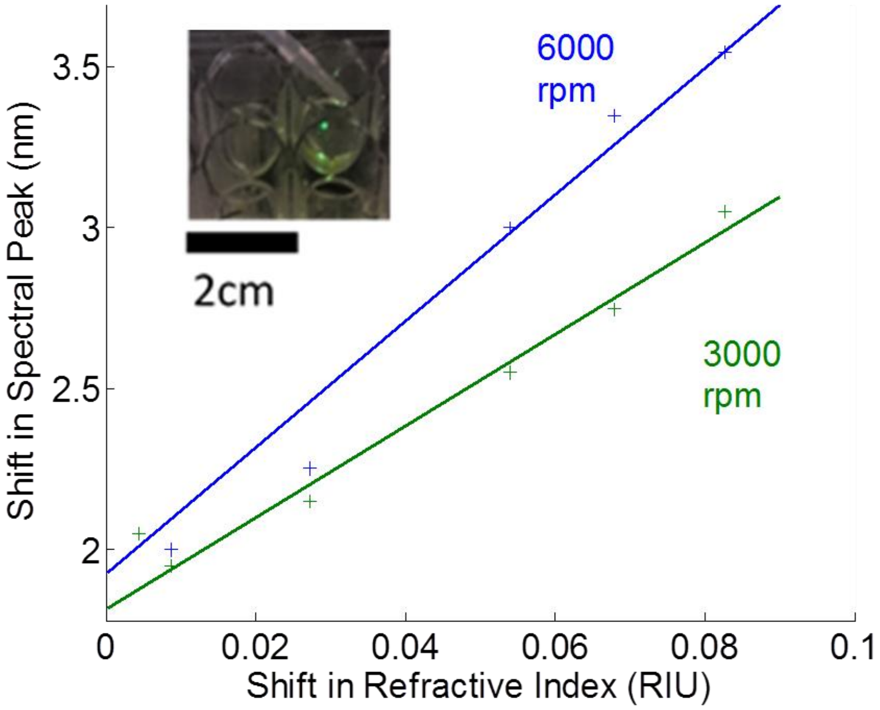

Figure 3.9 - Central emission wavelength shift (Δλ) of BBEHP-PPV DFB lasers in response to increasing the refractive index of superstrate solutions they are immersed in. Refractive index was controlled by increasing glucose solution concentration. Inset showing solution pipetting on immersed BBEHP-PPV DFB laser

Seen in Figure 3.9 are the plotted wavelength shift values, Δλ, for BBEHP-PPV DFB lasers spin-coated at 6 krpm and 3krpm against the refractive index for serially diluted glucose solutions from 0% DI water to 60% glucose solution. Refractive index values for different concentrations of glucose solution were obtained from a table in reference [158]. Assuming negligible adsorption of glucose molecules onto the surface of the DFB laser; a valid assumption since DFB lasers return to their base wavelength when solutions were removed; these values can be considered the bulk sensitivity for the devices with semi-infinite superstrates.

This sensitivity is, respectively for the lasers spin-coated at 3 krpm and 6 krpm, 11 nm.RIU^{-1} and 16 nm.RIU^{-1}. Compared to Tr DFB lasers this sensitivity is less than the 23nm.RIU^{-1} as reported by Haughey et al. [89] in a similar experiment. This gives a rough idea of how the DFB lasers will respond to refractive index changes caused by biomolecular adhesion to the surface of the DFB structure. 6 krpm demonstrated the limits that the equipment could reliably spin-coat onto epoxy gratings, it is possible that a greater sensitivity could be achieved with higher spinning speeds producing a thinner layer of OS since models predict a maximum of 21 nm.RIU for BBEHP-PPV lasers [89]. A comparison of experimental and modelled data for Tr and BBEHP-PPV DFB lasers can be seen in Figure 3.10. Expressed as a percentage of the central emission wavelength a maximum of 3.8% for BBEHP-PPV and 4.9% for Tr based DFB lasers. Over this range of refractive index perturbations, the wavelength shift appears to be approximately linear.

The effect on n_{eff} will be usually smaller with biomolecular interactions at the surface than the case of bulk sensing by immersion. The thin layers these interactions produce will affect a smaller proportion of the evanescent field's distribution than a semi-infinite section resulting from DFB lasers immersed in solution. Encapsulation has been shown to improve sensitivity by raising the evanescent field intensity at the surface region where biomolecular interactions occur. This is discussed further in Chapter 5 but has not been tested with DFB laser biosensors as the surface modifications would strip the encapsulating material while others are not biocompatible.

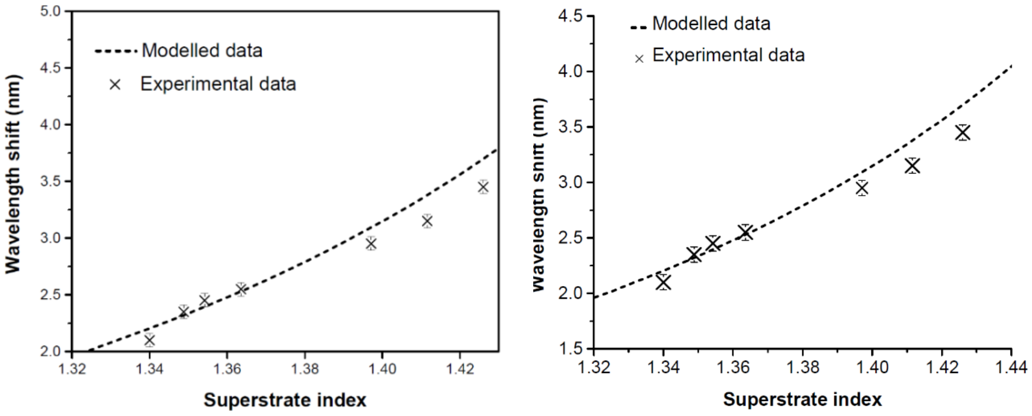

Figure 3.10 - Wavelength of operation of DFB lasers fabricated with Tr (left) and BBEHP-PPV (right) versus the superstrate index compared with modelled data

3.4 SURFACE SENSING

This section will bring together the concept discussed previously for wavelength-based DFB laser sensing with surface functionalization for oligonucleotide detection. Going from bulk sensitivity experiments towards a full biosensor necessitates the biochemistry functionalization of the laser surface, tailored for the detection of particular, specific analytes. Chapter 4 outlines in detail the biochemistry used to functionalise DFB lasers for oligonucleotide capture. In summary it involves an anchoring layer of PPL that is then modified with PEGylated azido N-Hydroxysuccinimide ester (Azido-PEG$_4$-NHS) as a linker allowing Alkyne tagged oligonucleotide probes to be attached onto the surface.

Using the Mathcad model the field distribution of a neat DFB laser and one with a PPL nanolayer are theoretically compared in Figure 3.11. It can be seen that the field is pulled towards the surface (towards negative d in the Figure) by the inclusion of a 5nm-thick nanolayer which has an estimated refractive index of 1.45, corresponding to a PPL monolayer [4]. The amine ligation site and the azide group are separated by 4 polyethylene glycol spacers; this is done since work by Haughey [4] suggested that steric hindrance could play a role in preventing oligonucleotide hybridisation at the PPL nanolayer surface.

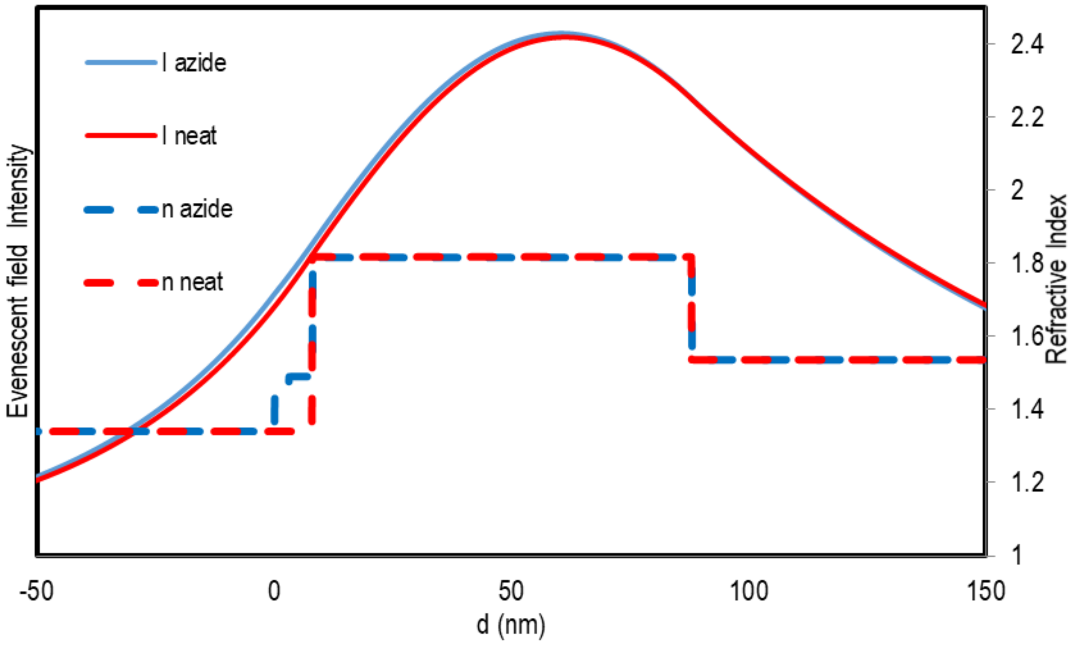

Figure 3.11 - Model output of TE_0 mode intensity and refractive index vertically through a Tr DFB laser where d is the depth from the OS layer surface

3.4.1 AZIDE MODIFICATION

Azide-modified laser surfaces were prepared by exposing the Poly(phenyl)-Lysine (PPL) monolayer-coated DFB laser surface to a 2mg.ml^{-1} solution of Azido-PEG4-NHS. This enables subsequent 'click' immobilization of alkyne labelled oligonucleotidess.

It was demonstrated that polyelectrolyte layers can be used to anchor probes to the surface of an OS-DFB [89]. In this manner a DFB laser surface is immersed with 200 µl droplets of PPL in 1mg.ml^{-1} 10mM phosphate buffer saline (PBS) for 10 mins. Washes with PBS were performed before and after immersion. Figure 3.12 shows the addition of a nanolayer of PPL which has terminal amine groups capped with Azido-PEG4-NHS, extending them, leaving terminal azide groups that can be used for click chemistry.

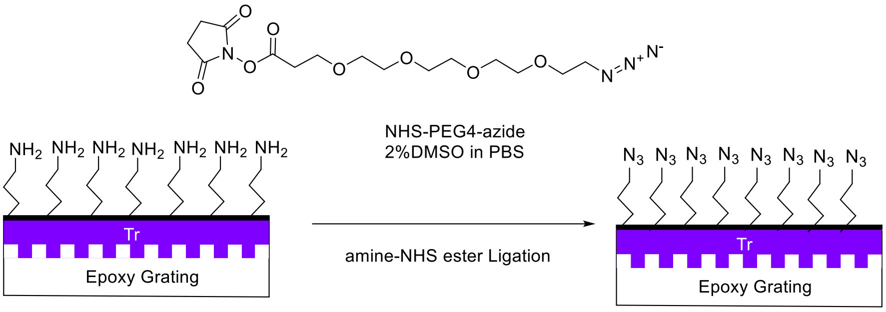

Figure 3.12 - Azide capping of terminal amines of PPL nanolayer on an Tr-DFB surface using Azido-PEG$_4$-NHS.

Again, the PEGylated azide group is separated from the ligation point by 4 Polyethylene-glycol (PEG) spacers as its been suggested that steric hindrance could be limiting the binding efficiency [4]. To perform the ester-amine ligation PPL coated DFB lasers were immersed with 200µl droplets of 2 mg.ml^{-1} Azido-PEG$_4$-NHS in 2% DMSO PBS. A PBS wash was performed after functionalisation to remove any loose material.

Recording the spectra before and after each step while immersed in PBS the λ_e of the DFB was shown to red-shift as material was adsorbed onto the surface. With the capping of terminal amines to present azide groups, again the red-shift in PBS immersed Tr-DFB laser's λ_e value was measurable by the spectrometer. The PEGylated azide arm is 2 nm in length.

Shown in Figure 3.13(a) are the spectra of PBS immersed DFB lasers before, during and after azide capping of the PPL layer. The λ_e values at 5 min intervals during immersion in 2 mg.ml^{-1} azido-PEG$_4$-NHS ester 2% DMSO PBS shown in Figure 3.13(b). There is a redshift observed up until 15 mins when the $\Delta\lambda$ resulting from azide capping began to saturate. This saturation in $\Delta\lambda$ is most likely due to terminal amines in the PPL monolayer becoming saturated with azide groups and the rate of amine-ester ligation slowing down. The λ_e values have a maximum error of 0.06 nm from the spectrometer resolution. The actual error will be less than this due to the fit applied by Matlab functions from

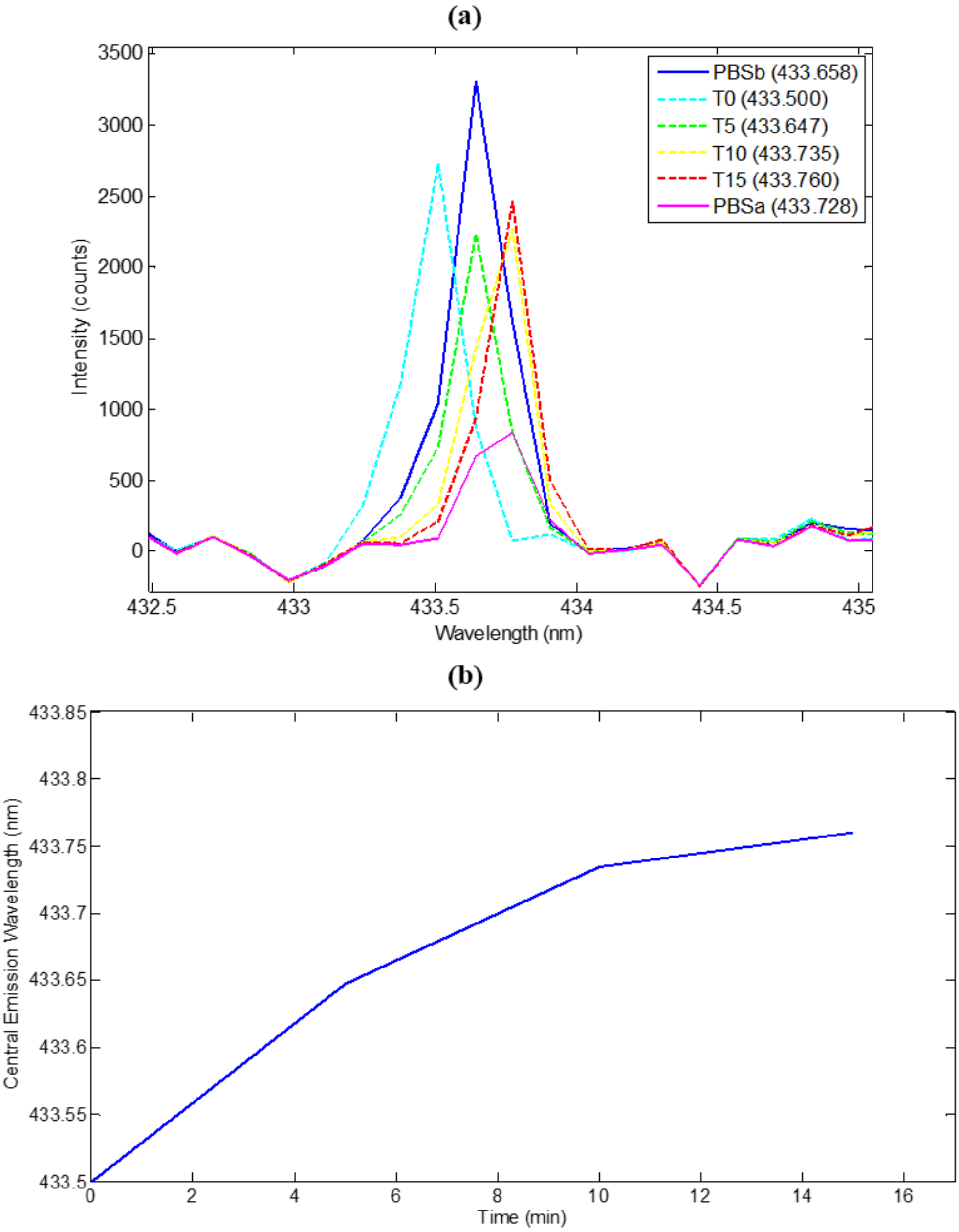

Figure 3.13 – (a) Red shifting wavelength of OS-DFB laser as terminal amines on PPL layer undergo ester ligation with azido-PEG$_4$-NHS. Showing PBSb/PBSa before/after (central emission wavelength calculated as described in section 3.3.1). (b) Central Emission wavelength of Tr-DFB laser from T=0minutes to T=15minutes.

The drop in intensity seen can be attributed to a number of factors. The reason for the low percentage of DMSO in solution is because this solvent can dissolve the Tr layer but is necessary for the amine-ester ligation. This along with the photostability of the DFB laser [156] dropping as a result of the optical pumping could account for the lower intensity observed after immersion. Limiting the exposure of the DFB laser to the pump beam while taking readings and taking an appropriate number of readings were essential parts of experimental design now that the basic principle had been confirmed. As a control, O-[(N-Succinimidyl)succinyl-aminoethyl]-O'-methylpolyethylene glycol (OME-PEG$_4$-NHS) ester was used to cap the terminal amino groups on the PPL layer and unlabelled target oligonucleotides were incubated in PBS on the surface of the laser for 30 mins. Comparing the results of the spectral shift from azido-PEG$_4$-NHS ester and OME-PEG$_4$-NHS ester there was no discernible increase in the $\Delta\lambda$ for the former. It was expected a red shift would be observed in the spectrum similar to that observed in the azide capping if the DNA was being captured by these surfaces. This result is consistent with theory as neither of these surfaces have been functionalised with probe oligonucleotides so there is no reason for the DNA to be binding to the surface and with no alkyne label they cannot undergo click chemistry to attach to the azide group. (see section 4.2).

Oligonucleotides used in this work (see section 4.2 for more detail) are 12-18 base pairs long and a single base pair measures 0.34nm so measure 4-6nm in length which is similar to the depth of PPL layer superstrate to the DFB laser surface. It could be assumed then that the oligonucleotide immobilisation would produce a measurable shift in the DFB laser output. However, since the PPL layer is a high density polymer layer; while in contrast the oligonucleotides can only be immobilised at terminal azide locations across the surface the effect on n_{eff} of oligonucleotide immobilisation is smaller. This sparse binding coupled with its spatial dislocation from the DFB laser surface minimises interaction with the evanescent field. The result is any red-shift expected from this interaction is unobservable and even the probe immobilisation could not be observed/confirmed by λ_e measurements.

3.4.2 PBS Washing

To prevent cross contamination between the various different functionalisation steps (more detail in sections 3.4.1 and 4.2) loose material (unattached OS or functionalisation materials) adsorbed onto the DFB laser surface was washed away using PBS. This was done by filling a well with PBS for a short time and then removing with a pipette. As has been discussed in section 3.3.2 the fill/wash/drain cycle used for this process is suspected to be able to cause changes to the surface morphology of the OS layers of a DFB. Some of the OS layer was assumed to be stripped from the surface of neat DFB lasers as the wavelength of PBS immersed lasers was seen to blue-shift; the PBS can also cause the thin film surface to swell and a reorganise its structure.

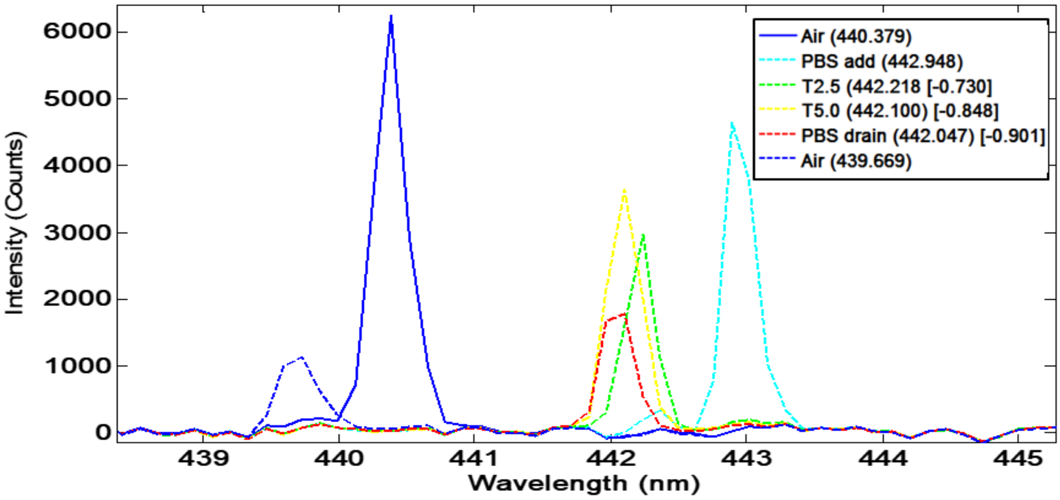

Figure 3.14 – Immersion of Tr-DFB laser with PBS showing spectral measurements at different points in a 5 min PBS wash. Dashed lines represent spectra after immersion.

Figure 3.14 demonstrates the resulting blue-shift by Tr stripping from PBS immersion during a 5 min wash. The effect can be seen to diminish over time and most of the blueshift occurs within the first 2.5 mins. The red spectrum was taken after the majority of PBS was drained from the well with a pipette, however, some droplets were still present on the surface localised to the pump spot. Once the surface had been fully dried, an overall blueshift of 0.71 nm is observed in the DFB laser output with air as the superstrate. This demonstrates the material stripping effects of a PBS wash step but since the amount of loose material present on any one sample can vary there was no discernible pattern in the blue-shift effects from one DFB laser to the next. The intensity drop is a result of alignment shifts surface morphology and device photo stability as previously discussed in this chapter.

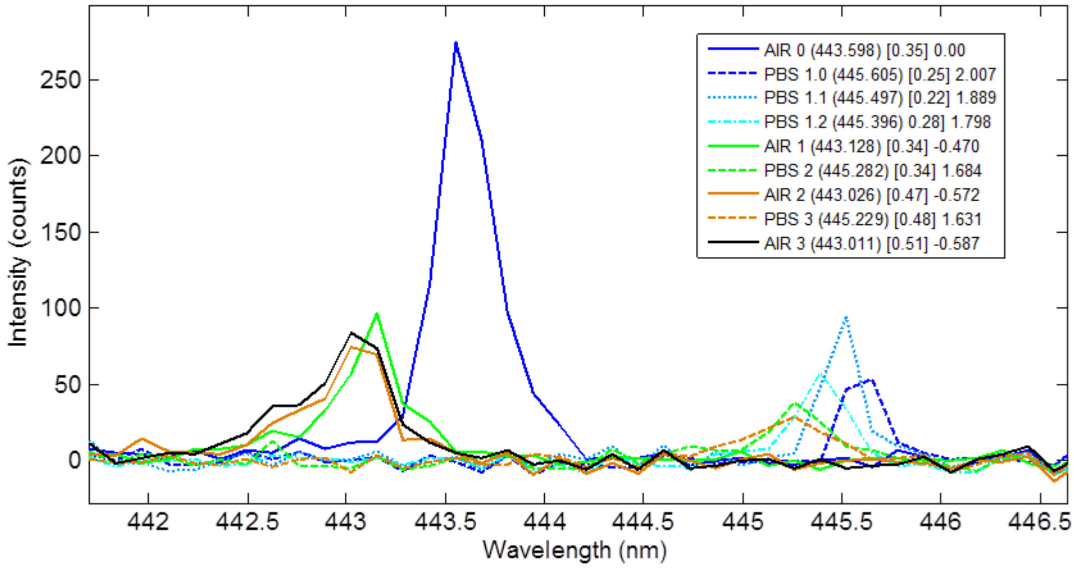

Figure 3.15 – Blueshifting spectra of DFB lasers during a sequence of PBS washes, a drop in intensity due to alignment and spectral effects of immersion demonstrates the effect of an increased FWHM resulting in a lower SNR.

Another experiment showed that most loose material was washed away in a similar fashion with 5 1 min wash steps, this can be seen in Figure 3.15. Laser surface functionalisation involves several iterations of the fill/wash/drain cycle with different solutions and washing with PBS between. This meant by the time spectral readings would be taken for biodetection the effect of loose material stripping would be minimized in the results. After 3 washes the blueshift in Δλ of a PBS immersed DFB laser, as a result of material stripping into the PBS, drops below 0.1 nm and the effects become negligible beyond this point (the spectrometer resolution is 0.13 nm).

Estimates in the values of λ in this experiment become inaccurate in later readings as the intensity drop and change to the spectral shape have increased the FWHM of the Gaussian peaks fitted. The low SNR results in errors due to the DFB laser's central emission peak intensity being close to the noise floor. Before taking readings with the Avasoft analysis package, they were baseline corrected with a background spectral reading; even with this correction the immersion effects on the spectrum lowered the intensity and resulted in a higher error with a Gaussian fit. This demonstrates another important consideration during DFB laser alignment ensuring that the intensity of the central emission peak is sufficient to mitigate the effects of the noise floor on spectral analysis. As well as with the pump spot size and position, this can be tuned by increasing or decreasing the pump energy with the use of an attenuator wheel.

3.5 CONCLUSION

This Chapter has described the practical concepts and steps entering in the development of a label-free oligonucleotide biosensor using an OS-DFB laser. It discussed bulk sensitivity, factors to be taken into account such as fabrication and washing steps, surface sensing, and compared two different OS materials for the application.

In conclusion, the optimum OS material for wavelength-based biodetection within the current set up is the Tr oligomer since it presents the greatest sensitivity. Surface functionalization with azide reacting groups was achieved and confirmed by wavelength transduction. Target oligonucleotides could not be detected using this technology in its current form but there are larger biomarkers which will specifically bind to oligonucleotides. Aptamers are a class of engineered oligonucleotides which can specifically bind to large proteins that could produce a measurable output from evanescent sensing. The following chapter will outline a method, using threshold instead of wavelength, by which it was confirmed that specific alkyne labelled oligonucleotide probes could be anchored onto the surface.

Encapsulation work by C. Foucher et.al [90]. has shown promise with BBEHP-PPV devices for low threshold operation with encapsulation which could allow the development of miniaturised devices using a laser diode pump over the desktop based Nd:Yag laser used in this work. As discussed previously by Vannahme et. Al [105]. cladding layers have also been used in dye based DFB lasers to improve sensitivity and this modification to BBEHP-PPV devices could potentially be used to fabricate an OS-DFB capable of being used as a portable, miniaturized form of this technology using laser diode pumping. In this manner the technology could be used to form the core component of a Point-of-Care device.

Selecting an appropriate pump spot before any experiment with optically pumped OS-DFB lasers is important in increasing the SNR and also finding a smooth surface spot with a near Gaussian spectral output can improve the resolution/reliability of the analysis functions used to characterise the output spectra. The set up used in this work was suitable for these initial assessment stages of the project but an automated mechanical stage capable of manoeuvring well plates with samples fixed to the bottom of wells at sub-micron scales would be much more suitable for larger scale data collection. However, it is also possible that a more integrated device format would mitigate the alignment issues and gain layer uniformity could improve with more scalable coating techniques.

Chapter 4

BIOSENSOR DEVELOPMENT

4.1 INTRODUCTION

As described in previous Chapters Tr-DFB lasers were fabricated by spincoating a nanofilm ≈80nm in thickness on the surface of an epoxy grating with 276nm periodicity. Employed as evanescent sensors they form the transducer element for a biosensor platform. The other component needed to achieve this is a selective and sensitive scheme for the capture of target biomarkers. This was mentioned in Chapter 3 when presenting the experiment to detect oligonucleotides by wavelength shift transduction and the challenges associated with it. Expand on here is the discussion of biomarker surface capture and sensing in this Chapter where click chemistry and monitoring of the laser threshold (instead of the wavelength) are respectively utilised for surface functionalization and bio-detection.

4.2 SURFACE CHEMISTRY

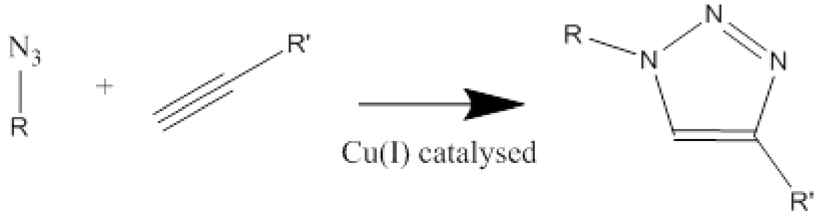

Figure 4.1 - Click chemistry reaction between azide and alkyne labelled reactants forming covalent linkages between R and R'

Previous work has shown that Tr-DFB lasers were responsive to the adsorption of self-limiting polyelectrolyte layers at the interface with the sensing medium [89]. To form a reliable and repeatable process for biosensor fabrication the use of covalent bonding to anchor probe structures at OS-DFB laser surfaces was investigated.

Click chemistry, a covalent linking protocol, has been used extensively for DNA modification and immobilisation studies [159, 160]. AM Haughey [4] explored a biocompatible copper free alternative to traditional click chemistry approaches but results were not conclusive. Using Cu-catalyzed alkyne-azide cycloaddition (CuAAC) click chemistry, depicted in Figure 4.1, oligonucleotides modified with a terminal alkyne group at the 5' can be immobilised onto an azide-presenting surface. If an OS-DFB laser surface could be modified in this manner probes could be immobilised to the surface, putting them within the overlap region of the laser mode evanescent field. As discussed in Chapter 2 this would employ the OS-DFB laser as an evanescent sensor for detecting changes in the refractive index due to biomolecular interaction with the probes. This would allow an OS-DFB laser surface modified with oligonucleotide probes targeted to a specific biomarker exposed to a patient sample to form the core of a biosensing diagnostic platform.

In order to functionalise the surface of an OS-DFB laser using covalent attachment strategies however, the surface must first be coated with an anchor by physical adsorption since none of the gain materials currently available have functional groups appropriate for covalent attachment [4].

4.2.1 CLICK CHEMISTRY

CuAAC is a robust covalent attachment strategy that has be used in the labelling [159] and immobilisation [160] of oligonucleotide sequences. Azide and Alkyne functional groups bind to form stable covalent linkages in the presence of Cu(I), this was discussed in section 2.3.2.2 and a schematic is shown in Figure 4.2. By using the more reliable copper catalysed protocol or even a copper free micro contact printing approach demonstrated by Rozkiewicz et al. [145] it is expected that a successful binding can be achieved on a DFB laser surface.

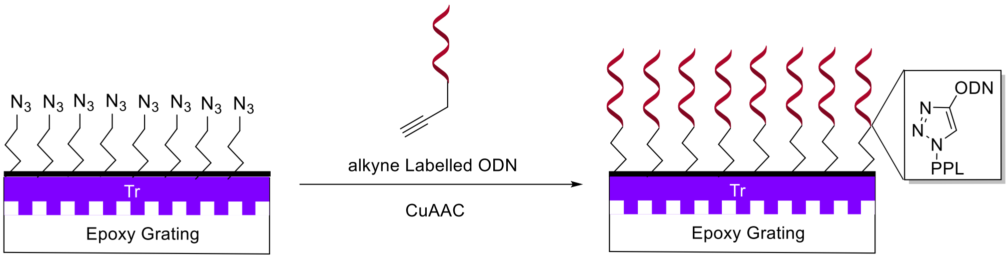

Figure 4.2 – Click chemistry immobilisation of alkyne labelled oligonucleotide probes onto an azide presenting nanolayer on a Tr-DFB laser

For CuAAC immobilisation of oligonucleotides, probe oligodeoxyribonucleic acid sequences were purchased from BaseClick with the (p) modifier shown in Figure 4.3. To immobilize these probes on the lasers, 17.5 nmol of a (p) modified oligonucleotides in deionized water with copper (II) sulphate, 35 nmol sodium ascorbate and 35 nmol Tris(3-hydroxypropyltriazolylmethyl)amine, was incubated for 30 mins. The surface is then washed with PBS.

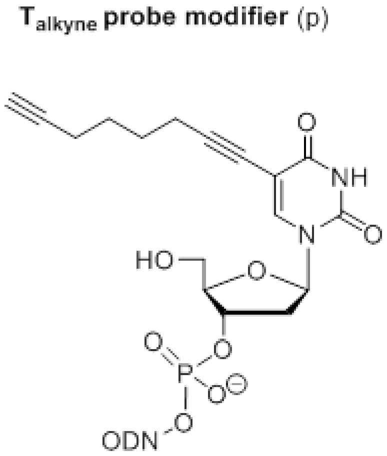

Figure 4.3 - Structure of probe oligonucleotide alkyne presenting label

In an investigation presented in section 3.4.2 the immersion in and removal of solutions at the surface of an OS-DFB laser left the dry device with a blue-shifted output. This is thought to be due the stripping of material from the surface and swelling of the gain layer minutely lowering the n_{eff} value of the laser mode. Repeated washes proved to cause successively less and less blue-shift so by performing washes between stages of surface modification this blue-shifting can be minimised to negligible levels in experimental readings.

4.2.2 BIO-HYBRIDIZATION

Oligonucleotide probess (ODNxp where x=1, 2 or 3 corresponds to different sequences as identified in Figure 4.4 and p is for probe) were purchased with an alkyne group at the 5’ end to enable click immobilization on to an azide presenting surface. These would form probes at the laser surface, which targets could bind to. Modified oligonucleotides were purchased from ATDBio and BaseClick,

	ODN sequences (5'→ 3')
ODN_{1p}	(p)—T-T-T—T-T-T—T-T-T—T-T-T—3'
ODN_{2p}	(p)—G-T-T-C-T-T-G-T-A-A-T-T-G-G-A-A-T-G—3'
ODN_{3p}	(p)—G-T-T-C-T-T-G-A-T-A-T-T-G-G-A-A-T-G—3'
ODN_{1t}	(t)—A-A-A—A-A-A—A-A-A—A-A-A—3'
ODN_{2t}	(t)—C-A-T-T-C-C-A-A-T-T-A-C-A-A-G-A-A-C—3'

Figure 4.4 - Oligonucleotide sequences for probe and target strands

For oligonucleotide targets (ODN_{yt} where y=1 or 2 corresponds to two different sequences, see Figure 4.4 and t is for target) were purchased with a terminal thiol at the 5’ end (shown in Figure 4.5). These were used to functionalize AgNPs [67] (synthesised as discussed in Section 4.3.1 to approx. 40-45 nm in diameter) labelled with malachite green isothiocyanate (MGITC) dye that was used for SERS detection.

As discussed in Chapter 3 the laser wavelength transducing approach proved to not be sensitive enough to detect the binding events of pM amounts of small molecule oligonucleotides. With the plasmonic enhancements of SERS nanoparticles amplifying the signal however the DNA hybridisation and the surface functionalisation strategies could be verified as follows.

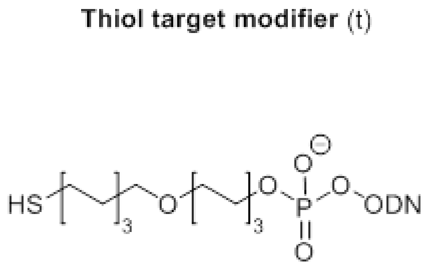

Figure 4.5 - Thiol modification on target oligonucleotide sequences used to functionalise AgNP surfaces

4.3 SURFACE ENHANCED RAMAN SPECTROSCOPY

By adsorbing dyes with unique Raman signatures onto metal nanoparticles their Raman signal can be amplified by a factor of 10^6 by the excitation of surface plasmons [138]. Using Surface Enhanced Raman Spectroscopy (SERS) detection methods Driskell et al. [139] has demonstrated the detection of microRNAs in picoMolar samples and the technology has been employed in the identification and targeting of cancerous biomarkers [161-163].

In SERS, light from a laser is confined by Surface Plasmons at a metal/air interface where the material being investigated has been immobilised, in this manner the scattering of the photons, as a result of the laser lights interaction with the target material, is amplified and detected by a Raman spectrometer.

4.3.1 NANOPARTICLE DETECTION

S. Mabbott, WestCHEM, Department of Pure and Applied Chemistry, University of Strathclyde, used the (t) modified target oligonucleotides (see Section 4.2.2) to modify the surface of MGITC coated AgNPs they synthesised. In this way AgNP labelled oligonucleotide target hybridisation could be observed with SERS mapping of OS-DFB laser surfaces. SERS involves the use of metal nanoparticles to amplify the Raman signature. AgNPs used in this work were synthesised using reducing sugars in the presence of Tollen's reagent as described by Kashmery et al. [67] resulting in a diameter of 40-45 nm.

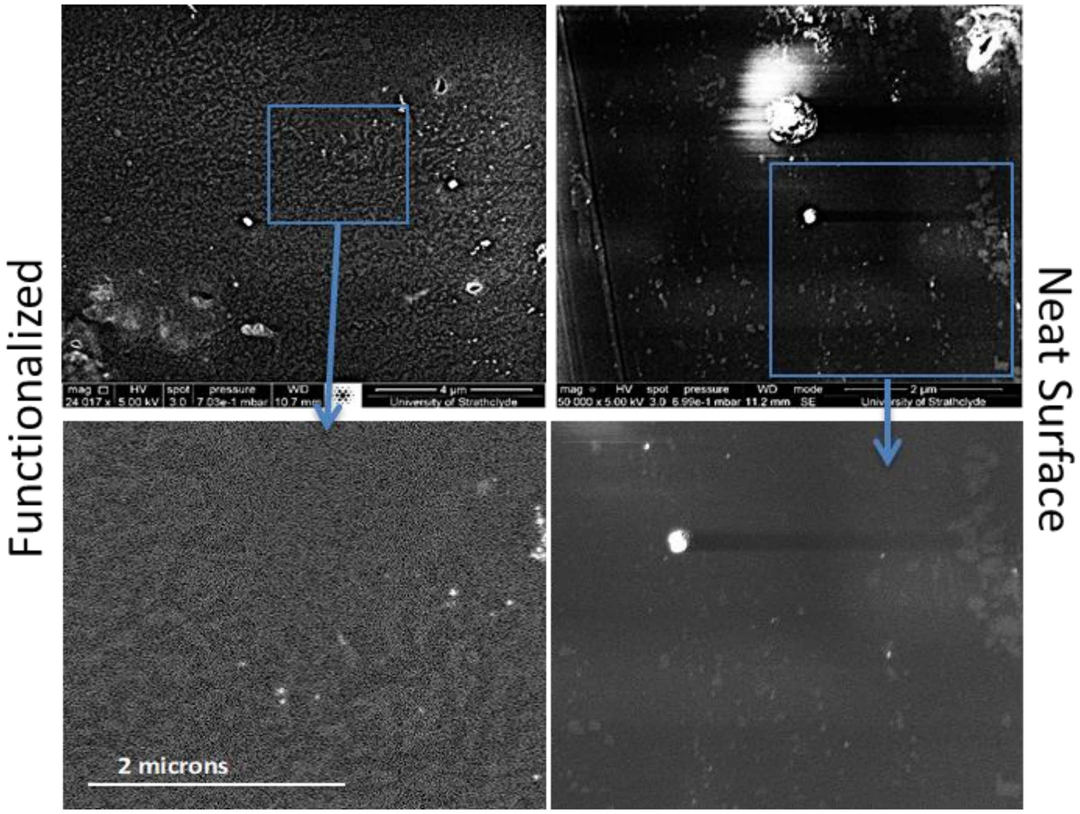

Figure 4.6 - SEM imaging of a functionalized and an unfunctionalized, neat, OS-DFB laser surface after immersion in AgNP bound target oligonucleotide 0.3M NaCl PBS showing a spotted pattern in the functionalised sample

4.3.1.1 SEM Imaging

Figure 4.6 shows the scanning electron microscope (SEM) image (taken by José Carreira, Institute of Photonics, University of Strathclyde) of the surface of an OS-DFB laser with and without probe functionalization after exposure to target bound AgNPs in solution. A dense spotted pattern across the functionalized OS-DFB laser surface that is not present on non-functionalized OS-DFB laser surfaces is attributed to the 40-45 nm AgNPs hybridized onto surface bound probes. A coverage density of 30 μm^{-2} was determined by counting spots within certain area. These images were captured using a Quanta FEG 250 from FEI, MV = 5kV and WD=10.7 mm / 11.2 mm

4.3.1.2 NP functionalisation

MGITC has a reported signature peak around 1171cm^{-1} which is circled in Figure 4.7 showing preliminary Raman Spectroscopy readings of AgNP labelled target oligonucleotides hybridised to oligonucleotide probes anchored on the surface of an OS-DFB laser. Similar to the target oligonucleotide strands, the MGITC dye molecules were bound onto the surface of the AgNPs by thiol ligation. Peaks identified in the blue spectrum can be attributed to the MGITC dye [67], the peaks that are also found in the red spectrum result from Raman scattering by the neat Tr-DFB laser.

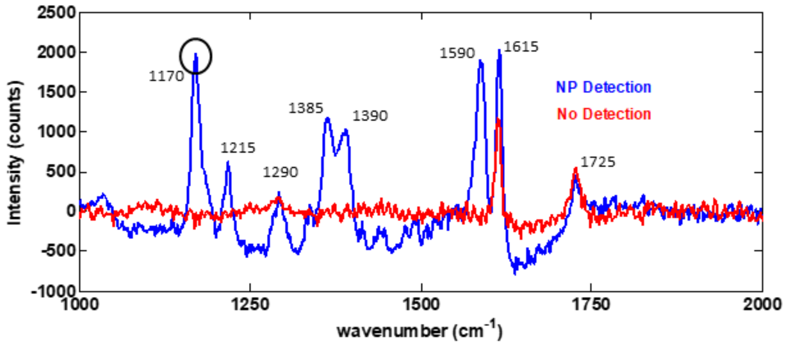

Figure 4.7 - SERS spectral comparison of a positive and negative result for NP detection on the surface of an OS-DFB laser, with the 1170 cm^{-1} signature peak of MGITC circled

4.3.2 SERS Binding Assessment

To obtain a mapping of SERS intensity, spectra like the one in Figure 4.8 were taken at intervals over the surface of OS-DFB lasers using a Raman microscope (Gloucestershire, UK) equipped with an excitation wavelength of 514.5 nm. Excitation light was focused on the samples using a 20x objective and the Raman shift was calibrated using a Si standard peak fixed at 520.5 cm^{-1}. Spectra of each sample were collected for 0.5 s in a 680-6080 cm^{-1} spectral range. The SERS peak present at 1171 cm^{-1} corresponding to the in-plane C-H bending of MGITC was used to track the AgNP distribution across the surface [67]. The SERS data was baseline corrected and the intensity of the signature of MGITC, indicative of the presence of AgNPs, used to generate surface maps with 0.01µm spatial resolution.

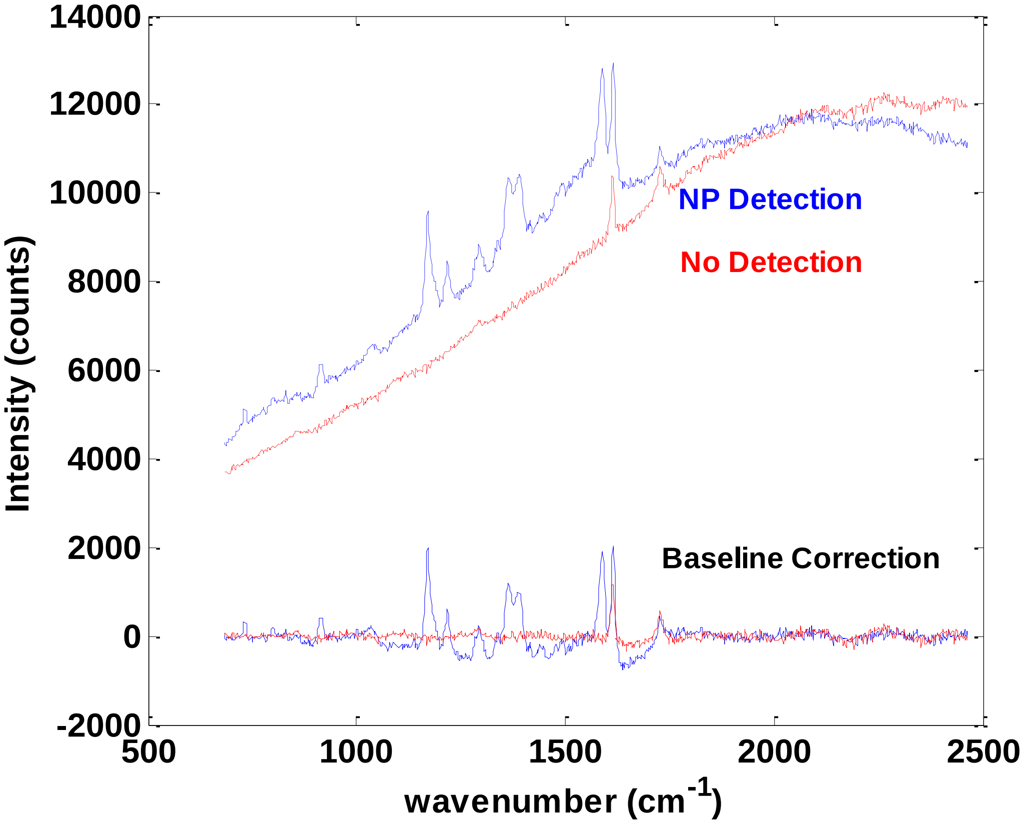

Figure 4.8 - Positive and Negative result SERS spectra from Tr-DFB lasers exposed to MGITC coated AgNP before and after baseline correction

With output from the Raman microscope using the Avantes Avasoft package, data was read into Matlab using SPCStruct data types to store the information. The different spectra were baseline corrected as shown in Appendix I.2.1 to remove background noise and produce spectra as seen in Figure 4.8. The baseline corrected intensity value of the 1171cm^{-1} MGITC signature peak was then taken for each pixel on a surface mapping scan and used to generate heat maps of the OS-DFB laser surface for different samples. Using this technique, the immobilisation of probes and hybridisation of target complementary strands labelled with AgNPs could be confirmed.

4.3.2.1 Experimental Results

The results in Figure 4.9 demonstrate the necessity for the various steps of the functionalisation process, as well as demonstrating by SERS surface mapping the specificity of the oligonucleotide hybridisation protocol. Modified OS-DFB laser surfaces were exposed to solutions containing AgNPs coated with the oligonucleotides poly-A_{12} (ODN_{1t}) in the top row and an unmatched control (ODN_{2t}) on the bottom row for 30 mins. With reference to the surface chemistry described in section 3.2.1 and section 4.2.1, different steps were modified in the following ways to demonstrate:

- in column 1: the improvements in surface binding as a result of the PPL layer used to anchor azides for click chemistry.
    - These samples had no PPL layer for the Azido-PEG_4-NHS to be covalently anchored to.
- in column 2: the specificity of the hybridisation of matched sequence target coated AgNPs to the fully functionalised OS-DFB laser surface.
    - These samples were fully functionalised with the poly-T_{12} ODN_{1T} probe oligonucleotides covalently anchored onto an azide modified PPL layer, adsorbed onto the Tr DFB surface, via CuAAC
- in column 3: that NHS-ester ligation was covalently capping the PPL layers.
    - Bizazido PEG was used in place of the Azido-PEG_4-NHS so no amine-NHS ester ligation could occur and the PPL layer would not present covalently attached azides for click chemistry
- in column 4: that click chemistry was anchoring the probes to the surface.

- The Azido-PEG$_4$-NHS step was omitted so there was no azide for click chemistry

These are compared to a neat DFB laser surface with no functionalisation steps prior to the exposure to target bound AgNPs.

There is very little coating observed on most of the samples in Figure 4.9 other than for the PPL treated sample immersed in matching poly-A$_{12}$ coated AgNPs. The samples in columns 1-4 used ODN$_{1P}$ (poly-T$_{12}$ matched probes) in the surface functionalisation protocol. The bisazido PEG sample's functionalisation used a PEG chain with terminal azides at either end in place of Azido-PEG$_4$-NHS to demonstrate the covalent capping of terminal amines of the PPL and not just surface adsorption was necessary for presenting azide click reaction sites. No azide samples were also prepared with uncapped terminal amines on the PPL layer to show that it was indeed CuAAC attaching the azido click reaction sites to the anchoring PPL nanolayer. The leftmost column was prepared with no PPL layer but some AgNP presence is observed.

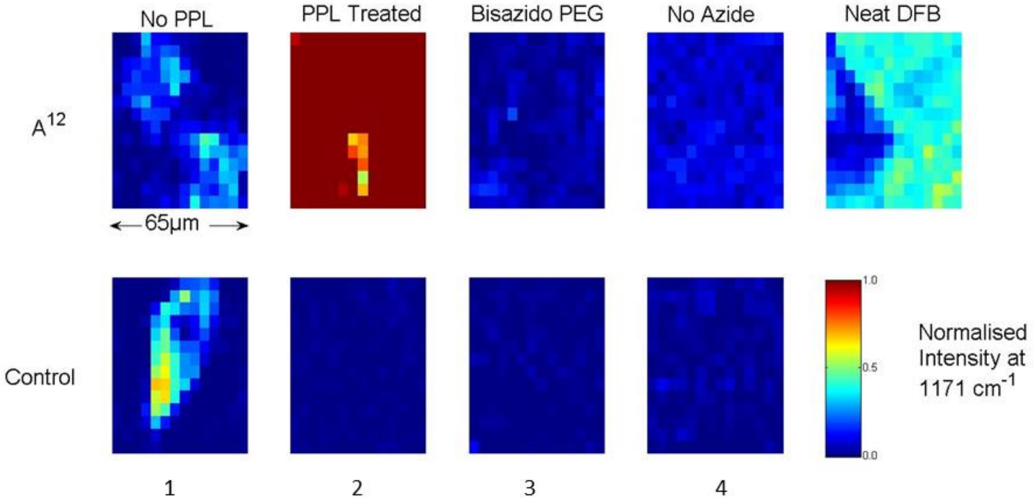

Figure 4.9 - Raman heatmaps of OS-DFB laser surfaces exposed to poly-A$_{12}$ (ODN$_{1t}$) and an unmatched control (ODN$_{2t}$) for 30 mins. The samples had undergone variations on the functionalisations procedures described in the text to verify the strategy

The results demonstrate that the binding affinity on the OS-DFB laser sample with the PPL anchored matching probe sequence for target bound AgNPs is far greater than other samples. The PPL layer appears, in samples where the oligonucleotide probes have not been successfully anchored onto the surface, to block non-specific absorption (NSA). The heat maps for these samples show less AgNP presence than the neat OS-DFB or samples excluding PPL from the functionalisation protocol. With no PPL to anchor to the DNA backbones seem to undergo some NSA similar to how the PPL itself would be deposited. This results in the low levels of AgNPs observed in these control samples.

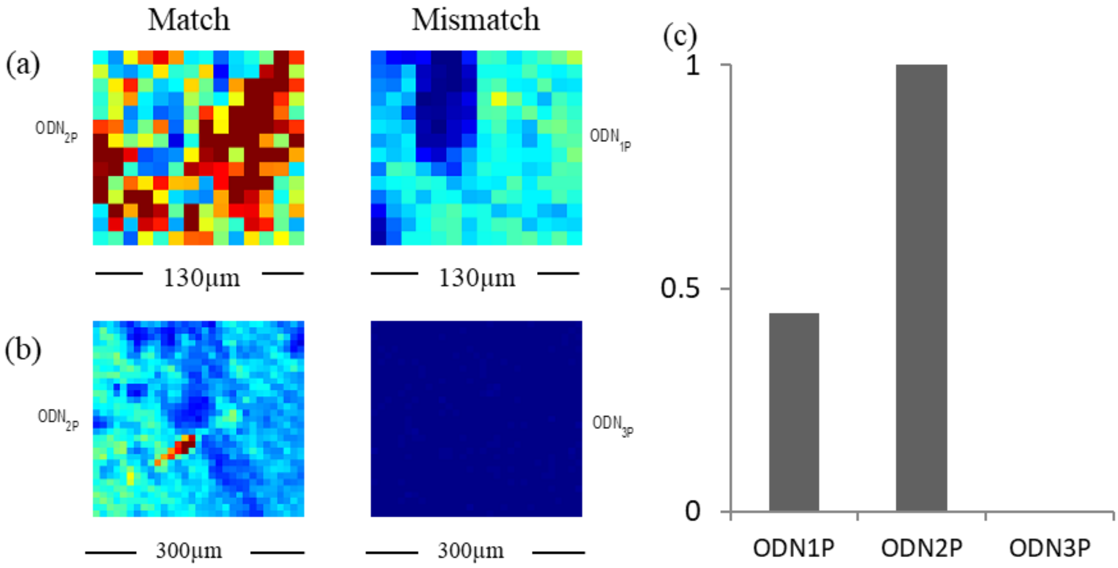

Figure 4.10 – (a)&(b)SERS heatmaps of OS-DFB laser surfaces functionalised with matched and mismatched oligonucleotide probes after immersion in MGITC & ODN_{2t} functionalised AgNPs suspended in 0.3M NaCl PBS (c)Normalised intensity of average pixel heat for each oligonucleotide probe.

Seen in Figure 4.10(a) & (b) are the surface maps for OS-DFB lasers functionalised with different oligonucleotide probes described in 4.2.2. These samples were immersed in solutions containing AgNPs functionalised with MGITC and ODN_{2T} oligonucleotides in 0.3 M NaCl PBS for 30 mins. In (a) ODN_{1P} probes had 61% of mismatch with ODN_{2T} and this was 11%

for ODN_{3P} in (b).Seen in Figure 4.10(c) are the normalised average intensity of the pixels shown in the heat maps. In each experiment (a) and (b) the pixel heat values were determined by normalising the intensity values to the ODN_{2P} maximum pixel intensity and scaling them to a 256 colour scale from blue to red (see Appendix I: MATLAB CODE)

In Figure 4.10(b) the size of the heatmap has been increased to 300 µm making the scans take longer but allows a more complete picture of the AgNP coverage to be formed. In the smaller scans, local maxima are observed as the maximum intensity and a smaller range of intensity values are represented, as a trade-off this does allow greater resolution to be shown as the same 256 colour scale is used.

Looking again at Figure 4.10(c) the drop in binding affinity of ODN_{2T} mixed base sequence target oligonucleotide bound AgNPs to mismatched ODN_{1P}/ODN_{3P} probe oligonucleotides when compared to matched ODN_{2P} probe coated OS-DFB lasers can clearly be observed. The ODN_{1P} samples are shown to have higher binding affinity than the ODN_{3P} samples and this is thought to be due to the ODN_{1P} probes being monobasic oligonucleotides containing only Thymine so it is easier for some partial binding to take place as some Adenine bases can partially bind to the Thymine chain. In ODN_{3P} samples the probes are polybasic oligonucleotides with bases 8 and 9 reversed from the ODN_{2T} matched ODN_{2P} probe oligonucleotides so random binding is far less likely than with ODN_{1P}. The lower resolution pixel colour scale on the larger maps will also contribute to lowering average pixel heat observed in these maps.

4.3.3 EFFECT ON LASING THRESHOLD

Confirmed by SERS using AgNP labelling, oligonucleotide targets had successfully hybridised to their probe counterparts and were shown to have a high and discernible specificity. With this in mind the next stage was to assess the OS-DFB laser capabilities as a biosensor for targets labelled as such. When AgNPs are adsorbed onto the surface, they absorb energy from the laser mode and otherwise introduce scattering effects, i.e. loss. This is because the laser mode is able to couple to the surface plasmons of the AgNPs.

This can be understood by looking at Figure 4.11, which represents the extinction spectrum of AgNPs and the typical emission wavelength of a Tr-DFB laser. The extinction spectrum of AgNPs overlaps significantly with the wavelength of Tr-DFB lasers used in this work. Because of this coupling to a lossy channel, a higher threshold energy/pump fluence is therefore required for laser action (i.e. a higher threshold) once AgNPs attached to their target oligonucleotides were hybridised to the probe oligonucleotides at the OS-DFB laser surface. In the following section 4.3.3.1 is a simplified theory to understand this effect of AgNPs on the threshold Energy (E_{th}) required for OS-DFB laser action.

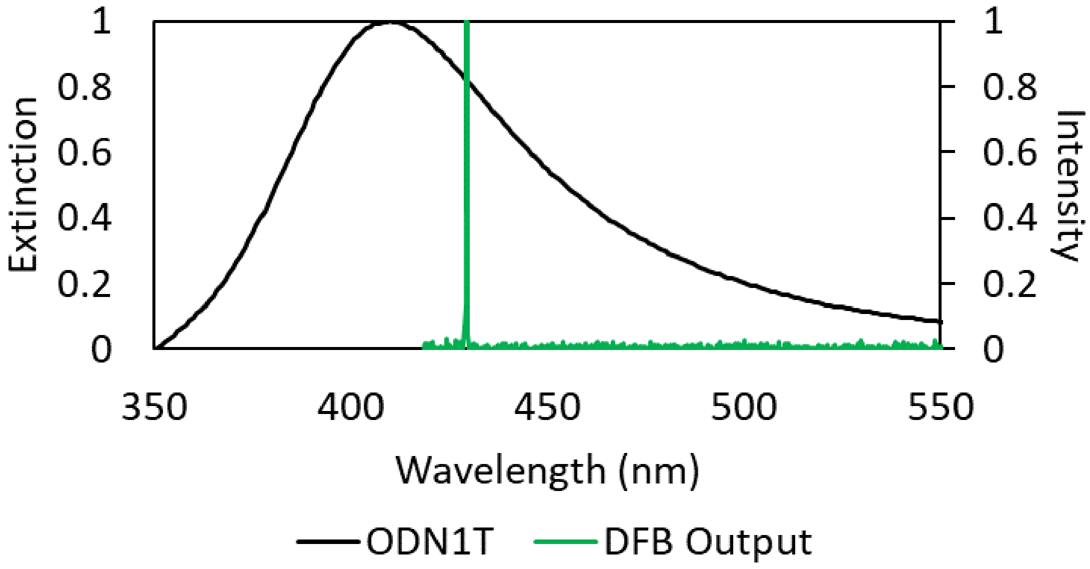

Figure 4.11 - Tr-DFB laser emission spectrum overlapping with AgNP extinction spectrum

4.3.3.1 NP concentration vs Threshold Increase

The behaviour of the laser threshold upon binding of AgNPs can be understood by modeling the system through rate equations [164] as explained below. The formalism is similar to that described in [165] but it is extended here to take into account the modal loss caused by binding of NPs wheras in [165] spontaneous emission quenching was considered. Some assumptions are made:

- The laser operates in the weak coupling and small gain regimes so that feedback and amplification effects can be approximated as decoupled from each other.
- The AgNPs add losses to the mode through scattering and absorption and do not affect significantly the feedback or the confinement of the mode.
- The effects of the AgNPs on the pump absorption and on the spontaneous lifetime of the laser transition are ignored.
- The conjugated polymer gain material is modeled as a 4-level system (although noting that the same result would be obtained if considering a 3-level system).

The electronic levels of this laser sytem are labeled 1 to 4. Level 1 is the ground state of the OS medium. This gain medium is excited by optical pumping to the higher lying level 4, from which it can relax to level 3. The lasing transition is between level 3 and level 2. The rate equations describing the population inversion $\boldsymbol{\Delta N}$ between level 3 and level 2 and the photon number $\boldsymbol{\phi}$ of the mode corresponding to the laser transition are then given by:

$$\frac{d\Delta N}{dt} = R_p - \Delta N B\phi - \frac{\Delta N}{\tau_{32}} \qquad \textbf{Eq. 4.1}$$

$$\frac{d\phi}{dt} = \left[V_a B\Delta N - \frac{1}{\tau_c}\right]\phi \qquad \textbf{Eq. 4.2}$$

where $\boldsymbol{R_p}$ is the pumping rate, $\boldsymbol{B}$ is the stimulated emission rate per photon and $\boldsymbol{\tau_{32}}$ is the lifetime of the transition between level 3 and level 2. $\boldsymbol{V_a}$ is the volume of the mode in the active region, which can also be expressed as a function of the volume of the mode, $\boldsymbol{V}$, and the transversal modal overlap with the active region, $\boldsymbol{\Gamma_a}$: $\boldsymbol{V_a = \Gamma_a V}$. Considering the mode overlap in the other 2 directions is 100%.

At equilibrium $\frac{d\Delta N}{dt} = \mathbf{0}$ and therefore:

$$\Delta N = \frac{R_p}{B\phi + \frac{1}{\tau_{32}}} \qquad \textbf{Eq. 4.3}$$

When $\boldsymbol{\phi}$ is small, e.g. below threshold, the population inversion is:

$$\Delta N_0 = R_p \tau_{32} \qquad \textbf{Eq. 4.4}$$

The so-called small signal modal gain is then:

$$g_0 = \Gamma_a \sigma \Delta N_0 = \Gamma_a \sigma R_p \tau_{32} \qquad \textbf{Eq. 4.5}$$

Where σ represents the strength of the emission resulting from the transition. At lasing threshold the modal gain g_0 must match the losses, which can be writen as $\boldsymbol{\alpha}$, including reabsorption and scattering losses experienced by the mode and the loss from output coupling. The equation for the threshold condition is:

$$g_0 = \alpha = \Gamma_a \sigma R_{pth} \tau_{32} \qquad \textbf{Eq. 4.6}$$

The pumping rate at threshold $\boldsymbol{R_p = R_{pth}}$ is therefore:

$$R_{pth} = \frac{\alpha}{\Gamma_a \sigma \tau_{32}} \qquad \textbf{Eq. 4.7}$$

Note that the intensity of the pump, $\boldsymbol{I_p}$, is directly proportional to the pumping rate as $\boldsymbol{R_p} = \frac{\alpha_p I_p}{h v_p}$ with $\boldsymbol{\alpha_p}$ the pump absorption and $\boldsymbol{h v_p}$ the energy of a pump photon where **h** is plank's constant. Therefore the pump intensity at the laser oscillation threshold is:

$$I_{pth} = \frac{h v_p}{\alpha_p} \frac{\alpha}{\Gamma_a \sigma \tau_{32}} \qquad \textbf{Eq. 4.8}$$

When AgNPs attach to the laser surface, the modal loss increases due to the added scattering and plasmonic absorption of the AgNPs. If $\boldsymbol{\alpha'}$ represents this added loss then using Eq 4.8:

$$\boldsymbol{I'_{pth} = \frac{h\nu_p}{\alpha_p}\frac{\alpha+\alpha'}{\Gamma_a\sigma\tau_{32}} = I_{pth} + \frac{h\nu_p}{\alpha_p}\frac{\alpha'}{\Gamma_a\sigma\tau_{32}}} \qquad \textbf{Eq. 4.9}$$

where $\boldsymbol{I'_{pth}}$ is the pump intensity at threshold in the presence of AgNPs. The ratio of the threshold after and before AgNP binding is expressed as:

$$\boldsymbol{\frac{I'_{pth}}{I_{pth}} = 1 + \frac{\alpha'}{\alpha}} \qquad \textbf{Eq. 4.10}$$

The overlap of the mode with the AgNPs, denoted $\boldsymbol{\Gamma_l}$, can be made explicit:

$$\boldsymbol{\frac{I'_{pth}}{I_{pth}} = 1 + \frac{\Gamma_l\alpha_{NP}}{\alpha}} \qquad \textbf{Eq. 4.11}$$

with $\boldsymbol{\alpha_{NP}}$ the distributed loss of the AgNPs as seen by a wave 100% overlapping the AgNPs. $\boldsymbol{\alpha_{NP}}$ depends linearly on the amount of bound AgNPs. The latter is given by the Michaelis-Menten relation [91]:

$$\boldsymbol{\alpha_{NP} = \frac{\alpha_{NPm}x}{K_d+x}} \qquad \textbf{Eq. 4.12}$$

with $\boldsymbol{x}$ the analyte concentration. $\boldsymbol{K_d}$ is inversely proportional to the binding affinity of the analytes/probes interaction and represents the concentration at which the number of bound AgNPs results in an added loss that is half the maximum value $\boldsymbol{\alpha_{NPm}}$. $\boldsymbol{\alpha_{NPm}}$ is proportional to the maximum analyte binding capacity of the laser sensor. For low **x** (when $\boldsymbol{x \ll K_d}$) the added loss is approximately linear with the concentration:

$$\boldsymbol{\alpha_{NP} \approx \frac{\alpha_{NPm}}{K_d}x} \qquad \textbf{Eq. 4.13}$$

Therefore, at low analyte concentration, the ratio of the threshold fluence after ($\mathbf{E_a}$) and before ($\mathbf{E_b}$) binding is:

$$\frac{\mathrm{E}_a}{\mathrm{E}_b} = \frac{I'_{pth}}{I_{pth}} \approx \mathbf{1} + \boldsymbol{\Gamma_l} \frac{\alpha_{NPm}}{K_d \alpha} \boldsymbol{x} = \mathbf{1} + \boldsymbol{cste} \frac{\boldsymbol{x}}{\boldsymbol{\alpha}}$$ **Eq. 4.14**

The increase in threshold due to binding is therefore proportional to the binding affinity, to the intrinsic loss of the AgNPs, to the analyte concentration and to the modal overlap with the AgNPs; and it is inversely proportional to the overall modal losses before binding. Monitoring of the threshold can therefore be used to detect binding of analytes with the magnitude of the factor $\boldsymbol{\Gamma_l} \frac{\alpha_{NPm}}{K_d \alpha}$ ultimately setting the detection limit.

In practice, the gain saturates. There will be a pump level for which the population inversion cannot increase anymore. Therefore, if the added losses are high, it is possible that laser threshold cannot be achieved.

4.3.3.2 Laser slope efficiency

The slope efficiency, given as the slope of the laser intensity versus the pump fluence above threshold as defined in Chapter 2, is also affected by AgNP binding. Again, the pumping rate at threshold is given by $\boldsymbol{R_{pth}} = \frac{\alpha}{\Gamma_a \sigma \tau_{32}}$. Once the pumping rate exceeds this value, the photon number will grow from spontaneous emission seeding and will eventually reach a steady-state value $\boldsymbol{\phi_c}$ as will the population inversion $\boldsymbol{\Delta N_c}$

By setting $\frac{d\Delta N}{dt} = \frac{d\phi}{dt} = \mathbf{0}$:

$$\boldsymbol{\Delta N_c} = \frac{\mathbf{1}}{BV_a \tau_c} = \boldsymbol{R_{pth} \tau_{32}}$$ **Eq. 4.15**

$$\boldsymbol{\phi_c} = \boldsymbol{V_a \tau_c} \left[\boldsymbol{R_p} - \frac{\Delta N_c}{\tau_{32}} \right] = \boldsymbol{V_a \tau_c} \left[\boldsymbol{R_p} - \boldsymbol{R_{pth}} \right]$$ **Eq. 4.16**

The laser output intensity can therefore be expressed as:

$$\boldsymbol{I_{out}} = \frac{A\phi_c}{V} \boldsymbol{h\nu} = \boldsymbol{A \Gamma_a \tau_c} \frac{\nu}{\upsilon_p} \boldsymbol{\alpha_p} \left[\boldsymbol{I_p} - \boldsymbol{I_{pth}} \right]$$ **Eq. 4.17**

where $\boldsymbol{A}$ is a factor representing the output coupling of the laser mode and the detection efficiency, $\frac{\boldsymbol{\nu}}{\boldsymbol{\nu_p}}$ is the quantum defect, $\boldsymbol{\alpha_p}$ is the pump absorption and $\boldsymbol{\tau_c}$ is the photon lifetime in the laser cavity. Note that $\boldsymbol{\tau_c}$ is reduced with the addition of losses, thereby one expects the slope efficiency of the laser output to decrease with increasing AgNPs (if considering AgNPs do not affect feedback). This could explain results observed in Figure 4.12.

The cavity lifetime can be given as the general expression:

$$\boldsymbol{\tau_c = \frac{1}{c\alpha}} \qquad \textbf{Eq. 4.18}$$

with $\boldsymbol{c}$ the celerity of light. Therefore, with added loss:

$$\boldsymbol{\tau_c{}' = \frac{1}{c(\alpha+\Gamma_l\alpha_{NP})}} \qquad \textbf{Eq. 4.19}$$

If the output coupling is not significantly affected by the added loss then the slope efficiency decreases is given by the ratio:

$$\boldsymbol{\frac{\tau_c{}'}{\tau_c} = \frac{\alpha}{\alpha+\Gamma_l\alpha_{NP}} = \frac{\alpha}{\alpha+\Gamma_l\frac{\alpha_{NPm}}{K_d}x} = \frac{1}{1+a\frac{x}{\alpha}}} \qquad \textbf{Eq. 4.20}$$

It can be argued though that the addition of AgNPs can influence other parameters such as $\boldsymbol{A}$ and $\boldsymbol{\alpha_p}$, which would necessitate a more in-depth analysis of the system if one desires to use the slope efficiency for sensing.

4.3.3.3 Experimental Data

Figure 4.12(a) shows the example of the laser transfer functions before and after incubation with 23 pM target-bound AgNP solution for 10 mins; the thresholds $E_b$and E_a are identified by arrows. The threshold energy required to produce OS-DFB laser action before (E_b) and after (E_a) target bound AgNPs were hybridised to the surface-bound probes increases (because of the presence of surface bound AgNPs). Serially diluted to half concentration from X to $\frac{X}{4}$, from a concentration of X=48.5 pM, AgNPs in 0.3M NaCl PBS samples were prepared. A sample of thiol modified target oligonucleotides ODN_{1t} bound to AgNPs coated with MGITC was split into 100 µl microtube samples. Spun in a centrifuge for 20 mins at 5 krpm, pipetting the supernatant into a waste jar, a concentrated mass of AgNPs remained. This was then dissolved into 100 µl of 0.3 M NaCl PBS and used to immerse OS-DFB laser samples with surface bound probes of ODN_{1p} for 10 mins. At concentration X=48.5 pM tested OS-DFB samples did not reach laser oscillation threshold after AgNP hybridisation.

The ratio $\frac{E_a}{E_b}$, which increases with the concentration, is plotted in Figure 4.12(b) along with the linear fit. Using a simplified form of Eq. 4.14, $\frac{\boldsymbol{E_a}}{\boldsymbol{E_b}} = \boldsymbol{Cx} + \mathbf{1}$ the gradient $\boldsymbol{C} = 0.039$ pM^{-1} is a constant linked to the binding affinity and to $\boldsymbol{\alpha}$. The lowest concentration detected by threshold monitoring in this work is 11.5 pM, a lower limit may be obtained by increasing the resolution of AgNP concentrations that are tested. Alterations to the incubation time with samples of concentration <11.5 pM could allow the detection of lower concentrations as a longer incubation time may allow more hybridization to occur. Bringing the laser emission aligned with the NP resonance would increase absorption and therefore should lower the LOD as well. Figure 4.12(c) confirms the hybridisation of AgNPs by SERS measurements at concentrations from $\mathbf{X}$ to $\frac{\boldsymbol{X}}{\mathbf{4}}$ and using 0.3M NaCl PBS for a 0 pM concentration control.

It is thought samples immersed in higher concentration 48.5 pM AgNP solutions had such a high surface saturation that the gain saturation of the OS-DFB lasers was reached before they could overcome losses incurred from the plasmonic effects of the AgNPs. At this point, maximum population inversion has occurred in the Tr-DFB laser and higher pump energies would not produce a greater gain from the laser medium. This is why the 48.5 pM data point is not found in Figure 4.12(b) as an E_a reading could not be obtained since laser action could not be achieved after exposure to target bound nanoparticles at this level.

At a concentration of 48.5 pM the E_a value was unobtainable as the laser could not reach threshold. The reason for this is that for a given OS-DFB laser structure (i.e. a given Tr thickness) the modal gain has a maximum, called the saturated gain, which cannot be

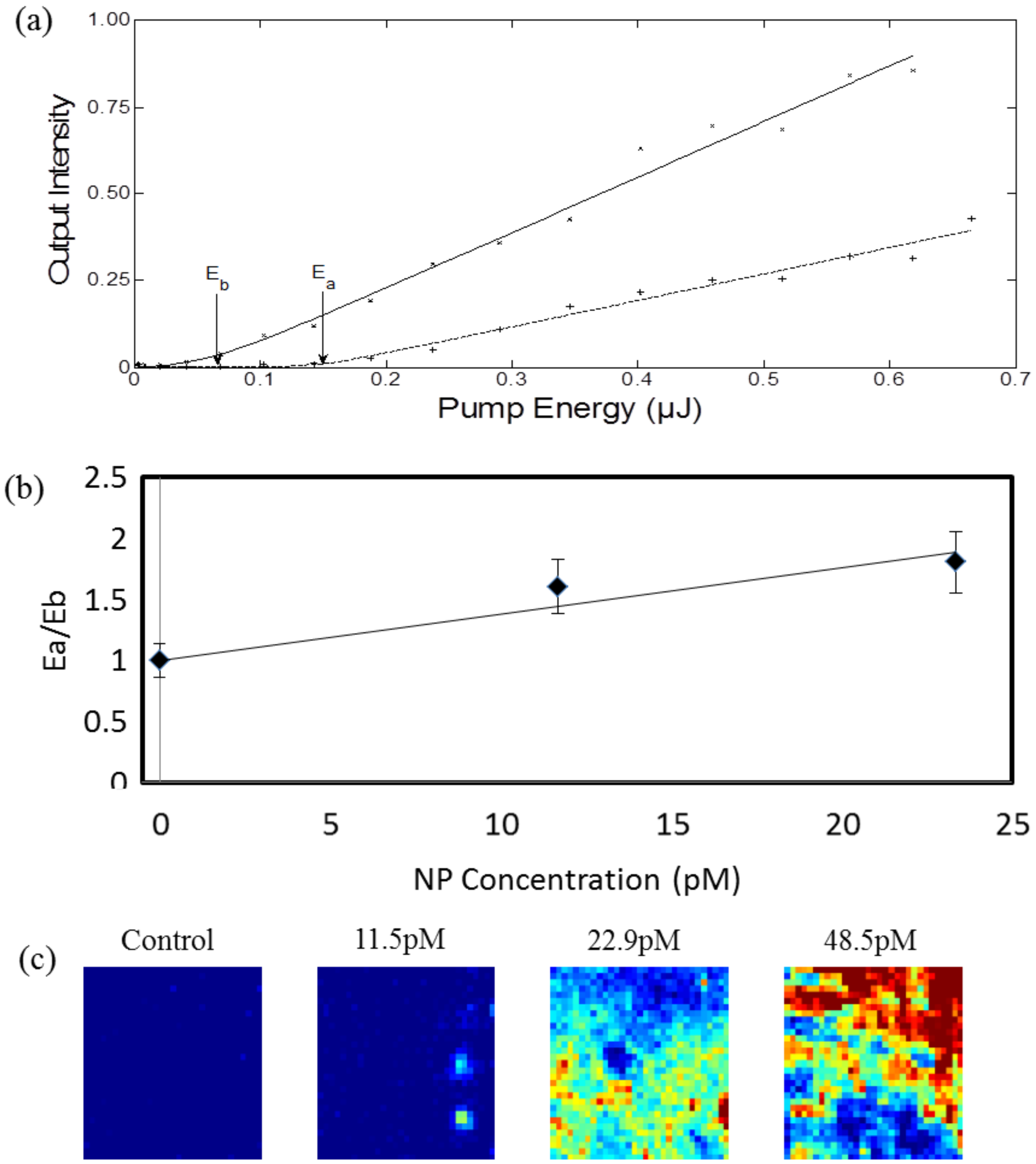

Figure 4.12 - (a)Laser threshold experimental results before and after AgNP binding to surface probes. (b)Threshold energy ratio after/before AgNP binding to surface probes for different concentrations of AgNPs. (c)SERS heatmaps of OS-DFB laser surfaces after oligonucleotide hybridisation binding AgNPs at different concentrations.

exceeded as discussed in the previous section 4.3.3.2. This effect limits the dynamic range of sensing by laser threshold monitoring estimated here to be around 5 dB. The dynamic range could be increased however by increasing the thickness of the Tr film, which would raise the saturated gain value.

Looking back at the wavelength of operation Figure 4.13 shows the laser output before and after incubation with 0 pM and 22.9 pM target bound NP solutions. The dramatic drop in output intensity can clearly be seen in the 22.9 pM sample as a result of surface immobilized AgNPs. The central emission wavelength does appear to blueshift but looking at data from multiple lasers to determine a pattern, results were inconclusive (within a +/-0.13 nm resolution). During threshold calculations, minor changes in wavelength and linewidth were accounted for when fitting the OS-DFB laser output with a Gaussian curve [156].

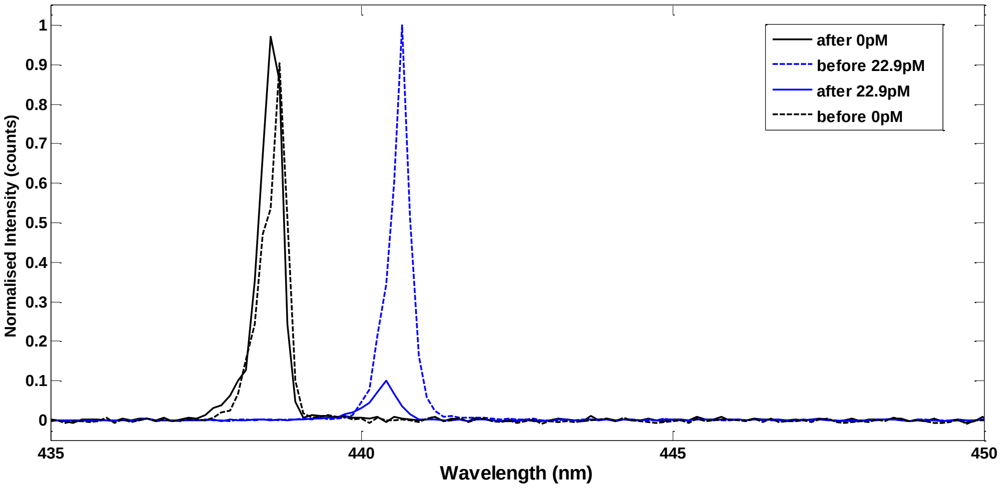

Figure 4.13 - Spectrum of oligonucleotide probe functionalised OS-DFB laser output before and after immersion in 0.3M NaCl PBS (black) and the same solution containing 22.9 pM target bound AgNP.

4.4 CONCLUSION

In summary, 2 main advancements have been made towards the development of a label free oligonucleotide based biosensor utilizing OS-DFB lasers. A covalent attachment strategy to anchor oligonucleotide probes has been developed and confirmed using SERS. The specificity and concentration dependency of the oligonucleotide hybridisation has been demonstrated. An electrostatically bound polyelectrolyte layer is used to covalently immobilize the oligonucleotide probes at the OS-DFB surface. AgNPs bound to target oligonucleotides hybridise specifically to these probes (shown in Figure 4.14) and this is detected down to 11.5pM concentration.

In combination, these findings demonstrate for the first time a novel OS-DFB laser biosensor platform using threshold monitoring. As discussed however the OS-DFB lasers employed as label-free evanescent sensors are not in their current implementation capable of biodetection at pM scales. Successfully confirming the surface functionalization strategy, the plasmonic effects of the AgNPs on the OS-DFB laser threshold can also be used for a label based oligonucleotide biosensing strategy. By comparing the pump fluence required to achieve lasing before and after the hybridisation it is clear that there is a concentration dependant rise in the threshold as a result of AgNPs bound 10-15nm from the OS-DFB surface. Concentrations higher than 48.5 pM resulted in no laser action after hybridisation.

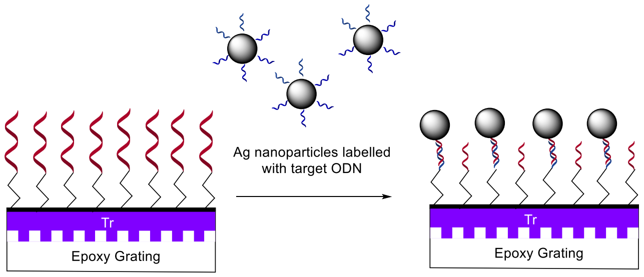

Figure 4.14 - ODN hybridisation capture of target bound AgNPs

Combining these findings with the results discussed in Chapter 3 the sensing capabilities of an OS-DFB laser biosensor demonstrated a wealth of potential for further research and development. With the confirmation of the surface chemistry experiments which lead to a greater shift in the n_{eff} of an OS-DFB laser biosensor could realise such an aim. Chapter 5 will discuss some potential avenues of research to this end and also some modifications to the threshold monitoring paradigm using it as a highly sensitive biosensor comparable to SERS judging by the LOD observed here.

Chapter 5

CONCLUSIONS AND FUTURE DIRECTIONS

5.1 SUMMARY

This thesis reported on research and development of an OS-DFB laser platform motivated by its potential for rapid and inexpensive detection of CVD biomarkers. The main aim was to achieve on this platform, a robust protocol with materials that are more environmentally stable than that of the existing technologies, in particular using a click chemistry approach for biofunctionalization with oligonucleotides probes.

Chapter 1 stated the project goal and motivations, and gave background of the relevant technologies, including the state of the art in DFB laser sensing. With current state of CVD treatment pushing for rapid diagnosis and personalised care the need for a label-free miniaturised device capable of translating current laboratory based methods to the point of care is on the rise. Some promising commercial examples of CVD POC diagnostic tools exist although some recent advancements in optical, photonic based sensing technologies and surface functionalization chemistry discussed in this thesis have the potential to address their shortcomings.

Chapter 2 discussed the principles and fabrication of organic DFB laser sensors. In particular, it covered the different laser materials relevant to this work, the strategy chosen for biofunctionalization, and the multilayer model used in subsequent chapters for calculations of laser mode profiles and effective refractive indices and related discussions.

An assessment for the laser device employed as an evanescent sensor was reported in Chapter 3 to illustrate the main experimental concepts. Two different OSs for DFB lasers, each at a different emission wavelength, Tr and BBEHP-PPV, were studied. Tr absorbs in the near UV and is able to provide gain in the blue spectral region (430nm). BBEH-PPV is a conjugated polymer, which has the advantage of having an optimum absorption in the blue region of the spectrum and therefore lends itself to efficient GaN laser diode and/or LED pumping. The experimental methods and results for the development of a label-free oligonucleotide biosensor with an OS-DFB laser at its core were also discussed. Primarily, wavelength monitoring was investigated as the transduction method. It was found that the optimum OS material in terms of sensitivity for wavelength-based biodetection is the Tr oligomer. Target oligonucleotides could not be detected using the technology in its current form but larger biomarkers, which would specifically bind to oligonucleotides, would be detectable in principle. Aptamers are a class of engineered oligonucleotides, which can specifically bind to large proteins that could produce a measurable output from evanescent sensing.

Chapter 4 outlined a novel transducing method for DFB laser sensors, using threshold instead of wavelength, by which it was confirmed that specific alkyne labelled oligonucleotide probes could be anchored onto the surface. Results demonstrated two main advancements towards the development of a label free oligonucleotide based biosensor utilizing OS-DFB lasers. Firstly, a covalent attachment strategy to anchor oligonucleotide probes was developed and confirmed using SERS. Secondly, the specificity and concentration dependency of the oligonucleotide hybridisation was shown. An electrostatically bound polyelectrolyte layer was used to covalently immobilize the oligonucleotide probes at the OS-DFB surface. AgNPs bound to target oligonucleotides hybridise specifically to these probes and this was detected down to a 11.5pM concentration. Such sensitivity exceeds current POC sensors by an order of magnitude and therefore the approach, while not truly label-free as it uses NPs as enhancers, is attractive for low detection limit tests. In combination, these findings demonstrate for the first time a novel OS-DFB laser biosensor platform using threshold monitoring.

In summary, Chapter 1 tells us the clinical and scientific motivations for the undertaking of this work before Chapter 2 delivers an overview of surface functionalization and the DFB laser technology and how it operates. Chapter 3 outlines a thin film OS-DFB laser biosensor fabrication process and investigates the use of OS-DFB lasers as label-free evanescent sensors. Chapter 4 discusses the use of click chemistry to anchor oligonucleotide probes onto the surface of OS-DFB lasers and the use of AgNP labelled target oligonucleotides for biosensing; also presenting an investigation into the concentration dependant effects of the protocol down to 11.5pM AgNP concentration.

Important steps to realising a true label free OS-DFB laser oligonucleotide biosensor have been taken. A biochemical strategy to anchor probe oligonucleotides to an OS-DFB laser surface has been demonstrated and AgNP enhancements have shown their potential to form a component of a label based biosensing strategy; as well as providing confirmation of the surface functionalisation protocols.

Although not yet realised further avenues of research building on the principles outlined in this thesis could realise a label free POC diagnostic device for CVD biomarker diagnosis. The main obstacles in achieving this are miniaturisation, sensitivity of the OS-DFB laser and repeatability. The remainder of the chapter will discuss these limitations in more detail and then outline some potential solutions as well as other avenues of research that could be explored to improve the technology.

5.2 MINIATURISATION - OPTICAL PUMPING UNIT AND DETECTION

Portability is an important feature of POC diagnostic tools. The OS-DFB laser has great potential for this although the focus of this thesis's work was on gain materials and oligonucleotide bio-functionalization and not on miniaturisation per se. To that end miniaturising the current table top optical set up used in this work is necessary. This can be achieved by using a smaller pump laser like that of a GaN laser diode rather than the Nd:YAG laser used here. Currently, cheap GaN laser diodes in the Institute of Photonics, University of Strathclyde laboratories are being used to deliver pump fluence of around 10-20 μJ.cm^2 per diode; these were such that optically pumping OS-DFBs using these sources for biosensor applications was not possible (typical fluence of Tr lasers were 90 μJ.cm^2). As previously mentioned encapsulation with a high refractive index cladding layer has been used to lower OS-DFB laser thresholds, so that direct diode pumping was achieved. This also has the potential, if engineered correctly, to increase the sensitivity of OS-DFB laser sensors.

Increasing the overlap of the mode profile with the surface region of biomolecular interactions would make OS-DFB lasers more sensitive to the biomarker binding events. So far, results suggest that the hydrogen bonding of short stranded unlabelled oligonucleotide chains cannot be detected with picomolar concentrations of target oligonucleotides without using metallic nanoparticles as enhancers. Results also indicated that the azide modification by probe oligonucleotide chains could not be detected in a similar fashion to other surface functionalisation stages. Micro-RNAs are one candidate biomarker discussed for CVD diagnostics but other larger protein molecules can also be targeted.

A recent class of engineered oligonucleotide probes called Aptamers can be developed to specifically bind to these larger proteins (see section 5.6). As this work has demonstrated a method by which oligonucleotide probes can be anchored to a sensing OS-DFB laser's surface, it could be used to adapt a label free protein based biosensor from the current design. Depending on the availability of binding sites on the azido modified PPL layer using higher concentrations of alkyne labelled probe oligonucleotides or experimenting with higher concentrations of unlabelled target oligonucleotides could allow for evanescent sensing of the oligonucleotide hybridisation.

OS-DFB lasers for biosensing applications must have their repeatability closely monitored, the same tenability in the fabrication process that makes them an attractive research area also means characterisation of these devices must consider many sources of errors. Characterisation may vary not just from one laser to the next but also across the area of a single device between pump spots and side effects of the steps involved to functionalise the OS-DFB laser surface for biosensing interfere with the spectral analysis. These can be mitigated with proper experimental design and data analysis and sometimes just the right technique (see Section 5.5).

The AgNP labelling strategy for biodetection presented in Chapter 4 comes with all the same disadvantages typical of other label based approaches but the LOD outclasses that of commercial solutions. Novel oligonucleotide structures and techniques could adapt the principles this demonstrates to operate as an OS-DFB laser biosensor for unlabelled oligonucleotides as discussed in 5.6.

In this work an Avantes desktop spectrometer was used, in realising a POC device this needs to be replaced with something more compact. The Avantes model used is a general purpose detector, more compact solutions exist with narrower bandwidths which would still be sufficient to sense the range of wavelengths relevant to biosensing. Another alternative comes in the form of recent advancements in using smartphone cameras for biosensing[166]. Removing the need for a special purpose tool for spectral readings would allow for the design of a much simpler diagnostic tool. One could envision that smartphone advancements take the technology to the stage that it could be used as the sensor for multiple diagnostic tests and medical staff could hook up their smart device at each patient bed to take readings and update records with ease.

5.3 ENCAPSULATION

BBEHP-PPV has been the most promising laser material candidate so far for an OS-DFB biosensor using laser diode pumping in terms of threshold. The absorption spectrum of BBEHP-PPV peaks in the blue region around 450 nm, which matches efficient InGaN laser diode emissions much better than that of Tr. While the Tr lasers were shown to be more sensitive evanescent sensors, the BBEHP-PPV lasers were not too far behind and the encapsulation used by Foucher [119] in studies could improve that as well as lowering the lasing threshold to within diode source emission power capabilities.

The encapsulation here meant coating the gain layer with a thin layer of transparent material. This coating increases the symmetry of the waveguide laser structure, which in certain case enhances the mode overlap with the gain region, hence decreases the threshold for laser oscillation. It also pulls the mode towards the sensing surface, which is beneficial for sensitivity, if the coating is not too thick. In [87], a 180nm layer of PVA was utilised to also increase the photo-stability in air of the laser (PVA acting as a barrier to oxygen).

Unfortunately PVA, also used in other studies [90, 103], is water soluble and so unsuitable for biofunctionalization and biodetection strategies targeted by this work. Furthermore, the thickness used in [87] is not thin enough for sensitivity enhancement. Even if a thinner (tens of nm) was used, the refractive index of PVA is a bit low to offer a significant enhancement. A material with a higher refractive index would be needed. Spin on glass [103] has potential to deposit a porous layer of increased refractive index to encapsulate OS-DFB lasers with a material that would withstand the functionalization steps. Modelling has shown[89] that encapsulation can increase the sensitivity of the device provided that the encapsulating layer is not so thick it negates the shift of the mode profile above the OS layer.

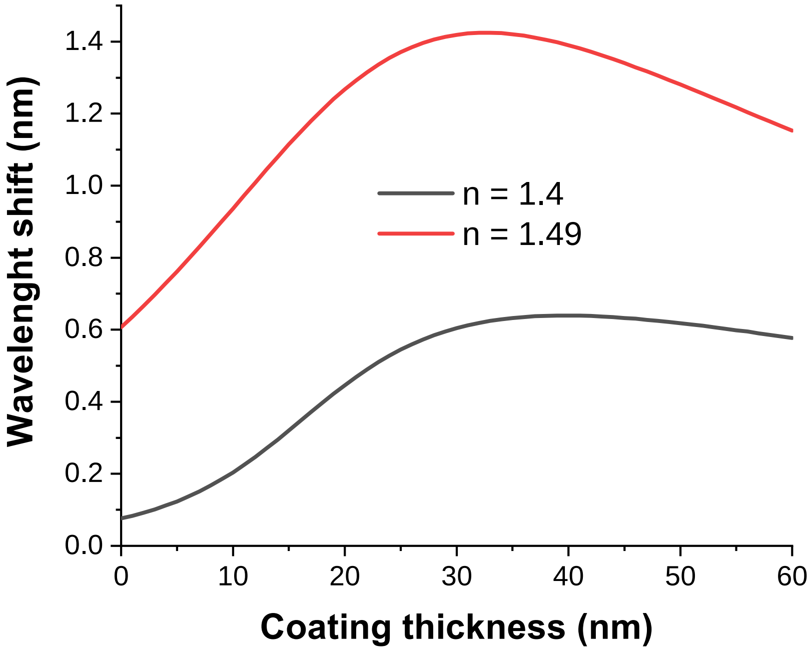

Figure 5.1 – Wavelength shift versus coating layer thickness for a coating of refractive index 1.4 and 1.49.

Figure 5.1 demonstrates this point by plotting the laser wavelength shift versus the coating layer thickness in the case of a Tr laser. The cases of a coating of refractive index n = 1.4 and n = 1.49 are shown. Calculations were made using the model described in Chapter 2. In both cases the optimum is reached for a coating thickness of 25 to 30 nm. Above that the shift decreases. A thin, high refractive index layer is therefore advantageous. Work by Lu et al. [88] has used TiO_2 nanolayer as the coating. TiO_2 has a high refractive index, ideal for maximisation of the sensitivity. However, this approach made use of oxide deposition chamber and was not entirely based on solution processing, increasing the complexity and cost of fabrication. As stated above, a relatively high refractive index can be obtained with spin-on-glass which showed promise to lower the threshold of colloidal quantum dot (CQD) DFB lasers and BBEHP-PPV DFB lasers as discussed by McLellan [103] in his Thesis.

5.4 COLLOIDAL SEMICONDUCTOR NANOCRYSTALS

While the work on DFB laser sensors has mainly utilised organics as the gain materials (dyes, and in this work oligomers and conjugated polymers), another family of solution-processed materials has attractive properties for such application. This other class of material encompasses all types of colloidal semiconductor nanocrystals, and in particular colloidal quantum dots [167]. These are tiny (<20nm) inorganic semiconductor crystals that can emit and amplify light efficiently.[168] They have ampiphilic ligands on their surface and are therefore compatible with solution processing. It means that they are, like some OS materials, amenable to integration with both organic and inorganic materials, enabling the exploration of novel hybrid photonic devices. Their uses include labels for bio-imaging, phosphors in displays and as active elements in light-emitting diodes and lasers.

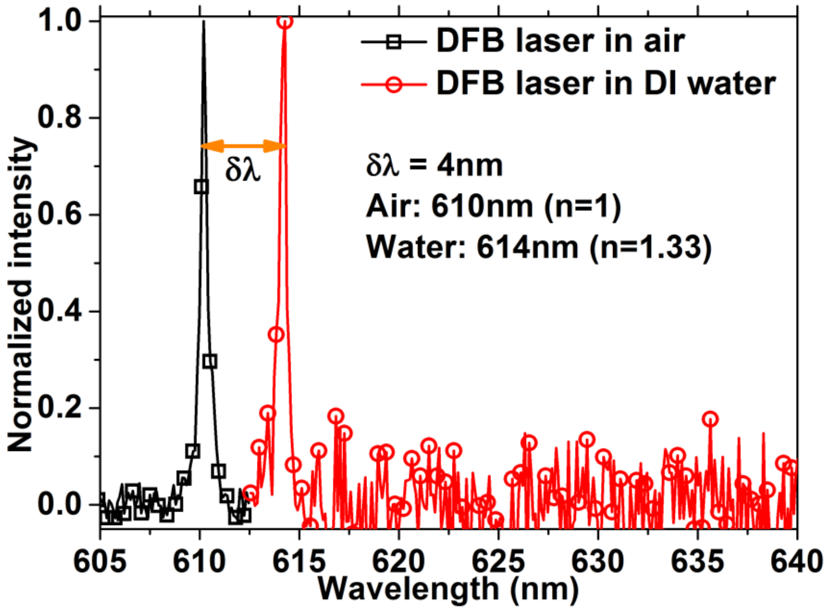

Figure 5.2 – From [169]**: CQD DFB laser emission spectrum in air and in water as proof-of-principle bulk refractive index sensing.**

Different semiconductor alloys including II-VI, III-V and perovskite metal halide enables emission across the visible spectrum.[170] These materials have advantageous properties including high refractive index and a broad absorption spectrum. As discussed in this thesis a high refractive index gain layer is desirable to pull the laser mode towards the surface and hence to increase the sensitivity. A broad absorption spectrum relaxes the tolerance on the pump wavelength. In fact, unlike organics, all visible emitting semiconductor nanocrystal laser materials absorb strongly at the wavelength of high power GaN optical sources (blue-violet).

Progress in CQDs and quantum wells have been going steady over the last 15 years. Low thresholds have been reported for some of them, as well as quasi-CW operation. Overall though, the field is less mature than that of OS lasers and, on average, typical thresholds in pulsed operation are still higher in comparison to OS lasers. Also, while the potential for sensing with CQD DFB lasers is real, very little work has been done in that domain since Guilhabert et al. [169] at Strathclyde reported operation in water and proof of concept bulk refractive index sensing with a CdSe/ZnS CQD laser (see Figure 5.2). Still, these materials are to watch in the future.

5.5 DESIGN, DATA AND THE RIGHT TECHNIQUE

Discussed throughout the experimental results in this text there are demonstrations of the sensitivity of the set-up to disturbances in alignment and surface morphology/composition of the device. These effects were negligible in demonstrating the capabilities of this technology to perform as a biosensor. However, to realise this as a biosensor for a diagnostic tool these sources of error in the analysis would need to be addressed. Adjustments to the alignment could be made so that a smaller, more circular beam is incident on the OS-DFB laser perpendicular to its surface, this is done in minor ways at the beginning of each experiment previously presented. With a smaller beam diameter less energy will be needed from the pump source and spectral variations from surface morphology will be limited now less surface area is being illuminated.

Currently each OS-DFB laser must be analysed in turn as the pump spot must be maintained between readings, taped to the bottom of a well and the well plate secured in the stand with a careful touch this could be achieved but micron scale changes could introduce errors so holes were drilled in the base to secure the stand to the table, this although limited the wells which could be used as the fibre stage only covered a finite region for coupling the OS-DFB laser output. A digitally controlled mechanical stage, accurate to sub-micron scales, capable of accurately aligning the OS-DFB laser output being analysed for coupling into the fibre would improve this process. More so if it can accurately return to the same position allowing comparable spectra and then multiple samples could be analysed concurrently.

Bubbles in solution, solvent evaporation, dust contamination on samples and loose material are just some of the sources of variation between different lasers that could see a Tr-DFB laser with a central emission wavelength as low as 428 nm or as high as 441 nm. Following some simple techniques like pressing the acetate onto the epoxy from the middle ensuring the bubbles were pushed outward during fabrication mitigated these however, a scalable fabrication process could also improve the quality and regularity of the OS-DFB lasers.

While these improvements are appropriate for investigation in a laboratory setting they do not lend themselves well to a commercially available and compact POC device, a solution with a LED array is discussed later in Section 5.8 which would illuminate the need for the mechanical stages and the surface variations could be mitigated with improvements to the control of fabrication in a mass production setting.

As well as the aforementioned experimental controls, statistical methods can also be used for noise reduction, improving the accuracy of the results. Using windowing and statistical analysis techniques Tan et al. [111] have demonstrated combining multiple spectral readings to improve accuracy.

5.6 APTAMERS

An aptamer is defined as “an artificial chemical antibody that is generated from the randomized nucleic acid library by three simple steps: binding, separation, and amplification” [171]. The technology involves the production of successively selected generations of ODN probes based on their binding affinity to a target biomolecule. ODN probe synthesis can be performed with relative ease, when compared to protein based alternatives. While the initial development phase of a biomolecular specific oligonucleotide sequence is costly, aptamers significantly reduce the overhead for probe synthesis in comparison to protein based alternatives.

The protein biomarkers they target are much larger than the ≈20-mer oligonucleotides targeted in this project. These larger molecules will likely shift the n_{eff} of an OS-DFB evanescent sensor more than the pM concentrations of DNA. This larger shift should be observable in the central emission wavelength of the laser output, allowing for label free biomarker detection using Aptamer functionalised OS-DFB lasers. An Aptamer for Troponin I has already been developed[172] and adapting the design to assess this could be a useful next step in the development of this technology for CVD.

5.7 HAIRPIN OLIGONUCLEOTIDES

Hairpin oligonucleotides are another class of nucleic acid based molecules that could be employed as probes for an OS-DFB laser based biosensor[69, 173]. Consisting of a folded oligonucleotide sequence whose tail is hybridised to another part of the chain, they can be ‘unlocked’ by oligonucleotide sequences, which have a stronger binding affinity to the sequence the tail is bound to releasing the tail. By designing a hairpin oligonucleotide in such a way that a target oligonucleotide biomarker ‘unlocked’ the hairpin, as shown in Figure 5.3,

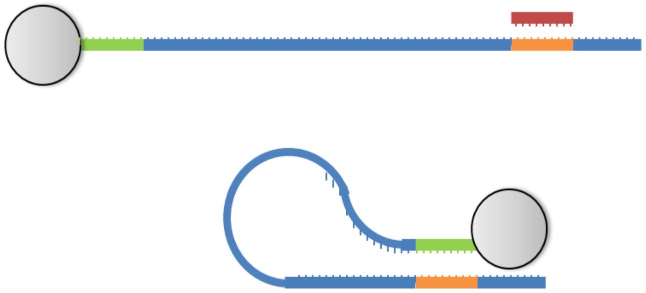

Figure 5.3 Hairpin oligonucleotide attached to an AgNP with locking sequence. in orange, matched to sequence in green but with higher binding affinity to target oligonucleotide in red

the orange section of the probing hairpin oligonucleotide must be designed to bind to both the red and green sequences but have a higher affinity for the red sequence, representing the target biomarker.

Since results shown in Figure 4.9 suggest AgNPs have lower attraction to coated OS-DFB surfaces, using plasmonic labels such as AgNPs the biomarker could theoretically 'unlock' the AgNPs from the surface, reducing their coupling with the OS-DFB output; producing laser action at a lower threshold energy.

5.8 MULTIPLEXING AND NANOPRINTING

Work by Rozkiewicz et al. [145] has demonstrated an effective copper free alternative to CuAAC. By infusing a patterned matrix with the desired alkyne probe oligonucleotides, these could be clicked onto an azide presenting surface without the need for the catalysing Cu(I) and reducing agents used in typical click chemistry. By employing the methods they developed, not only is this process of surface functionalisation simplified but azide presenting OS-DFB laser surfaces could be functionalised with patterns of alternating probes. This means that different pump spots on a single OS-DFB laser could be functionalized to sense for different biomarker targets and could potentially allow the development of a multiplexed label free OS-DFB laser biosensor. This in tandem with a computer automated mechanical stage as mentioned previously would allow a great deal of rapid data collection from many biomarker binding sites. For maximisation of compactness however, a solution with no mechanical stages is preferable. In such a case, it is possible to create an array of interrogating pump laser spots using optics or directly an array of sources (e.g. microLED array). Another way is to illuminate the whole area of the laser sensor with the pump beam and use camera with some sort of frequency discrimination (like a filter) to image the entire laser surface.

5.9 CONCLUSION

This thesis presents the foundational work which has established a successful immobilisation strategy for oligonucleotide probes on the surface of an OS-DFB laser. Using biomarker coated AgNPs, sensing by monitoring of the laser threshold of an OS-DFB laser was demonstrated for the first time. The capture of 40-45 nm AgNP surface bound target oligonucleotides via hydrogen base pair bonding to corresponding probes on the OS-DFB laser surface was shown to be selective down to individual nucleotide. Such detection limits are within diagnostically significant ranges and the protocols have plenty scope for modification to suit a multitude of different applications.

Findings presented in this thesis in combination with other emergent technologies show great promise in developing an Oligonucleotide based label-free OS-DFB laser biosensing platform. This platform could form the core of a POC device allowing for rapid patient-side diagnosis of CVD while also being adaptable to a wide range of other conditions.

REFERENCES

1. Trusheim, M.R., E.R. Berndt, and F.L. Douglas, *Stratified medicine: strategic and economic implications of combining drugs and clinical biomarkers.* Nature Reviews Drug Discovery, 2007. 6: p. 287.

2. Reichlin, T., et al., *Early Diagnosis of Myocardial Infarction with Sensitive Cardiac Troponin Assays.* New England Journal of Medicine, 2009. 361(9): p. 858-867.

3. Qureshi, A., Y. Gurbuz, and J.H. Niazi, *Biosensors for cardiac biomarkers detection: A review.* Sensors and Actuators B: Chemical, 2012. 171-172: p. 62-76.

4. Haughey, A.-M., *A distributed feedback for organic semiconductor laser platform for assessing the risk of cardiovascular disease*, 2014, University of Strathclyde.

5. Organisation, W.H. *WHO | Cardiovascular Diseases (CVDs)*. 2015 [cited 2015; Available from: http://www.who.int/mediacentre/factsheets/fs317/en/.

6. Honikel, M.M., et al., *Facilitating Earlier Diagnosis of Cardiovascular Disease through Point-of-Care Biosensors: A Review.* 2018. 46(1): p. 53-82.

7. Apple, F.S., et al., *National Academy of Clinical Biochemistry and IFCC Committee for Standardization of Markers of Cardiac Damage Laboratory Medicine Practice Guidelines: Analytical Issues for Biochemical Markers of Acute Coronary Syndromes.* Clinical Chemistry, 2007. 53(4): p. 547.

8. Ilhan, F. and S.T. Kalkanli, *Atherosclerosis and the role of immune cells.* World journal of clinical cases, 2015. 3(4): p. 345-352.

9. Herring, N. and D.J. Paterson, *ECG diagnosis of acute ischaemia and infarction: past, present and future.* QJM: An International Journal of Medicine, 2006. 99(4): p. 219-230.

10. Hulka, B. and T. Wilcosky, *Biological markers in epidemiologic research.* Arch. Environ. Health;(United States), 1988. 43(2).

11. Robinson, W.H., et al., *Autoantigen microarrays for multiplex characterization of autoantibody responses.* Nature Medicine, 2002. 8: p. 295.

12. Wong, J., et al., *Rapid detection of antibodies in sera using multiplexed self-assembling bead arrays.* Journal of Immunological Methods, 2009. 350(1): p. 171-182.

13. Tasoglu, S., et al., *Manipulating biological agents and cells in micro-scale volumes for applications in medicine.* Chemical Society Reviews, 2013. 42(13): p. 5788-5808.

14. Wang, L., et al., *Nanostructured substrates for isolation of circulating tumor cells.* Nano today, 2013. 8(4): p. 347-387.

15. Retolaza, A., et al., *Organic distributed feedback laser for label-free biosensing of ErbB2 protein biomarker.* Sensors and Actuators B: Chemical, 2016. 223: p. 261-265.

16. Strimbu, K. and J.A. Tavel, *What are biomarkers?* Current opinion in HIV and AIDS, 2010. 5(6): p. 463-466.

17. Yuan, L.Q., et al., *MicroRNA and Cardiovascular Disease 2016.* Biomed Res Int, 2017. 2017: p. 3780513.

18. Naga Prasad, S.V., et al., *A unique microRNA profile in end-stage heart failure indicates alterations in specific cardiovascular signaling networks.* PLoS One, 2017. 12(3): p. e0170456.

19. Cordes, K.R. and D. Srivastava, *MicroRNA regulation of cardiovascular development.* Circ Res, 2009. 104(6): p. 724-32.

20. Zhang, X.B. and B.S. Chen, *[Perspective of microRNA in cardiovascular-associated diseases].* Zhonghua Xin Xue Guan Bing Za Zhi, 2008. 36(7): p. 661-3.

21. Justino, A., et al., *Comprehensive massive parallel DNA sequencing strategy for the genetic diagnosis of the neuro-cardio-facio-cutaneous syndromes.* European Journal of Human Genetics, 2015. 23(3): p. 347-353.

22. Song, H., Y. Nan, and X.W. Cheng, *Circulating cf-DNA: a promising, noninvasive tool for assessment of early cardio-metabolic risk.* Atherosclerosis, 2014. 233(1): p. 307-9.

23. Elliott, H.R., et al., *DNA methylation, cardio metabolic risk and type 2 diabetes in south Asians and Europeans.* Diabetologia, 2013. 56: p. S149-S149.

24. Hu, R., et al., *Serum sulfatides as a novel biomarker for cardiovascular disease in patients with end-stage renal failure.* Glycoconj J, 2007. 24(9): p. 565-71.

25. Lindahl, B., *Diagnosis and management of patients with suspected acute myocardial infarction.* Scand J Clin Lab Invest Suppl, 2005. 240: p. 93-8.

26. Willcox, B.J., et al., *C-reactive protein, cardiovascular disease and stroke: new roles for an old biomarker.* Expert Rev Neurother, 2004. 4(3): p. 507-18.

27. Hunter, C., et al., *Developing peptide MRM-based assays for cardiovascular biomarker proteins in plasma using a hybrid triple quadrupole linear ion trap mass spectrometer.* Molecular & Cellular Proteomics, 2005. 4(8): p. S217-S217.

28. Heller, W.T., et al., *The Solution Structure of a Cardiac Troponin C−Troponin I−Troponin T Complex Shows a Somewhat Compact Troponin C Interacting with an Extended Troponin I−Troponin T Component.* Biochemistry, 2002. 41(52): p. 15654-15663.

29. de Maat, M. and A. Trion, *C-reactive protein as a risk factor versus risk marker.* Current opinion in lipidology, 2005. 15: p. 651-7.

30. Zoltani, C.K., *Chapter 11 - Cardiovascular toxicity biomarkers*, in *Biomarkers in Toxicology*, R.C. Gupta, Editor. 2014, Academic Press: Boston. p. 199-215.

31. Gaggin, H.K. and J.L. Januzzi, *Biomarkers and diagnostics in heart failure.* Biochimica et Biophysica Acta (BBA) - Molecular Basis of Disease, 2013. 1832(12): p. 2442-2450.

32. Brennan, M.-L., et al., *Prognostic Value of Myeloperoxidase in Patients with Chest Pain.* New England Journal of Medicine, 2003. 349(17): p. 1595-1604.

33. Walldius, G., *The apoB/apoA-I Ratio is a Strong Predictor of Cardiovascular Risk.* 2012.

34. Freeman, A.P., et al., *Comparison of serum myoglobin and creatine kinase MB isoenzyme in early diagnosis of acute myocardial infarction.* British heart journal, 1981. 45(4): p. 389-392.

35. Vasan, R.S., *Biomarkers of cardiovascular disease: molecular basis and practical considerations.* Circulation, 2006. 113(19): p. 2335-62.

36. Nakagawa, K., et al., *Plasma Concentrations of Brain Natriuretic Peptide in Patients with Acute Ischemic Stroke.* Cerebrovascular Diseases, 2005. 19(3): p. 157-164.

37. Marcovina, S.M., et al., *Biochemical and bioimaging markers for risk assessment and diagnosis in major cardiovascular diseases: a road to integration of complementary diagnostic tools.* Journal of Internal Medicine, 2007. 261(3): p. 214-234.

38. Balboni, I., et al., *MULTIPLEXED PROTEIN ARRAY PLATFORMS FOR ANALYSIS OF AUTOIMMUNE DISEASES.* Annual Review of Immunology, 2006. 24(1): p. 391-418.

39. Kost, G.J., et al., *Katrina, the Tsunami, and Point-of-Care TestingOptimizing Rapid Response Diagnosis in Disasters.* American Journal of Clinical Pathology, 2006. 126(4): p. 513-520.

40. Spindel, S. and E.K. Sapsford, *Evaluation of Optical Detection Platforms for Multiplexed Detection of Proteins and the Need for Point-of-Care Biosensors for Clinical Use.* Sensors, 2014. 14(12).

41. Shafiee, H., et al., *Acute On-Chip HIV Detection Through Label-Free Electrical Sensing of Viral Nano-Lysate.* Small, 2013. 9(15): p. 2553-2563.

42. Shafiee, H., et al., *Nanostructured optical photonic crystal biosensor for HIV viral load measurement.* Scientific reports, 2014. 4: p. 4116-4116.

43. Amano, Y. and Q. Cheng, *Detection of influenza virus: traditional approaches and development of biosensors.* Analytical and Bioanalytical Chemistry, 2005. 381(1): p. 156-164.

44. Boltovets, P.M., et al., *Detection of plant viruses using a surface plasmon resonance via complexing with specific antibodies.* Journal of Virological Methods, 2004. 121(1): p. 101-106.

45. Cui, Y., et al., *Nanowire Nanosensors for Highly Sensitive and Selective Detection of Biological and Chemical Species.* Science, 2001. 293(5533): p. 1289.

46. Martinez-Perdiguero, J., et al., *Surface plasmon resonance immunoassay for the detection of the TNFalpha biomarker in human serum.* Talanta, 2014. 119: p. 492-7.

47. Morales-Vidal, M., et al., *Distributed feedback lasers based on perylenediimide dyes for label-free refractive index sensing.* Sensors and Actuators B: Chemical, 2015. 220: p. 1368-1375.

48. Jackowski, G., *Method and device for diagnosing and distinguishing chest pain in early onset thereof*, 1996, SPECTRAL DIAGNOSTICS INC.

49. Washburn, A.L., L.C. Gunn, and R.C. Bailey, *Label-Free Quantitation of a Cancer Biomarker in Complex Media Using Silicon Photonic Microring Resonators.* Analytical Chemistry, 2009. 81(22): p. 9499-9506.

50. Wang, S., F. Xu, and U. Demirci, *Advances in developing HIV-1 viral load assays for resource-limited settings.* Biotechnology Advances, 2010. 28(6): p. 770-781.

51. Klevan, L., et al., *Chemiluminescent detection of DNA probes in forensic analysis.* (0173-0835 (Print)).

52. Walter, B., *Dry reagent chemistries in clinical analysis.* Analytical Chemistry, 1983. 55(4): p. 498A-514A.

53. Turner, A., I. Karube, and G.S. Wilson, eds. *Biosensors : Fundamentals and Applications*. 1987, Oxford University Press: Oxford, New York. 770.

54. Bruins Slot, M.H., et al., *Point-of-care tests in suspected acute myocardial infarction: a systematic review.* Int J Cardiol, 2013. 168(6): p. 5355-62.

55. Cox, K.L., et al., *Immunoassay Methods*, in *Assay Guidance Manual*, G.S. Sittampalam, et al., Editors. 2004: Bethesda (MD).

56. Keefe, A.D., S. Pai, and A. Ellington, *Aptamers as therapeutics.* Nat Rev Drug Discov, 2010. 9(7): p. 537-550.

57. Fonseca Guerra, C., et al., *Hydrogen Bonding in DNA Base Pairs: Reconciliation of Theory and Experiment.* Journal of the American Chemical Society, 2000. 122(17): p. 4117-4128.

58. De Lorimier, R.M., et al., *Construction of a fluorescent biosensor family.* Protein Science, 2002. 11(11): p. 2655-2675.

59. Zangheri, M., et al., *A multiplex chemiluminescent biosensor for type B-fumonisins and aflatoxin B1 quantitative detection in maize flour.* Analyst, 2015. 140(1): p. 358-65.

60. Wang, J., *Electrochemical biosensors: Towards point-of-care cancer diagnostics.* Biosensors and Bioelectronics, 2006. 21(10): p. 1887-1892.

61. Grieshaber, D., et al., *Electrochemical Biosensors - Sensor Principles and Architectures.* Sensors (Basel, Switzerland), 2008. 8(3): p. 1400-1458.

62. Lakowicz, J.R., *Principles of Fluorescence Spectroscopy*. 2007: Springer US.

63. Ivonne Gonzalez, S. and J. La Belle, *The Development of an At-Risk Biosensor for Cardiovascular Disease.* Biosensors Journal, 2012. 1: p. 1-5.

64. Hong, B.J., et al., *DNA microarrays on a dendron-modified surface improve significantly the detection of single nucleotide variations in the p53 gene.* Nucleic Acids Research, 2005. 33(10): p. e90-e90.

65. Rogers, Y.-H., et al., *Immobilization of Oligonucleotides onto a Glass Support via Disulfide Bonds: A Method for Preparation of DNA Microarrays.* Analytical Biochemistry, 1999. 266(1): p. 23-30.

66. Wang, H., et al., *Label-free hybridization detection of a single nucleotide mismatch by immobilization of molecular beacons on an agarose film.* Nucleic acids research, 2002. 30(12): p. e61-e61.

67. Kashmery, H.A., et al., *SERS enhancement of silver nanoparticles prepared by a template-directed triazole ligand strategy.* Chemical Communications, 2015. 51(65): p. 13028-13031.

68. Xi, W., et al., *Click Chemistry in Materials Science.* Advanced Functional Materials, 2014. 24(18): p. 2572-2590.

69. Cañete, S.J.P., W. Yang, and R.Y. Lai, *Folding-based electrochemical DNA sensor fabricated by "click" chemistry.* Chemical Communications, 2009(32): p. 4835-4837.

70. Roda, A., et al., *Progress in chemical luminescence-based biosensors: A critical review.* Biosensors and Bioelectronics, 2016. 76: p. 164-179.

71. Damborský, P., J. Švitel, and J. Katrlík, *Optical biosensors.* Essays In Biochemistry, 2016. 60(1): p. 91-100.

72. Fang, Y., A.M. Ferrie, and G. Li, *Probing cytoskeleton modulation by optical biosensors.* FEBS Letters, 2005. 579(19): p. 4175-4180.

73. Quaranta, G., et al., *Recent Advances in Resonant Waveguide Gratings.* Laser & Photonics Reviews, 2018. 12(9): p. 1800017.

74. Wijaya, E., et al., *Surface plasmon resonance-based biosensors: From the development of different SPR structures to novel surface functionalization strategies.* Current Opinion in Solid State and Materials Science, 2011. 15(5): p. 208-224.

75. Liedberg, B., C. Nylander, and I. Lundström, *Biosensing with surface plasmon resonance — how it all started.* Biosensors and Bioelectronics, 1995. 10(8): p. i-ix.

76. Im, H., et al., *Plasmonic nanoholes in a multichannel microarray format for parallel kinetic assays and differential sensing.* Analytical chemistry, 2009. 81(8): p. 2854-2859.

77. Singh, P., *SPR Biosensors: Historical Perspectives and Current Challenges.* Sensors and Actuators B: Chemical, 2016. 229: p. 110-130.

78. Gallegos, D., et al., *Label-free biodetection using a smartphone.* Lab on a Chip, 2013. 13(11): p. 2124-2132.

79. Chan, L.L., et al., *A label-free photonic crystal biosensor imaging method for detection of cancer cell cytotoxicity and proliferation.* Apoptosis, 2007. 12(6): p. 1061-1068.

80. Groothoff, N., et al., *Distributed feedback photonic crystal fibre (DFB-PCF) laser.* Opt Express, 2005. 13(8): p. 2924-30.

81. Shamah, S.M. and B.T. Cunningham, *Label-free cell-based assays using photonic crystal optical biosensors.* Analyst, 2011. 136(6): p. 1090-1102.

82. Zhou, J., et al., *Double-layered photonic crystal slabs with guided-mode resonance as a high-sensitivity biosensor and application for single nanoparticle detection.* 2016 Conference on Lasers and Electro-Optics (Cleo), 2016.

83. Cunningham, B., et al. *Colorimetric resonant reflection as a direct biochemical assay technique*. in *Technical Digest. MEMS 2002 IEEE International Conference. Fifteenth IEEE International Conference on Micro Electro Mechanical Systems (Cat. No.02CH37266)*. 2002.

84. Ganesh, N., I.D. Block, and B.T. Cunningham, *Near ultraviolet-wavelength photonic-crystal biosensor with enhanced surface-to-bulk sensitivity ratio.* Applied Physics Letters, 2006. 89(2): p. 023901.

85. Chen, W., et al., *Photonic crystal enhanced microscopy for imaging of live cell adhesion.* Analyst, 2013. 138(20): p. 5886-5894.

86. Zhuo, Y., et al., *Single nanoparticle detection using photonic crystal enhanced microscopy.* Analyst, 2014. 139(5): p. 1007-1015.

87. Cunningham, B.T., et al., *Recent Advances in Biosensing With Photonic Crystal Surfaces: A Review.* IEEE Sensors Journal, 2016. 16(10): p. 3349-3366.

88. Lu, M., et al., *Label free biosensor incorporating a replica-molded, vertically emitting distributed feedback laser.* Applied Physics Letters, 2008. 92(26): p. 261502.

89. Haughey, A.M., et al., *Organic Semiconductor Laser Biosensor: Design and Performance Discussion.* Ieee Journal of Selected Topics in Quantum Electronics, 2016. 22(1).

90. Foucher, C., et al., *Diode-pumped, mechanically-flexible polymer DFB laser encapsulated by glass membranes.* Opt Express, 2014. 22(20): p. 24160-8.

91. Haughey, A.M., et al., *An oligofluorene truxene based distributed feedback laser for biosensing applications.* Biosens Bioelectron, 2014. 54: p. 679-86.

92. Haughey, A.M., et al., *An organic semiconductor laser based on star-shaped truxene-core oligomers for refractive index sensing.* Sensors and Actuators B: Chemical, 2013. 185: p. 132-139.

93. Haughey, A.M., et al., *Distributed feedback laser for biosensing applications.* Conf Proc IEEE Eng Med Biol Soc, 2014. 2014: p. 3703-6.

94. Haughey, A.M., et al., *Hybrid organic semiconductor lasers for bio-molecular sensing.* Faraday Discuss, 2014.

95. Haughey, A.M., et al., *Organic distributed feedback laser biosensor.* 2013 Ieee Photonics Conference (Ipc), 2013: p. 161-162.

96. Gao, F.Y., et al., *Design and simulation of label-free biosensor based on the dynamic distributed feedback laser emission.* 2011 Asia Communications and Photonics Conference and Exhibition (Acp), 2012.

97. Heydari, E., et al., *Label-Free Biosensor Based on an All-Polymer DFB Laser.* Advanced Optical Materials, 2014. 2(2): p. 137-141.

98. Samuel, I.D.W. and G.A. Turnbull, *Organic Semiconductor Lasers.* Chemical Reviews, 2007. 107(4): p. 1272-1295.

99. Lu, M., et al., *Plastic distributed feedback laser biosensor.* Applied Physics Letters, 2008. 93(11): p. 111113.

100. Vannahme, C., et al., *Nanoimprinted distributed feedback lasers comprising TiO2 thin films: Design guidelines for high performance sensing.* Laser & Photonics Reviews, 2013. 7(6): p. 1036-1042.

101. Burroughes, J.H., et al., *Light-emitting diodes based on conjugated polymers.* Nature, 1990. 347(6293): p. 539-541.

102. Tessler, N., G.J. Denton, and R.H. Friend, *Lasing from conjugated-polymer microcavities.* Nature, 1996. 382(6593): p. 695-697.

103. McLellan, L., *Colloidal Quantum Dot and Hybrid Lasers*, in *Department of Physics*2018, University of Strathclyde: Glasgow.

104. Ge, C., et al., *Large-area organic distributed feedback laser fabricated by nanoreplica molding and horizontal dipping.* Opt Express, 2010. 18(12): p. 12980-91.

105. Vannahme, C., et al., *Emission wavelength of multilayer distributed feedback dye lasers.* Applied Physics Letters, 2012. 101(15): p. 151123.

106. Ge, C., et al., *Distributed Feedback Laser Biosensor Incorporating a Titanium Dioxide Nanorod Surface.* 2010 Conference on Lasers and Electro-Optics (Cleo) and Quantum Electronics and Laser Science Conference (Qels), 2010.

107. Vannahme, C., M. Dufva, and A. Kristensen. *Nanoimprinted distributed feedback dye laser sensor for real-time imaging of small molecule diffusion*. in *SENSORS, 2014 IEEE*. 2014.

108. Riedl, T., et al., *Tunable organic thin-film laser pumped by an inorganic violet diode laser.* Applied Physics Letters, 2006. 88(24): p. 241116.

109. Nagai, K. and K. Yamashita, *Wavelength Tunability of Plastic Waveguide Laser With Asymmetric Distributed Bragg Reflectors.* Journal of Lightwave Technology, 2015. 33(22): p. 4600-4605.

110. Zhou, Z., et al., *Microfluidic channels incorporating organic distributed Bragg reflector lasers for in situ sensing applications.* Journal of Materials Chemistry C, 2018. 6(10): p. 2565-2572.

111. Tan, Y.F., et al., *Distributed Feedback Laser Biosensor Noise Reduction.* Ieee Sensors Journal, 2013. 13(5): p. 1972-1978.

112. Li, B., et al., *[A Methane Detection System Using Distributed Feedback Laser at 1 654 nm]*. Guang Pu Xue Yu Guang Pu Fen Xi, 2016. 36(1): p. 20-6.

113. Jin, W., *Performance analysis of a time-division-multiplexed fiber-optic gas-sensor array by wavelength modulation of a distributed-feedback laser.* Appl Opt, 1999. 38(25): p. 5290-7.

114. Jahjah, M., et al., *Quartz enhanced photoacoustic spectroscopy with a 3.38 mum antimonide distributed feedback laser.* Opt Lett, 2012. 37(13): p. 2502-4.

115. Gao, F.Y., et al., *Design and simulation of label-free biosensor based on the dynamic distributed feedback laser emission.* Optical Sensors and Biophotonics Iii, 2011. 8311.

116. Liu, X., et al., *Organic semiconductor distributed feedback laser pixels for lab-on-a-chip applications fabricated by laser-assisted replication.* Faraday Discuss, 2014. 174: p. 153-64.

117. Ge, C., et al., *Distributed feedback laser biosensor incorporating a titanium dioxide nanorod surface.* Applied Physics Letters, 2010. 96(16).

118. Hunsperger, R.G., *Acousto-Optic Modulators*, in *Integrated Optics: Theory and Technology*, R.G. Hunsperger, Editor. 2009, Springer New York: New York, NY. p. 201-220.

119. Foucher, C., *Solution-processable, mechanically-flexible lasers*, in *Department of Physics*2015, University of Strathclyde: Glasgow.

120. Svelto, O., *Principles of Lasers*. 2009: Springer US.

121. Han, S.G., et al., *Optically pumped distributed feedback dye lasing with slide-coated TiO(2) inverse-opal slab as Bragg reflector.* Opt Lett, 2014. 39(16): p. 4743-6.

122. Hsiao, V., et al., *High contrast switching of distributed-feedback lasing in dye-doped H-PDLC transmission grating structures.* Opt Express, 2005. 13(10): p. 3787-94.

123. Katarkevich, V.M., et al., *Highly efficient solid-state distributed feedback dye laser based on polymer-filled nanoporous glass composite excited by a diode-pumped solid-state Nd:LSB microlaser.* Appl Opt, 2015. 54(26): p. 7962-72.

124. Wang, Y., *Experimental Methods*, in *Low Threshold Organic Semiconductor Lasers: Hybrid Optoelectronics and Applications as Explosive Sensors*. 2014, Springer International Publishing: Cham. p. 33-57.

125. Wang, Y., *Low-Threshold and Broadly Tuneable Organic Lasers Based on Star-Shaped Oligofluorene Truxenes*, in *Low Threshold Organic Semiconductor Lasers: Hybrid Optoelectronics and Applications as Explosive Sensors*. 2014, Springer International Publishing: Cham. p. 59-77.

126. Wang, Y., *Commercial LED Pumped Organic Semiconductor Lasers*, in *Low Threshold Organic Semiconductor Lasers: Hybrid Optoelectronics and Applications as Explosive Sensors*, Y. Wang, Editor. 2014, Springer International Publishing: Cham. p. 79-100.

127. Chen, Y., et al., *Laser action in a surface-structured free-standing membrane based on a π-conjugated polymer-composite.* Organic Electronics, 2011. 12(1): p. 62-69.

128. Tsiminis, G., et al., *Nanoimprinted organic semiconductor laser pumped by a light-emitting diode.* Adv Mater, 2013. 25(20): p. 2826-30.

129. Belton Colin, R., et al., *Location, Location, Location - Strategic Positioning of 2,1,3-Benzothiadiazole Units within Trigonal Quaterfluorene-Truxene Star-*

Shaped Structures. Advanced Functional Materials, 2013. 23(22): p. 2792-2804.

130. Wang, Y., et al., *Broadly tunable deep blue laser based on a star-shaped oligofluorene truxene.* Synthetic Metals, 2010. 160(13): p. 1397-1400.

131. Kanibolotsky, A.L., et al., *Synthesis and Properties of Monodisperse Oligofluorene-Functionalized Truxenes: Highly Fluorescent Star-Shaped Architectures.* Journal of the American Chemical Society, 2004. 126(42): p. 13695-13702.

132. Wertz, C.F. and M.M. Santore, *Effect of Surface Hydrophobicity on Adsorption and Relaxation Kinetics of Albumin and Fibrinogen: Single-Species and Competitive Behavior.* Langmuir, 2001. 17(10): p. 3006-3016.

133. Mattson, G., et al., *A practical approach to crosslinking.* Molecular Biology Reports, 1993. 17(3): p. 167-183.

134. Samanta, D. and A. Sarkar, *Immobilization of bio-macromolecules on self-assembled monolayers: methods and sensor applications.* Chemical Society Reviews, 2011. 40(5): p. 2567-2592.

135. Kolb, H.C., M.G. Finn, and K.B. Sharpless, *Click Chemistry: Diverse Chemical Function from a Few Good Reactions.* Angewandte Chemie International Edition, 2001. 40(11): p. 2004-2021.

136. Rostovtsev, V.V., et al., *A Stepwise Huisgen Cycloaddition Process: Copper(I)-Catalyzed Regioselective "Ligation" of Azides and Terminal Alkynes.* Angewandte Chemie International Edition, 2002. 41(14): p. 2596-2599.

137. Tornøe, C.W., C. Christensen, and M. Meldal, *Peptidotriazoles on Solid Phase: [1,2,3]-Triazoles by Regiospecific Copper(I)-Catalyzed 1,3-Dipolar Cycloadditions of Terminal Alkynes to Azides.* The Journal of Organic Chemistry, 2002. 67(9): p. 3057-3064.

138. Jewett, J.C., E.M. Sletten, and C.R. Bertozzi, *Rapid Cu-Free Click Chemistry with Readily Synthesized Biarylazacyclooctynones.* Journal of the American Chemical Society, 2010. 132(11): p. 3688-3690.

139. Blackman, M.L., M. Royzen, and J.M. Fox, *Tetrazine ligation: fast bioconjugation based on inverse-electron-demand Diels-Alder reactivity.* Journal of the American Chemical Society, 2008. 130(41): p. 13518-13519.

140. Tao, L., et al., *Anti-epithelial cell adhesion molecule monoclonal antibody conjugated fluorescent nanoparticle biosensor for sensitive detection of colon cancer cells.* Biosens Bioelectron, 2012. 35(1): p. 186-92.

141. Hoyle, C.E., A.B. Lowe, and C.N. Bowman, *Thiol-click chemistry: a multifaceted toolbox for small molecule and polymer synthesis.* Chemical Society Reviews, 2010. 39(4): p. 1355-1387.

142. Fairbanks, B.D., et al., *Reaction Rates and Mechanisms for Radical, Photoinitated Addition of Thiols to Alkynes, and Implications for Thiol−Yne Photopolymerizations and Click Reactions.* Macromolecules, 2010. 43(9): p. 4113-4119.

143. Dyer, E., J.F. Glenn, and E.G. Lendrat, *The Kinetics of the Reactions of Phenyl Isocyanate with Thiols1.* The Journal of Organic Chemistry, 1961. 26(8): p. 2919-2925.

144. Song, W., et al., *A Photoinducible 1,3-Dipolar Cycloaddition Reaction for Rapid, Selective Modification of Tetrazole-Containing Proteins.* Angewandte Chemie International Edition, 2008. 47(15): p. 2832-2835.

145. Rozkiewicz, D.I., et al., *Transfer printing of DNA by "click" chemistry.* Chembiochem, 2007. 8(16): p. 1997-2002.

146. Heuer-Jungemann, A., et al., *Copper-free click chemistry as an emerging tool for the programmed ligation of DNA-functionalised gold nanoparticles.* Nanoscale, 2013. 5(16): p. 7209-12.

147. Agard, N.J., J.A. Prescher, and C.R. Bertozzi, *A Strain-Promoted [3 + 2] Azide−Alkyne Cycloaddition for Covalent Modification of Biomolecules in Living Systems.* Journal of the American Chemical Society, 2004. 126(46): p. 15046-15047.

148. Siemsen, P., R.C. Livingston, and F. Diederich, *Acetylenic Coupling: A Powerful Tool in Molecular Construction.* Angewandte Chemie International Edition, 2000. 39(15): p. 2632-2657.

149. Wang, Q., et al., *Bioconjugation by Copper(I)-Catalyzed Azide-Alkyne [3 + 2] Cycloaddition.* Journal of the American Chemical Society, 2003. 125(11): p. 3192-3193.

150. Chassaing, S., et al., *Click Chemistry in CuI-zeolites: The Huisgen [3 + 2]-Cycloaddition.* Organic Letters, 2007. 9(5): p. 883-886.

151. Chilwell, J. and I. Hodgkinson, *Thin-films field-transfer matrix theory of planar multilayer waveguides and reflection from prism-loaded waveguides.* Journal of the Optical Society of America A, 1984. 1(7): p. 742-753.

152. Jenkins, F.A. and H.E. White, *Fundamentals of Optics*. 1976: McGraw-Hill.

153. Fan, X., et al., *Sensitive optical biosensors for unlabeled targets: A review*. Analytica Chimica Acta, 2008. 620(1–2): p. 8-26.

154. Smith, C.L., et al., *Enhanced transduction of photonic crystal dye lasers for gas sensing via swelling polymer film.* Optics letters, 2011. 36(8): p. 1392-1394.

155. Lipson, A., S.G. Lipson, and H. Lipson, *Optical Physics*. 2010: Cambridge University Press.

156. Herrnsdorf, J., *Organic lasers and nanostructred organic films for hybrid integration*, 2012, University of Strathclyde: Glasgow.

157. Herrnsdorf, J., et al., *Flexible blue-emitting encapsulated organic semiconductor DFB laser.* Opt Express, 2010. 18(25): p. 25535-45.

158. Krivacic, J.R. and D. Urry, *Ultraviolet and visible refractive indices of spectroquality solvents. II. Aqueous solutions of polyhydroxy solutes*. Vol. 43. 1971. 240-6.

159. Seo, T.S., et al., *Click Chemistry to Construct Fluorescent Oligonucleotides for DNA Sequencing.* The Journal of Organic Chemistry, 2003. 68(2): p. 609-612.

160. Vigovskaya, A., et al., *Photo-induced chemistry for the design of oligonucleotide conjugates and surfaces.* Journal of Materials Chemistry B, 2016. 4(3): p. 442-449.

161. Maiti, K.K., et al., *Multiplex cancer cell detection by SERS nanotags with cyanine and triphenylmethine Raman reporters.* Chemical Communications, 2011. 47(12): p. 3514-3516.

162. Wang, G., et al., *Detection of the Potential Pancreatic Cancer Marker MUC4 in Serum Using Surface-Enhanced Raman Scattering.* Analytical Chemistry, 2011. 83(7): p. 2554-2561.

163. Xia, X., et al., *Silica-coated dimers of silver nanospheres as surface-enhanced Raman scattering tags for imaging cancer cells.* Interface Focus, 2013. 3(3): p. 20120092.

164. Svelto, O., *Passive Optical Resonators*, in *Principles of Lasers*, O. Svelto, Editor. 2010, Springer US: Boston, MA. p. 163-203.

165. Rose, A., et al., *Sensitivity gains in chemosensing by lasing action in organic polymers*. Vol. 434. 2005. 876-9.

166. Edwards, P., et al., *Smartphone based optical spectrometer for diffusive reflectance spectroscopic measurement of hemoglobin.* Scientific Reports, 2017. 7(1): p. 12224.

167. Wang, Y. and H. Sun, *Advances and prospects of lasers developed from colloidal semiconductor nanostructures.* Progress in Quantum Electronics, 2018. 60: p. 1-29.

168. Peng, Z.A. and X. Peng, *Mechanisms of the Shape Evolution of CdSe Nanocrystals.* Journal of the American Chemical Society, 2001. 123(7): p. 1389-1395.

169. Guilhabert, B., et al., *Nanosecond colloidal quantum dot lasers for sensing.* Opt Express, 2014. 22(6): p. 7308-19.

170. Dang, C., et al., *Red, green and blue lasing enabled by single-exciton gain in colloidal quantum dot films.* Nature Nanotechnology, 2012. 7(5): p. 335-339.

171. Gopinath, S.C.B., et al., *Chapter 2 - Influenza viral infection in the respiratory system—potential ways of monitoring*, in *The Microbiology of Respiratory System Infections*, K. Kon and M. Rai, Editors. 2016, Academic Press. p. 33-43.

172. Dorraj, G.S., et al., *Selection of DNA aptamers against Human Cardiac Troponin I for colorimetric sensor based dot blot application.* Journal of Biotechnology, 2015. 208: p. 80-86.

173. Cabello-Villegas, J. and E.P. Nikonowicz, *Discriminating duplex and hairpin oligonucleotides using chemical shifts: application to the anticodon stem-loop of Escherichia coli tRNA(Phe).* Nucleic acids research, 2000. 28(15): p. E74-E74.

APPENDIX I: MATLAB CODE

This appendix describes sections of Matlab code used to automate data analysis of DFB laser output data from an Avantes Spectrometer(utilizing functions described by J. Herrnsdorf in his 2012 Thesis) and .spc file SERS data from a Raman Reinshaw Spectrometer. They were developed in MATLAB R2014a.

I.1 STHRESHOLDING

This function automated the steps which calculated the appropriate inputs for and executed the *softthreshold* function from raw experimental data. User input was required to determine the saturation point observed with increasing pump energy so that the correct fit could be made when passing inputs to *softthreshold*.

During these experiments the waveplate shown in Figure 3.3 would be moved through values from 0 to *a* in incements of 2, and the filter wheel set at value *b*. *E* and *dE* represent the pump energy readings taken by the ThorLabs power meter of the average and standard deviation respectively. Using *peakdecomposition ll* and *ul* would be calculated at the full-width half maximum of the DFB laser output. Finally *lam* and *int* represent the outputs from *readroh* of the lambda and intensity values read by an Avantes Spectrometer for increasing values of the waveplate.

```
function [] = sthresholding(a, b, E, dE, ll, ul, lam, int)
% Author: Glenn McConnell
% Last Revision: 04/06/2014
% sthreshilding:    Takes in the values required to perform soft
%                   thresholding to plot graphs of the lasers
%                   characteristics. requires the inputs:
%
%                   a: Maximum alpha value
%                   b: Beta value
%                   E: Mean Energy of pump beam
%                   dE: Standard Deviation of pump beam energy
%                   ll: lower bound of laser bandwidth
%                   ul: upper bound of laser bandwidth
%                   lam: matrix of lambda values
%                   int: matrix of intensity values
%
%                  function uses minilite and softthreshold functions
%                   written by Johannes Herrnsdorf.

% initializes array of alpha values                                 %
alpha = [0:2:a];

% calculates Ep and deltaEp using minilite function                 %
[Ep,deltaEp] = minilite(alpha,b,E,dE);

% sets C value to test for lambda limits                            %
C = lam{1} >ll & lam{1} <ul;

% initializs I to array of 0's                                      %
I=zeros(size(lam,1),1);

% for each data set, sum the intensity values between the lambda
bounds %
for i=1:size(lam,1)
I(i) = sum(int{i}(C));
end
% plot the output intensity against Ep and ask user for Ep saturation
%
% value                                                             %
figure
plot(Ep,I)
sat = str2double(inputdlg('Where does the graph saturate?'));

% set C to test Ep for saturation value and display graph of values
%
C=Ep<sat;
[Eth,Isat,kappa] = softthreshold(Ep(C),I(C))
plot(Ep(C),I(C))%
```

I.2 SERS MAPPING

Output from the Reinshaw Raman Spectrometer would be in the form of spc files. Using the function *tgspcread* the data could be loaded into *SPCStruct* data types, the intensity of the 1171 cm^{-1} signature peak of MGITC would then be extracted and normalised for baseline corrected SERS mapping scan data. These normalised values would then be plotted on heat maps of the scan area of DFB laser samples before correcting the contrast of the heatmaps for effectively display of the data.

```
%%%%%%%%%%%%%%%%%%%%%%%%%%%%%%%%%%%%%%%%%%%%%%%%%%%%%%%%%%%%%%
%Used to plot normalised, baseline corrected intensity values%
%of 1171cm-1 peak values in SERS mapping scan data.          %
%%%%%%%%%%%%%%%%%%%%%%%%%%%%%%%%%%%%%%%%%%%%%%%%%%%%%%%%%%%%%%

%Define the names of the different spc files%
name = ['0-0'; '0-3'; '0-5';'1-0']
sqs = 31 %Pixel Width of square heat maps%
L = size(name)

%Read in data to a SPCstruct array for each element of names%
for i=1:L
struc(i) = tgspcread(strcat(name(i,:),'.spc'));
end

%Starting with the first element, find the 1171 cm-1 data point%
p=1;
while struc(1).X(p)>1171
p=p+1;
end

%For every SPCstruct Baseline correct the spectra%
for s=1:L
for i=1:struc(s).Header.NumScans
base(:,i) = Baseline(double(struc(s).Y(:,i)),201,3);
signal(s,i)=base(p,i);
end
end

%normalise the data and store in sqn%
Max = max(max(signal));
for i=1:L
temp =[];
for y=1:sqs
temp=[temp;signal(i,(y-1)*sqs+1:y*sqs)];
end
sqn(:,:,i)=temp/Max;
end
```

```
%assign colour map values to normalised 1171 intensity readings%
sqi = uint8(sqn*255);
for s = 1:L
Spn(s) = subplot(1,4,(5-s)),image(sqi(:,:,s));axis off
Smean(s) = mean(mean(sqi(:,:,s)));
Sstd(s) = std2(sqi(:,:,s));
end

%adjust contrast of colour map%
colormap(jet(128));
```

I.2.1 BASELINE CORRECTION

```
function [bcy] = Baseline(Y, WindowWidth, PolynomialOrder)
% Author: Glenn McConnell
% Last Revision: 01/07/2015
% Baseline:        Returns Y baseline corrected using Savitzky-Golay
%                  sliding polynomial filter smoothing
%                  u: number of elements to plot
%                  lam: matrix of lambda values
%                  int: matrix of intensity values


% Now smooth with a Savitzky-Golay sliding polynomial filter
ww = WindowWidth;
po = PolynomialOrder;
baselineY = sgolayfilt(Y, po, ww);
% Now subtract the baseline from the original data
bcy = Y - baselineY;
```

I.3 PLOTTING MULTIPLE SPECTRA

One final piece of code that proved extremely useful in data analysis was a script written and detailed below which would plot a series of spectra giving each series a progressively from blue to magenta and then darkening to black. This allowed trends in a large dataset of many spectrum to be observed.

```
function [] = rplot(u, lam, int)
% Author: Glenn McConnell
% Last Revision: 01/07/2015
% rplot:             Plots u of the elements of lam and int
%                    with a progressive colour gradient.
%
%                    u: number of elements to plot
%                    lam: matrix of lambda values
%                    int: matrix of intensity values

figure
hold on

% for every element up to u%
for i = 1:u

    %Set colour Blue to Cyan%
    if i < u/6
        col = [0,6*i/u,1];
    %Set colour Cyan to Green%
    elseif i < u/3
        col = [0,1,1-6*(i-u/6)/u];
    %Set colour Green to Yellow%
    elseif i < 3*u/6
        col = [6*(i-u/3)/u,1,0];
    %Set colour Yellow to Red%
    elseif i < 2*u/3
        col = [1,1-6*(i-3*u/6)/u,0];
    %Set colour Red to Magenta%
    elseif i < 5*u/6
        col = [1,0,6*(i-2*u/3)/u];
    %Set colour Magenta to Black%
    else
        col = [subplus(1-6*(i-5*u/6)/u),0,subplus(1-6*(i-5*u/6)/u)];
    end

    %Plot values%
    plot(lam(i),int(i),'color',col)

end
```

APPENDIX II: PUBLICATIONS

II.1 CONFERENCES

[1] - G. McConnell, J. Carreira, S. Mabbott, O. Knibolotskyy, P. Skabara, D. Graham, M. Dawson, G. Burley, N. Laurand, *DNA-functionalised organic laser biosensor using click chemistry (oral).* Photon (2016), University of Leeds, Leeds, UK

[2] - G. McConnell, J. Carreira, S. Mabbott, O. Knibolotskyy, P. Skabara, D. Graham, M. Dawson, G. Burley, N. Laurand *Click chemistry functionalization of organic lasers for oligonucleotide-based sensing (poster)*, 5th International Conference on Bio-sensing Technology (2017), Riva Del Garda, Italy

II.2 PAPERS

[3] - A. Haughey, G. McConnell, B. Guilhabert, G. A. Burley, M. D. Dawson and N. Laurand, *Organic Semiconductor Laser Biosensor: Design and Performance Discussion*, IEEE Journal of Selected Topics in Quantum Electronics (2016) **22** (1), 6-14, DOI: 10.1109/JSTQE.2015.2448058

[4] - G. McConnell, S. Mabbott, A. L. Kanibolotsky, P. J. Skabara, D. Graham, G. A. Burley, and N. Laurand, *Organic Semiconductor Laser Platform for the Detection of DNA by AgNP Plasmonic Enhancement,* Langmuir (2018) **34** (49), 14766-14773, DOI: 10.1021/acs.langmuir.8b01313

Organic semiconductor laser biosensor: design and performance discussion

Anne-Marie Haughey, Glenn McConnell, Benoit Guilhabert, Glenn A. Burley, Martin D. Dawson *Fellow, IEEE,* and Nicolas Laurand, *Member, IEEE,*

***Abstract*—Organic distributed feedback lasers can detect nanoscale materials and are therefore an attractive sensing platform for biological and medical applications. In this paper, we present a model for optimizing such laser sensors and discuss the advantages of using an organic semiconductor as the laser material in comparison to dyes in a matrix. The structure of the sensor and its operation principle are described. Bulk and surface sensing experimental data using oligofluorene truxene macromolecules and a conjugated polymer for the gain region is shown to correspond to modeled values and is used to assess the biosensing attributes of the sensor. A comparison between organic semiconductor and dye-doped laser sensitivity is made and analyzed theoretically. Finally, experimental and theoretical specific biosensing data is provided and methods for improving sensitivity are discussed.**

***Index Terms*—Distributed feedback devices, biophotonics, organic semiconductors.**

I. Introduction

STRATIFIED medicine is a 21st century concept aimed at enabling clinicians to tailor treatment for individual groups of patients through the use of biological markers (biomarkers) [1]. This approach requires sensitive and compact platforms for point-of-care biomarker detection that are simple to implement and operate and provide rapid results. Multiplexed detection in a single test is also desirable as diagnosis will rarely be dependent on one biomarker. Organic semiconductor distributed-feedback (DFB) lasers, functionalized for surface sensing, have the potential to meet this need.

Organic DFB laser sensors are evanescent wave sensors that can enable label-free optical biomarker detection. They can be fabricated with low-cost techniques via the nanopatterning of a thin-film of gain material. Specific biomarker detection is achieved by functionalizing the surface of the gain material with probe molecules that specifically bind to an analyte. Upon analyte binding, a change in refractive index at the laser surface results in a change in the effective refractive index of the laser mode and in turn induces a shift in the emission wavelength, as explained in section IIB. This change in wavelength can be monitored for sensing.

Evanescent wave optical detection is the basis of several commercial technologies often seen as the ‘gold standard’ for biodetection, but the miniaturization of precise, bulky optical systems for injection and collection of the light into and from the transducer is difficult. The integration of organic lasers into a sensing platform, that can be remotely excited with non-critical alignment, can help alleviate this miniaturization problem, making them ideal transducers for compact point-of-care diagnostics. Furthermore, label-free detection using evanescent waves usually necessitates a trade-off between resolution and sensitivity. The trade-off arises because the detection of small refractive index perturbations is dependent on monitoring changes in an optical resonance [2]. The limit of detection of the system is linked to the magnitude of the resonance shift for a given refractive index change (the sensitivity) and is limited by the inherent bandwidth of the resonance (the resolution). To optimize the limit of detection of an evanescent wave based system, the magnitude of the resonance shift must be maximized while simultaneously minimizing the resonance bandwidth. Doing both concurrently is a non-trivial task but can be achieved with a DFB laser because, in this case, the resonance is the coherent output of the laser, which is characterized by a narrow linewidth for single mode oscillation. Finally, organic DFB lasers can be excited optically at any position within their surface to generate coherent emission normal to the laser structure, resulting in simple implementation whilst maintaining sensitivity. The flexibility to excite the DFB laser surface at any point also raises the prospect for multiplexed detection.

The first reports of organic DFB lasers for biosensing utilized gain material that incorporated dyes at low density into a polymeric matrix [3]. Recently, we expanded the concept to the use of a neat organic semiconductor (OS) gain region [4]. Organic semiconductor materials have higher refractive indices (from 1.6 to above 2) than dye-doped materials. The dye concentration in a polymer host must be kept relatively low (≈10%) to prevent fluorescence quenching and the refractive index of the transparent polymer host is typically around or below 1.5 [3]. We predict that the use of a higher index semiconductor gain layer, which takes the form of a dense thin-film, will result in improved surface sensing capabilities due to an increase in the strength of the laser mode intensity at the laser surface (where the biodetection region is situated). Another advantage of an OS gain layer is the potential for lower lasing thresholds, opening up the possibility for diode pumping with either InGaN laser diodes or LEDs and would therefore support miniaturization [5], [6].

In this paper, we study theoretically and experimentally the sensitivity advantage of using a high index OS as the gain region of a DFB laser sensor. We describe a model for the design of future OS DFB laser sensors that enables the biomarker detection sensitivity to be determined and maximized through optimization of the device structure. We expand upon previous models by including the effect of refractive index dispersions of the substrate and of the OS. And we investigate the interaction of the laser mode with the biodetection region at the sensor surface. We also discuss potential sensitivity benefits of using an OS as the laser gain material in comparison to other organic materials. Oligofluorene truxene macromolecules and a conjugated polymer are the OS gain materials used for the experimental data presented in this paper although properties

AM. Haughey, G. McConnell, B. Guilhabert, M.D. Dawson and N. Laurand are with the Institute of Photonics, University of Strathclyde, Glasgow, G4 0NW, UK e-mail: (annemarie.haughey@fraunhofer.co.uk).

G.A. Burley is with Department of Pure and Applied Chemistry, University of Strathclyde, Glasgow, G1 1XL, UK.

Manuscript received March 31, 2015; revised xx xx, 20xx.

discussed can be extended to other OS gain materials.

II. Design, methods and modeling

A. Device fabrication and optical set-up

A schematic of an OS (here oligofluorene truxene, (T3) [7]), second order DFB laser is shown in Fig. 1. The device consists of a UV-curable optical epoxy substrate (Norland 65, Norland Products), nano-patterned with a diffraction grating having a period (Λ) of 277 nm and a modulation depth of ≈50 nm and a thin (≈70 nm), dense T3 film. The refractive indices of the substrate and T3 are 1.54 and 1.81 at a wavelength of 430 nm respectively. When a conjugated polymer (BBEHP-PPV [8]) is used as the gain material, DFB lasers had a period of 350 nm, a gain layer thickness of 220 - 250 nm and a refractive index of 1.64 at a wavelength of 540 nm. As mentioned previously, OS gain materials have a higher refractive index than dye-doped gain materials which leads to greater confinement of the electric field within the gain layer, a greater overlap with the detection region at the laser surface and ultimately higher light matter interactions. Therefore, by utilizing an OS as the gain material rather than a dye-doped polymer, there is the potential to both match, if not improve upon, the sensitivity and resolution values and enhance the overall sensor performance. The lasing threshold of OS DFB lasers tends to be lower than those of dye-doped lasers [4], [9]. A lower lasing threshold makes pumping with compact light sources, such as gallium nitride based laser diodes, a possibility [6]. Laser diode based pumping will enable the miniaturization of the DFB laser sensing system and if off-the-shelf components can be used, such as mass produced ‘Blu-ray’ diodes, it should also enable the technology to be competitively priced.

The laser fabrication process have previously been described elsewhere [4] but are summarized here. The OS layer, which acts as the gain region, is deposited onto the nano-patterned substrate by spin-coating from a toluene solution. The spin-coating speed can be used to tune the thickness of the gain layer which has implications for the device performance. To ensure reproducible and uniform gain layers were achieved through spin coating, a large volume of OS solution was deposited relative to the surface area of the substrate; the surface area of the substrate was dependent on what vessel the laser was used with (see below). By using a solution volume in excess of that required to form the film, and ensuring that the substrate was flat (it was taped to a piece of glass), a constant gain layer thickness was produced and any excess solution was removed from the surface. Several different vessels were used to house the DFB lasers and test solutions for the experimental work, including a large quartz cuvette (Starna), a custom made demountable quartz cuvette (Comar) and a 24 well microtiter plate (TPP). When using the large cuvette or the 24 well plates, lasers were fixed in place using tape (Kapton). When the demountable cuvette was used, the grating imprinted epoxy was fixed to the flat face of the cuvette using optical epoxy (Norland 65) and cured for ≈2 minutes before spin-coating the gain layer as described in [4].

Lasers were excited using a frequency-tripled, Q-switched Nd:YAG pump laser (355 nm, 10 Hz repetition, 5 ns pulses). When a cuvette was used to house a laser, the laser was pumped through the cuvette and epoxy substrate at an angle of ≈45^o to the surface normal (chosen simply for ease of emission collection). Outcoupled laser emission was collected via a 50-μm core optical fiber, positioned normal to the cuvette surface at a distance of ≈20 mm, and connected to a grating-coupled CCD spectrometer (Avantes) with a resolution of 0.13 nm. When using 24 well plates, lasers were pumped through the plate and epoxy, normal to the laser plane as shown in Fig. 1. A dichroic mirror was used to direct the pump onto the laser within the plate, and to cut any of the pump when collecting DFB laser emission with the same optical fiber/spectrometer mentioned previously.

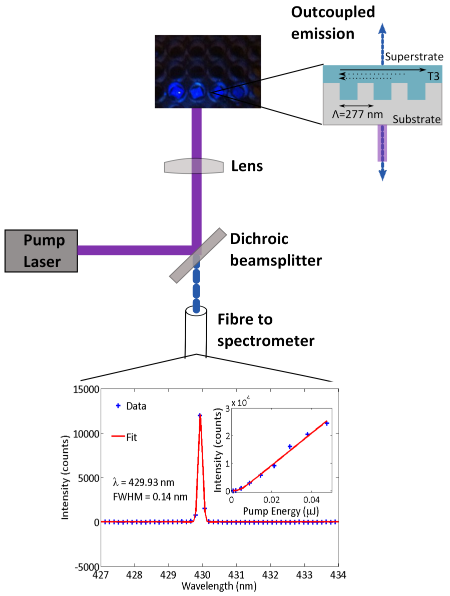

Figure 1. Schematic representing the implementation of the organic laser sensor. Photograph shows T3 lasers in wells under UV illumination. An example of a typical T3 emission spectra with the laser exposed to air, and a typical lasing threshold is also shown.

B. Theoretical model

The out-coupled laser emission for a DFB laser is described by the Bragg equation, Eq. 1, where m is the order of diffraction (m=2 for vertically emitting DFB lasers), λ is the wavelength of the DFB laser, n$_{eff}$ is the effective refractive index of the laser mode and Λ is the grating period as previously defined.

$$m\lambda = 2n_{eff}\Lambda \tag{1}$$

The effective refractive index for the device, which defines the laser emission wavelength, is dependent on the refractive indices of the substrate and superstrate materials, any material bounded by the substrate and superstrate and the thickness of this bounded region. Changes in any of these parameters results in a shift in the emission wavelength of the laser, therefore, changes in the emission wavelength can be used to sense bulk refractive index changes in the superstrate or to detect the immobilization of analytes at the laser surface. A multilayer transfer matrix model of a DFB laser can be adapted for numerical evaluation of the effective refractive indices of the laser modes, the expected wavelength shifts for both bulk and surface refractive index sensing, and the mode profile, and was used for the evaluation of our lasers. A full mathematical description of the model is described elsewhere [10] but a brief summary of the key details are provided here in the context of a DFB laser.

The DFB laser structure is represented in Fig. 2. A laser mode can be approximated as a waveguide mode of this multi-

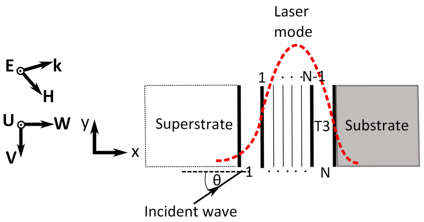

Figure 2. Multilayer stack of N thin films bounded by semi-infinite substrate and superstrate layers. The laser mode intensity profile is also represented. Here we take T3 as an example but other gain material would be equally valid.

layered structure oscillating at the frequency of maximum gain provided by the laser material. The laser gain layer and any other layers adjacent to the gain layer (with layer 1 being the topmost layer adjacent to the superstrate and layer N being the T3 layer) are enclosed between semi-infinite superstrate and substrate layers. The boundaries between layers 1 to N are numbered 1 to N-1. The direction cosines are given by $\alpha = ncos\theta = (n^2 - \beta^2)^{1/2}$ and $\beta = nsin\theta$ as indicated in Fig. 2, and where β is the propagation constant. Properly designed DFB lasers oscillate on the fundamental TE_0 mode and therefore the model is designed to solve for the TE_0 mode only, although it can equally be applied to other modes, including TM modes. The plane of incidence is the xy plane and the interfaces between the layers of the DFB laser are parallel to the yz plane. Therefore, the only material variation for the stack of layers occurs in the x direction, as shown in Fig. 2. For a TE wave, E_x and E_y, and therefore H_z, are equal to zero and E_z, H_y and H_x are given by Eq. 2a-c.

$$E_z = U(x)e^{i(k\beta y - \omega t)} \tag{2a}$$

$$H_y = V(x)e^{i(k\beta y - \omega t)} \tag{2b}$$

$$H_x = W(x)e^{i(k\beta y - \omega t)} \tag{2c}$$

The relationship between the transverse amplitudes of the field components, $U(x)$ and $V(x)$, is given by Eq. 3a-b, where γ ($\gamma = \frac{ncos\theta}{z_0}$) can be defined as $\gamma = \frac{\alpha}{c\mu}$ in non-magnetic media, where c is the speed of light and μ is the magnetic permeability. At the boundary between two adjacent layers the tangential components of the electric and magnetic fields (U and V) are continuous and W, the amplitude of the component normal to the boundary between the layers, is proportional to U. The total field can therefore be specified using the pair of simultaneous equations for U and V given in Eq. 3a and b.

$$\frac{dU}{dx} = \frac{ik\alpha}{\gamma}V \tag{3a}$$

$$\frac{dV}{dx} = ik\gamma\alpha U \tag{3b}$$

The knowledge of U and V at any boundary of the multilayer is sufficient to describe the entire transverse field using a transfer matrix $\mathbf{M}$. The particular components of matrix $\mathbf{M}$ for the stack of N layers between position x_n and x_{n-1} are given by matrix $\mathbf{M}_n$ in Eq. 4 where Φ is the phase thickness of the layer and and is given by $\Phi_n = k\alpha_n(x_n - x_{n-1})$.

$$\mathbf{M}_n = \begin{pmatrix} cos\Phi_n & \frac{-i}{\gamma_n}sin\Phi_n \\ -i\gamma_n sin\Phi_n & cos\Phi_n \end{pmatrix} \tag{4}$$

Each of the N layers of the multilayer stack is described by a matrix resembling Eq. 4. The transfer matrix ($\mathbf{M}$) combining all of the N layers is given by the product of each of the matrices for the respective individual layers, Eq. 5.

$$\mathbf{M} = \prod_{n=1}^{N} \mathbf{M}_n = \begin{pmatrix} m_{11} & m_{12} \\ m_{21} & m_{22} \end{pmatrix} \tag{5}$$

Eq. 5 enables the determination of the guided modes, i.e. the waves that are guided inside the multilayer structure in the y direction. In the DFB laser model presented here, the lowest order waveguided modes represent the laser mode (it overlaps the gain region, propagates in the y direction and interacts with the grating resulting in the feedback required for laser emission).

A wave propagating within the stack of N layers, as depicted in Fig. 2, is confined between the substrate and superstrate layers by total internal reflection. For waveguided fields, $\mathbf{M}$ must relate the field at the boundary between the superstrate and the layer N=1 to the field at the boundary between the T3 layer and the substrate. Therefore the fields at the stack boundaries are required to satisfy Eq. 6, where the subscripts $_{sub}$ and $_{sup}$ represent the substrate and superstrate respectively.

$$\begin{pmatrix} U_{sup} \\ V_{sup} \end{pmatrix} = \mathbf{M} \begin{pmatrix} U_{sub} \\ V_{sub} \end{pmatrix} \tag{6}$$

As the laser modes guided within the DFB laser are bound between the semi-infinite substrate and superstrate layers, the field is evanescent in both the superstrate and the substrate, as shown in Fig. 2. It is this evanescent part of the mode that is used to probe the region close to the laser surface for sensing. The waves are negative-going in the substrate and positive-going in the superstrate (radiation condition) such that $U = U_{sup}e^{(-ik\alpha_{sup}x)}$ and $U = U_{sub}e^{(ik\alpha_{sub}(x-x_{sub}))}$, respectively. For waveguided modes α_{sup} and α_{sub} are imaginary.

Solving Eq. 6 for positive and negative traveling waves results in the modal-dispersion function ($\chi(\beta)$)for bound modes, Eq. 7.

$$\chi(\beta) = \gamma_{sup}m_{11} + \gamma_{sup}\gamma_{sub}m_{12} + m_{21} + \gamma_{sub}m_{22} = 0 \tag{7}$$

Eq. 7 can be solved numerically for β, which is equivalent to the effective refractive index of the laser mode in the case of the DFB laser described in Fig. 2. Each solution of Eq. 7 corresponds to a waveguided mode, with the highest solution representing the lowest order waveguided mode for multilayer DFB lasers.

Once the effective refractive index of the TE_0 mode is found, the field distribution throughout the DFB laser structure and the stack of N layers can be traced. To do this, one of the field amplitudes may be arbitrarily chosen at one point and Eq. 8 can be used to calculate the field amplitudes at other points of the structure relative to the initial chosen amplitude.

$$\begin{pmatrix} U_{n-1} \\ V_{n-1} \end{pmatrix} = \mathbf{M}_n \begin{pmatrix} U_n \\ V_n \end{pmatrix} \tag{8}$$

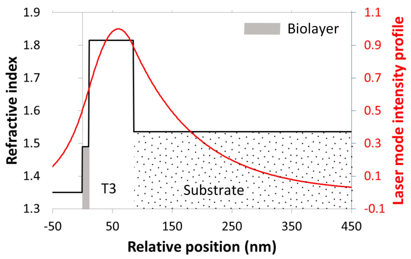

Figure 3. Laser mode intensity profile for a T3 laser with a 10 nm thick biolayer at the surface.

Knowing the amplitudes at each of the layer interfaces, the mode profile, $E(x)$, is calculated through the DFB laser structure and the N layers, where $U(x) = E(x)$, for the TE mode. The resulting mode profile can be plotted against the refractive index of the structure and stack of layers, as shown in the example in Fig. 3, where a T3 DFB laser (n=1.81) is represented with a 10 nm biolayer (n=1.49) on the T3 surface.

The laser mode field intensity is proportional to the square of the field amplitude and the contribution to the field for a particular layer can be found using Eq. 9. Eq. 9 is an example of the calculation of the laser mode intensity overlap (Γ_{bio}) with a biomolecule layer on the laser surface, that extends from x=0 to x=10 nm (for a 10-nm thick layer).

$$\Gamma_{bio} = \frac{\int_0^{10} |E(x)|^2 \, dx}{\int_{-\infty}^{+\infty} |E(x)|^2 \, dx} \tag{9}$$

In this paper, the laser modes are modeled for the DFB laser in response to a number of different scenarios. The shift in laser wavelength due to changes in bulk refractive index are modeled by varying the refractive index of the semi-infinite superstrate layer. For a T3 laser, the semi-infinite substrate layer had a refractive index of approximately 1.52 and a gain layer index of approximately 1.81 (1.64 for BBEHP-PPV) and a thickness approximated by averaging over the grating period to account for the effect of the periodic modulation of the gain layer thickness. When modeling the response of the laser to the adsorption of nanolayers at the DFB laser surface, the index and thickness of the layers were set. For the build-up of polyelectrolyte layers, section IIIB, the refractive index is defined as 1.5 and the layer thickness increased from 1 nm up to a constant thickness of 5 nm for the 6th deposited layer. The superstrate index is defined as the buffer index which was generally 1.35. For modeling the 10 nm biolayer, section IIIB, the index of the layer varied between 1.35 and 1.5, which is the expected index range of biological material [11]. When the response of a dye-doped DFB laser to the adsorption of a 10 nm biolayer was modeled, the gain layer was defined to have an average thickness of 400 nm, index of 1.52 and a semi-infinite substrate of 1.47 [12]. The addition of a high index cladding layer was also modeled for both a dye-doped and a T3 DFB laser, in section IIIC. For these, the TiO_2 index was defined as 2.45 [12] and the thickness was varied from 0 to 60 nm. When modeling the specific detection of avidin with a biotin functionalized laser, section IIID, the following layer parameters were used during modeling: index of 1.46 and a buffer superstrate of 1.35. Specific avidin detection was also modeled for a T3 laser as above but also including a 20 nm TiO_2 layer (index of 2.45).

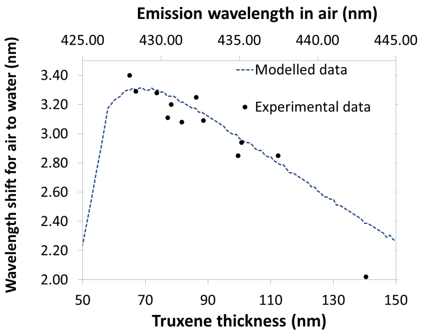

Figure 4. The shift in wavelength and emission wavelength in air for lasers fabricated with a range of T3 thicknesses are plotted. Theoretical thickness, emission wavelength and wavelength shifts are also plotted.

III. Results and discussion

A. Laser characteristics

Fig. 1 provides an example of laser emission from a T3 DFB laser exposed to air; T3 lasers typically have an emission wavelength of around 430 nm and the linewidth is below the resolution of the spectrometer (0.13 nm). The central wavelength and linewidth were determined from a Gaussian fit to the data. The inset in Fig. 1 shows the laser threshold for a laser exposed to air, which is currently 2.5 nJ (fluence of 60 μJ/cm^2). The laser threshold decreases for increasing superstrate refractive index and is approximately half of the value stated when immersed in water. This decrease can be attributed to the increased superstrate index drawing the electric field closer to the device surface, resulting in a greater overlap with the gain region (overlap of 31% in water compared to 23% in air) and therefore a higher modal gain. Our DFB lasers remain operational for >15 minutes at pump energies several times that of the threshold value [13] and the emission wavelength has been shown to remain stable over the laser lifetime [4].

B. Bulk sensing and nanolayer detection - model validation

As mentioned previously, the thickness of the region between the laser substrate and superstrate influences the effective refractive index of the laser and, subsequently, the laser wavelength and sensitivity. Sensitivity can be defined as the shift in wavelength ($\Delta\lambda$) per refractive index change (Δn) for bulk refractive index sensing. Therefore, it is necessary to optimize the thickness of the gain layer in order to achieve the maximum shift in wavelength for changes to the superstrate index. A minimum gain layer thickness (expected to be in the region of 60-80 nm for a T3 DFB laser) is required in order to support the laser mode but beyond this minimum 'cut-off' thickness, a thinner gain layer results in a greater shift in emission wavelength per refractive index unit (RIU) change to the superstrate refractive index. Device sensitivity was investigated by performing bulk sensing measurements with T3 lasers with a range of gain layer thicknesses (≈65-140 nm). For bulk sensitivity measurements, lasers were immersed in de-ionised (DI) water (n=≈1.34 at 430 nm). The laser wavelengths in air and the shift in wavelength upon immersion in DI water for each of the lasers are shown in Fig. 4.

The shift in wavelength versus T3 thickness/emission wavelength in air was modeled and is also plotted in Fig. 4. The experimental data reveals that the largest shift in wavelength upon exposure of the laser to DI water occurred for the lasers with the shortest emission wavelengths, which corresponds to lasers with a thinner T3 layer. Incidentally, our model predicts that the largest overlap of the TE_0 mode with the superstrate occurs for a gain layer thickness of 76 nm (13.2 % when the superstrate is water), resulting in the maximum shift in wavelength observed for a T3 layer of this thickness. The theoretical wavelength versus shift in wavelength plot replicated the experimental data. The model predicts a maximum shift of 3.25 nm for a refractive index change corresponding to the air to water transition, as shown in the plateau region of the plot in Fig. 4. And the model predicts that this maximum response to refractive index changes occurs for a T3 layer thickness of 65 - 75 nm. The drop-off in wavelength shift for a gain layer thickness below 60 nm is due to the fact that a minimum gain layer thickness is required in order to support the guided modes, as mentioned previously. The T3 layer thickness was measured using atomic force microscopy; when T3 is spin-coated at a speed of 3.2 krpm the mean thickness of the T3 layer deposited onto a glass cover-slip was 71±9 nm. We expect that the thickness of this layer may differ slightly with the T3 spin-coated onto the epoxy substrate as opposed to glass, but as the mean wavelength shift of lasers fabricated at a speed of 3.2 krpm has been measured to be 3.33±0.07 nm upon immersion in DI water, we are confident that the average T3 layer thickness is within the maximum plateau region predicted by the model. The good agreement between the experimental and theoretical results indicates that the model can be used to replicate experimental results and investigate design changes to the DFB laser structure for sensitivity optimization.

Further testing of the model was performed by comparing modeled and experimental bulk solutions with varying refractive indices and surface sensing, via adsorption of an analyte. The wavelength shift for changing superstrate index was measured by immersing the laser in solutions with a range of refractive indices, shown in Fig. 5. Data is presented for T3 and BBEHP-PPV lasers to demonstrate the effect of the gain layer index on sensitivity. For both T3 and BBEHP-PPV lasers, the redshift in wavelength across all solutions is approximately linear and corresponds to a bulk refractive index sensitivity of 23 nm/RIU and 21 nm/RIU respectively. The modeled wavelength shifts for increasing refractive index are also shown in Fig. 5a and b. The model overestimates the bulk sensitivity slightly relative to the experimental data. This is most likely down to small variations between the actual solution refractive index and the stated values which are estimates adjusted to take into account the laser emission wavelength (430 nm for a T3 laser, 540 nm for BBEHP-PPV laser). Whilst the bulk sensitivity of our T3 laser currently falls short of that reported for optimized dye-doped DFB lasers (≈100 nm/RIU) [14], the improvement for these lasers can be attributed to two structural features. The first being that dye-doped lasers for biosensing applications tend to operate at longer wavelengths and therefore have a higher grating period value, resulting in a greater wavelength shift for bulk superstrate index changes. The second, and more significant, design feature is the inclusion of a high index TiO_2 cladding layer deposited on top of the gain layer during fabrication [14]. This additional layer compensates for the relatively low index contrast between the dye-doped material and the superstrate; without this additional layer the bulk sensitivity for a dye-doped laser has been reported as 17 nm/RIU [9]. A fairer comparison between the dye-doped and organic semiconductor lasers is to take the ratio of the shift in wavelength ($\Delta\lambda$) per RIU to the emission wavelength (λ). The ratio is 3.4% for a dye-doped laser, 3.9% for BBEHP-PPV and 5.1% for a T3 laser, indicating the improved sensitivity as the gain layer index increases. The inclusion of a TiO_2 cladding layer results in an additional step and added complexity to the laser fabrication process which offsets one of the advantages of DFB lasers, namely ease of fabrication through solution processing. However, this downside may be justified by the improved sensitivity for biomarker detection. The implications of adding a TiO_2 layer are discussed in more detail in section IIIC where we also demonstrate the potential improvement in sensitivity for a T3 laser with a TiO_2 cladding layer. The refractive index range that can be measured with a DFB laser depends on device parameters. In principle, the laser can measure refractive indices from that of vacuum up to the value of the gain material. As expected, the closer you get to the cut-off frequency (i.e. when n_{sup} is equal or above the refractive index of the gain material there are no waveguided modes), the higher the bulk sensitivity as the mode overlap is greater in the superstrate.

Bulk sensitivity is a metric often used to compare the performance of optical sensors and it is a useful means for comparing laser sensors with similar resonant wavelengths. However, it should be kept in mind that in biosensing applications, the analyte binding occurs at the sensors surface therefore, the laser wavelength does not have a significant effect on sensitivity unlike in the case of bulk refractive index sensing [15]. To investigate the surface sensing capability of our laser we employed the layer-by-layer adsorption of cationic Poly (allylamine hydrochloride) (PAH) and anionic Poly (sodium 4-styrenesulfonate) (PSS) nano-layers, results shown in Fig. 5c. For this investigation the T3 DFB laser was immersed in alternating PSS/PAH (5 mg/mL in 0.9 M NaCl, pH 7) solutions for 5 minutes before rinsing with 0.9 M NaCl and recording the emission wavelength attributed to the addition of the PSS/PAH layer. PSS/PAH are known to form self-limiting monolayers; the layers deposited initially are expected to be thinner than subsequent layers, with the layer thickness increasing until a maximum thickness of ≈5 nm is reached around the 6th layer [16]. The PSS/PAH monolayers are expected to have a refractive index of 1.5 at 430 nm. The wavelength shift of the increasing polyelectrolyte stack was also modeled, shown in Fig. 5c, assuming a buffer index of 1.35 and increasing layer thickness up to 5 nm for the first 6 layers and a constant 5 nm layer thickness for all remaining layers. The addition of each nano-layer corresponds to a shift in emission wavelength demonstrating the potential of our DFB laser for surface sensing applications. Surface sensing is demonstrated up to a stack thickness of ≈70 nm and there is the potential to detect additional layers beyond this thickness as the magnitude of the shift in wavelength for the final layer added was 0.18 nm which is well beyond the detection limit of our system (currently 0.06 nm, limited by the resolution of our spectrometer). After the first 6 layers the shift in wavelength is roughly linear up to the 17th layer. The slope of the wavelength shift per nm of adsorbed material is 3.8 % as indicated in the inset in Fig. 5c. This indicates that the DFB laser can detect thicknesses of adsorbed material from the nanometer scale up to several tens of nanometers. A shift of 0.06 nm, the detection limit for our system, corresponds to a nanolayer thickness of <2 nm. A 'size' of 2 nm corresponds to proteins with a molecular weight of ≈5 kDa [17] indicating that our laser has the potential to detect biomarkers of this size, and larger, which includes many relevant biomarkers.

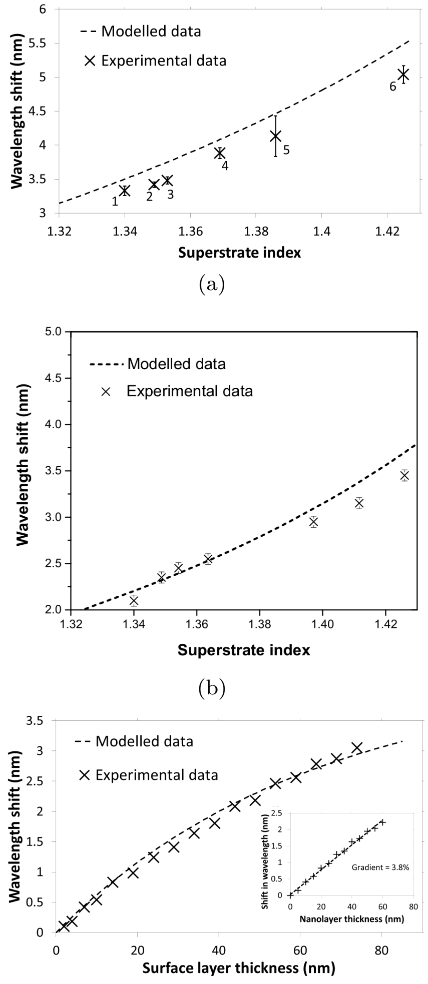

(a)

(b)

(c)

Figure 5. Experimental and modeled data showing the response of the laser to bulk superstrate refractive index changes T3 (a) and BBEHP-PPV (b). And detection of nanometer layers of polyelectrolyte to the sensor surface, experimental and modeled data (c).

As mentioned previously, we hypothesize that a neat, dense OS gain layer with a refractive index higher than that of a dye-doped polymer gain layer has the potential for improved sensitivity. The higher gain layer index will result in greater confinement of the electric field within the gain layer and will also provide a greater overlap with the biomolecule detection region, resulting in improved sensitivity. To test this hypothesis, the response of our laser to the presence of a nano-layer at the sensor surface was modeled for a range of different refractive indices and nano-layer thicknesses. The equivalent modeling was also performed for a typical dye-doped DFB laser with a grating period of 384 nm, substrate index of 1.47, gain layer index of 1.52 and thickness of 400 nm [12]. Biomolecules such as proteins and nucleic acids typically have a refractive index greater than 1.35 and no higher than 1.5 [11] therefore, the response of the lasers to the addition of a nano-layer with an index within this range was investigated, shown in Fig. 6. Fig. 6 demonstrates that for each bio-layer thickness simulated, the shift in wavelength is greater for the T3 laser than the corresponding dye-doped laser by ≈3.5 times.

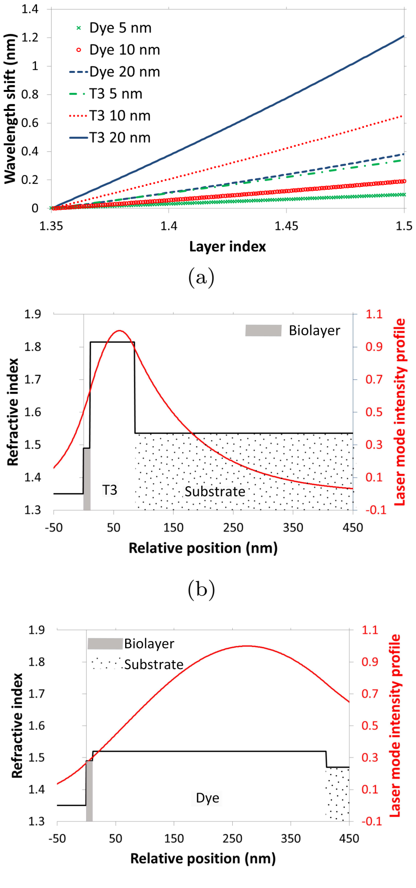

(a)

(b)

(c)

Figure 6. Modeled shift in wavelength for thin biolayer adsorption to T3 and typical dye-doped DFB laser (a). Laser mode intensity profile and device structure for a T3 (b) and a dye-doped laser (c).

The greater wavelength shift is due to the higher index of the OS gain layer. This leads to a greater overlap of the laser mode with the biomolecule detection region for the T3 laser, as shown in Fig. 6b and c. For example, for a 10 nm nanolayer, the T3 laser mode overlap with this nanolayer is 21%. For the dye-doped laser with the same nano-layer the overlap is only 6%. Therefore, the higher index T3 gain layer results in greater interaction of the laser mode with the biomolecule detection region and leads to a larger shift in emission wavelength upon addition of such a nano-layer at the laser surface. For purely solution processed DFB lasers, the use of a neat, high index OS gain material results in improved sensitivity relative to the equivalent dye-doped DFB laser. The improvement in bulk sensitivity for dye-doped DFB lasers upon the addition of a TiO_2 cladding layer is so marked, as mentioned previously, because of the relatively low index contrast between the dye-doped gain layer (n=1.52) and typical biological solutions (n= 1.35 - 1.5). The inclusion of a TiO_2 cladding layer will not result in as large an increase in sensitivity for a T3 layer but is still expected to provide a significant boost to the sensitivity of the T3 DFB laser.

C. Inclusion of a high index cladding layer

A high index TiO_2 cladding layer can be deposited to the surface of the gain material via evaporated ion beam deposition [12] amongst other methods. Whilst this additional fabrication step does lead to a more complex fabrication process, the improvement in surface sensing performance may offset this shortcoming. The effect of adding a TiO_2 cladding layer to the T3 layer was investigated using our model. The shift in wavelength for the addition of a thin (10 nm) bio-layer (n=1.4) in a reference buffer (n=1.35) was modeled for a range of TiO_2 thicknesses, shown in Fig. 7a. The shift in wavelength for the addition of the 10 nm bio-layer, with no TiO_2 cladding layer, corresponds to a shift in wavelength of 0.21 nm for a T3 layer and 0.08 nm for a dye-doped laser. The magnitude of the shift in wavelength increases up to a maximum of 0.49 nm for a TiO_2 thickness of 34 nm and 0.64 nm for a TiO_2 thickness of 40 nm for a T3 and dye-doped laser respectively. Up to a TiO_2 thickness of 20 nm, the surface sensing response of the T3 laser is greater than that of the dye-doped laser. This is due to the increased overlap of the resonating mode with the biomolecule detection region, as shown in Fig. 7b. Although the overlap of the laser mode within the biolayer remains higher for a T3 laser than that of the dye-doped laser up to a TiO_2 thickness of 60 nm, the influence of the total structure effective refractive index results in this increased overlap translating to an improved sensitivity, relative to that of the dye-doped laser, only up to a TiO_2 thickness of 20 nm [12]. A thin layer of TiO_2 may be preferable for a number of reasons. Device cost is one consideration, with lower cost being associated with a thinner TiO_2 layer but more importantly, a thicker TiO_2 layer may increase lasing threshold . The lasing threshold is dependent on the overlap of the laser mode with the gain layer with a greater overlap resulting in a lower lasing threshold. Previous studies of dye-doped DFB lasers reports that the gain layer overlap for TE modes decreases for a TiO_2 thickness greater than 20 nm [12]. Therefore, a TiO_2 thickness <20 nm may be preferable to balance the increase in surface sensing sensitivity without compromising laser threshold.

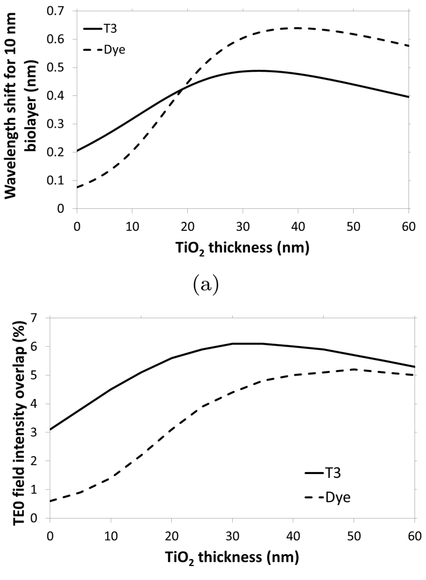

(a)

(b)

Figure 7. Modeled shift in wavelength for adsorption of the 10 nm biolayer to the surface of a T3 and a dye-doped laser for a range of different TiO_2 cladding layer thicknesses (a). And the modeled laser mode profile intensity overlap with a 10 nm biolayer for a T3 and dye-doped laser for a range of TiO_2 thicknesses (b).

D. *Specific biosensing*

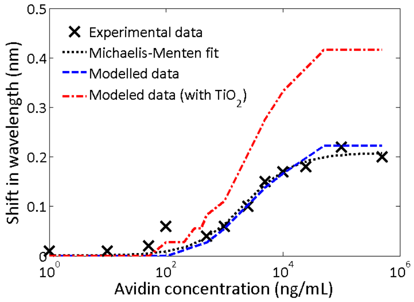

Figure 8. Experimental and modeled data for the specific detection of avidin on a biotin functionalized T3 laser.

For biosensing applications, specific detection of molecules requires functionalization of the laser surface with probes. To demonstrate proof-of-principle specific biosensing, we functionalized the T3 laser surface with biotin for the detection of avidin, shown in Fig. 8. To determine the avidin limit of detection, repeated measurements (4x) of avidin binding (10 μg mL^{-1}) were performed on different lasers. The standard deviation of the wavelength shift attributed to avidin binding of these independent measurements was 0.02 nm. A shift in wavelength is deemed to be 'detectable' if it has a magnitude of three times the standard deviation [18]. Therefore, the minimum level of avidin detection is defined as the avidin concentration resulting in a shift in wavelength $\geq$0.06 nm. The limit of detection corresponded to an avidin concentration of $\approx$1 μg/mL, which is expected to represent a sparse layer of avidin based on the size of avidin (molecular weight of 67 kDa [19]) and the size of the shift expected, as discussed previously. Saturation of all of the biotin binding sites occurs for a concentration around 100 μg/mL, as shown by the plateau in wavelength shift values. Experimental data was fitted to the Michaelis-Menten equation, which can be used to describe molecular binding kinetics [20]. Our multilayer slab waveguide was also modified to take into account the change in refractive index of the avidin biolayer deposited for each concentration. In brief, the deposited avidin molecule/buffer layer volume fraction was assumed to follow a Langmuir relationship and the refractive index was estimated by minimizing the effective medium approximation, shown in Eq. 10, where p represents the fraction of bound target biomolecules and is unity when the biolayer consists only of biomolecules and n_1 and n_2 are the refractive indices of the buffer and avidin molecules [21].

$$(1-p).\frac{n_1-1}{n_1+2}+p.\frac{n_2-1}{n_2+2}=0 \qquad (10)$$

The modeled data closely follows the Michaelis-Menten fit and estimates an avidin limit of detection of $\approx$1 μg/mL. In order to demonstrate the improvement in avidin detection with the presence of a TiO_2 layer, the response to avidin detection was modeled in the presence of a 20 nm TiO_2 layer, shown in Fig. 8. Here the limit of detection reduced by two thirds to around 300 ng/mL. It should be noted that at this stage there was no attempt to optimize the binding kinetics of the biotin and avidin interaction. Optimization of factors such as the buffer and pH may influence the limit of detection and may be investigated in future.

IV. CONCLUSION

In conclusion, we hypothesized that a DFB laser sensor with a neat OS gain layer would enable higher surface sensing sensitivity relative to a DFB laser with a lower index dye-doped gain layer. We have demonstrated optimization of the gain layer thickness for our T3 laser to maximize sensitivity and the agreement between our multilayer model with experimental sensing results. The bulk sensing results for a T3 DFB laser were compared to those of a DFB laser with a conjugated polymer of lower refractive index. The ratio of the shift in wavelength per RIU to the emission wavelength was 3.9% for a BBEHP-PPV DFB laser and 5.1% for the equivalent T3 laser, indicating improved sensitivity for the higher index T3 laser. We also showed that the overlap of the laser mode with the biomolecule detection region is greater for a T3 laser than for a dye-doped laser, resulting in improved sensitivity for surface sensing. Furthermore, modeled results suggest the addition of a thin, high index cladding material, such as TiO_2, to the T3 surface results in an increased sensitivity for surface sensing relative to that of a dye-doped laser, up to a TiO_2 thickness of 20 nm.

Acknowledgements

The authors gratefully acknowledge financial support by the EPSRC (EP/J021962/1 and EP/I029141/1) and Dr A. Kanibolotsky and Prof P. Skabara for supplying materials. The data presented in this paper can be accessed at www.xxxxxxxxxxxxxxxxxxxxxxxxxx.

References

[1] M. R. Trusheim, E. R. Berndt, and F. L. Douglas, "Stratified medicine: strategic and economic implications of combining drugs and clinical biomarkers." *Nature Reviews Drug Discovery*, vol. 6, no. 4, 2007.

[2] M. Kristensen, A. Krüger, N. Groothoff, J. García-Rupérez, V. Toccafondo, J. García-Castelló, M. J. B. nuls, S. Peransi-Llopis, and A. Maquieira, "Photonic crystal biosensor chip for label-free detection of bacteria," in *Optical Sensors*. Optical Society of America, 2011, p. SWB1.

[3] M. Lu, S. S. Choi, C. J. Wagner, J. G. Eden, and B. T. Cunningham, "Label free biosensor incorporating a replica-molded, vertically emitting distributed feedback laser," *Applied Physics Letters*, vol. 92, no. 26, p. 261502, 2008.

[4] A.-M. Haughey, B. Guilhabert, A. Kanibolotsky, P. Skabara, G. Bey, M. Dawson, and N. Laurand, "An organic semiconductor laser based on star-shaped truxene-core oligomers for refractive index sensing," *Sensors and Actuators B: Chemical*, vol. 185, no. 0, pp. 132 – 139, 2013.

[5] Y. Yang, G. A. Turnbull, and I. D. W. Samuel, "Hybrid optoelectronics: A polymer laser pumped by a nitride light-emitting diode," *Applied Physics Letters*, vol. 92, no. 16, p. 163306, 2008.

[6] T. Riedl, T. Rabe, H.-H. Johannes, W. Kowalsky, J. Wang, T. Weimann, P. Hinze, B. Nehls, T. Farrell, and U. Scherf, "Tunable organic thin-film laser pumped by an inorganic violet diode laser," *Applied Physics Letters*, vol. 88, no. 24, pp. 241 116 –241 116–3, 2006.

[7] A. L. Kanibolotsky, R. Berridge, P. J. Skabara, I. F. Perepichka, D. D. C. Bradley, and M. Koeberg, "Synthesis and properties of monodisperse oligofluorene-functionalized truxenes - highly fluorescent star-shaped architectures," *Journal of the American Chemical Society*, vol. 126, no. 42, pp. 13 695–13 702, 2004, pMID: 15493927.

[8] R. A, Z. Z, M. CF, S. TM, and B. V, "Sensitivity gains in chemosensing by lasing action in organic polymers," *Nature*, vol. 434, pp. 876–879, 2005.

[9] M. Lu, S. S. Choi, U. Irfan, and B. T. Cunningham, "Plastic distributed feedback laser biosensor," *Applied Physics Letters*, vol. 93, no. 11, pp. 111 113 –111 113–3, 2008.

[10] J. Chilwell and I. Hodgkinson, "Thin-films field-transfer matrix theory of planar multilayer waveguides and reflection from prism-loaded waveguides," *J. Opt. Soc. Am. A*, vol. 1, no. 7, pp. 742–753, 1984.

[11] J. Voros, "The density and refractive index of adsorbing protein layers," *Biophysical Journal*, vol. 87, no. 1, pp. 553 – 561, 2004.

[12] C. Vannahme, C. L. C. Smith, M. BrÃ¸kner Christiansen, and A. Kristensen, "Emission wavelength of multilayer distributed feedback dye lasers," *Applied Physics Letters*, vol. 101, no. 15, 2012.

[13] C. Foucher, B. Guilhabert, A. L. Kanibolotsky, P. J. Skabara, N. Laurand, and M. D. Dawson, "Highly-photostable and mechanically flexible all-organic semiconductor lasers," *Opt. Mater. Express*, vol. 3, no. 5, pp. 584–597, May 2013.

[14] Y. Tan, C. Ge, A. Chu, M. Lu, W. Goldshlag, C. S. Huang, A. Pokhriyal, S. George, and B. Cunningham, "Plastic-based distributed feedback laser biosensors in microplate format," *Sensors Journal, IEEE*, vol. 12, no. 5, pp. 1174 –1180, 2012.

[15] I. D. Block, N. Ganesh, M. Lu, and B. Cunningham, "A sensitivity model for predicting photonic crystal biosensor performance," *Sensors Journal, IEEE*, vol. 8, no. 3, pp. 274–280, 2008.

[16] G. Ladam, P. Schaad, J. C. Voegel, P. Schaaf, G. Decher, and F. Cuisinier, "In situ determination of the structural properties of initially deposited polyelectrolyte multilayers," *Langmuir*, vol. 16, no. 3, pp. 1249–1255, 2000.

[17] H. P. Erickson, "Size and shape of protein molecules at the nanometer level determined by sedimentation, gel filtration, and electron microscopy," *Biological Procedures Online*, vol. 11, 2009.

[18] B. Cunningham, "Label-free optical biosensors: An introduction," M. Cooper, Ed. Cambridge University Press, 2009, pp. 1–28.

[19] E. P. Diamandis and R. C. Morton, "Time-resolved fluorescence using a europium chelate of 4,7-bis-(chlorosulfopheny1)-1,10-phenanthroline-2,9-dicarboxylic acid (bcpda): Labeling procedures and applications in immunoassays," *Journal of Immunological Methods*, vol. 112, no. 1, pp. 43 – 52, 1988.

[20] A. D. Attie and R. T. Raines, *J. Chem. Educ.*, vol. 72, no. 2, p. 119, 1995.

[21] M. Erol, H. Du, and S. Sukhishvili, "Control of specific attachment of proteins by adsorption of polymer layers," *Langmuir*, vol. 22, no. 26, pp. 11 329–11 336, 2006, pMID: 17154622.

AM. Haughey received a M.Phys degree in 2007, M.DSc in 2010 and Eng.D in 2014. She currently works as a researcher at the Fraunhofer Centre for Applied Photonics.

G. McConnell received a M.Eng degree in 2013. He is currently working towards an Eng.D with the Institute of Photonics (IOP).

B. Guilhabert received the Engineering degree in 2003, D.E.A. degree in 2004 and Ph.D in 2008. He is currently a Senior Researcher with the IOP.

G.A. Burley received his B.Sc in 1996 and Ph.D in 2000. Glenn is currently a Senior Lecturer in the Department of Pure and Applied Chemistry at the University of Strathclyde.

M.D. Dawson received the Ph.D 1985. Since 1996 he has been with the IOP where he was promoted to Professor in 2001.

N. Laurand received the Engineering degree in 2000 and Ph.D in 2006. He is currently an Associate Team Leader with the IOP.

LANGMUIR Article
Cite This: Langmuir XXXX, XXX, XXX−XXX
pubs.acs.org/Langmuir

Organic Semiconductor Laser Platform for the Detection of DNA by AgNP Plasmonic Enhancement

G. McConnell,[†,‡] S. Mabbott,[§] A. L. Kanibolotsky,[∥,⊥,∇] P. J. Skabara,[∥,#] D. Graham,[§] G. A. Burley,[§] and N. Laurand[*,†]

[†]Institute of Photonics, Department of Physics, University of Strathclyde, Glasgow G12 8QQ, U.K.
[‡]Biomedical Engineering, University of Strathclyde, Glasgow G12 8QQ, U.K.
[§]WestCHEM, Department of Pure and Applied Chemistry, University of Strathclyde, Glasgow G12 8QQ, U.K.
[∥]WestCHEM, School of Chemistry, University of Glasgow, Glasgow G12 8QQ, U.K.
[⊥]Institute of Physical-Organic and Coal Chemistry, The National Academy of Sciences of Ukraine, 02160 Kyiv, Ukraine

Supporting Information

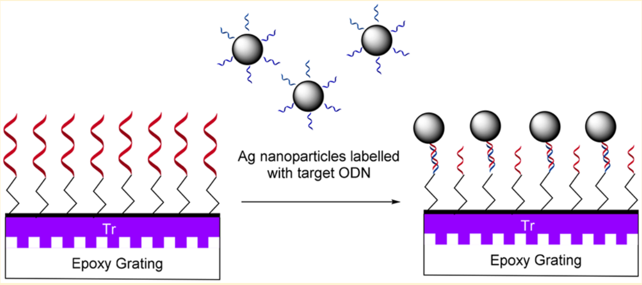

ABSTRACT: Organic semiconductor lasers are a sensitive biosensing platform that respond to specific biomolecule binding events. So far, such biosensors have utilized protein-based interactions for surface functionalization but a nucleic acid−based strategy would considerably widen their utility as a general biodiagnostic platform. This manuscript reports two important advances for DNA-based sensing using an organic semiconductor (OS) distributed feedback (DFB) laser. First, the immobilization of alkyne-tagged 12/18-mer oligodeoxyribonucleotide (ODN) probes by Cu-catalyzed azide alkyne cycloaddition (CuAAC) or "click-chemistry" onto an 80 nm thick OS laser film modified with an azide-presenting polyelectrolyte monolayer is presented. Second, sequence-selective binding to these immobilized probes with complementary ODN-functionalized silver nanoparticles, is detected. As binding occurs, the nanoparticles increase the optical losses of the laser mode through plasmonic scattering and absorption, and this causes a rise in the threshold pump energy required for laser action that is proportional to the analyte concentration. By monitoring this threshold, detection of the complementary ODN target down to 11.5 pM is achieved. This complementary binding on the laser surface is independently confirmed through surface-enhanced Raman spectroscopy (SERS).

INTRODUCTION

A range of biological materials such as circulating microRNA,[1−4] DNA,[5−7] and proteins,[8−11] which are found in the blood, plasma, or other biological fluids, can be used as biomarkers for patient diagnosis, identifying disease pathologies and risk groups.[12,13] While standard biomarker detection is carried out in centralized laboratories, approaches to medicine for early disease prevention,[14] triaging, and chronic disease management[15] necessitate the development of point-of-care diagnostic technologies to provide rapid results in nonlaboratory settings.[16,17] There are several promising optical technologies for this need in point-of-care diagnostics,[18−21] some of them combining evanescent sensing platforms with antibody protein or nucleic acid (DNA sensing) biorecognition approaches. The current technologies are subject to limitations, discussed here in more detail, which the new paradigm presented in this text hopes to address.

Most evanescent wave sensors are based on passive, optically resonant structures such as dielectric microresonators,[21−23] photonic crystals,[24−26] or surface plasmon resonators.[27,28] However, they necessitate precise injection of an external light source to the resonator, which complicates their miniaturization and further leads to a trade-off between sensitivity and detection resolution.[29] Organic distributed feedback (DFB) laser sensors offer a viable alternative to these passive evanescent wave devices. They mitigate the sensitivity/resolution trade-off issue, and their facile implementation is attractive for miniaturization.[29−32] Organic DFB laser sensors are fabricated by imprinting a nanofilm of lasing material with a Bragg grating structure. Their emission properties are responsive to changes in the refractive index at the surface of the nanofilm.[19,32] The laser material is either a transparent polymeric matrix doped with dyes[33−36] or an organic semiconductor (OS) as we previously reported.[37−39]

Biosensing with organic DFB lasers has so far exclusively relied on antibodies or antigens for biomarker capture and on measuring the shift of the laser wavelength for transduction. Demonstrating a nucleic acid strategy for biomarker capture is

Special Issue: Nucleic Acids Nanoscience at Interfaces

Received: April 22, 2018
Revised: September 15, 2018
Published: September 18, 2018

DOI: 10.1021/acs.langmuir.8b01313
Langmuir XXXX, XXX, XXX−XXX

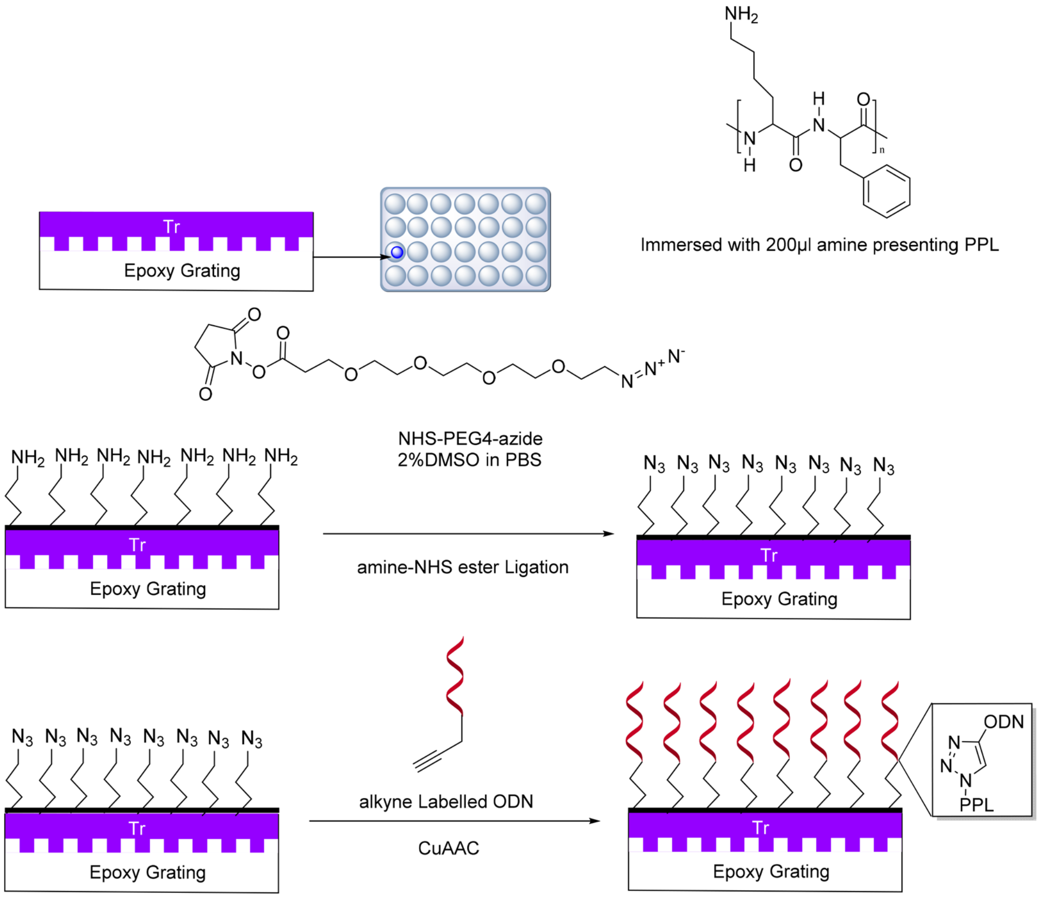

Figure 1. Stepwise functionalization of an organic DFB laser with ODN probes for the capture of matching ODN sequences (not to scale).

of interest because DNA probes are more robust, less costly to produce and they can be flexibly designed to target particular biomarkers and tailored for reuse.[40,41] Furthermore, devices have been shown to specifically detect IgG with a limit of detection (LOD) of 60 ng/mL,[42] TNF-α at a LOD of 0.625 μg/mL,[43] and ErbB2 protein biomarkers at a LOD of 14 ng/mL.[32] While these are within the diagnostic ranges of a few medically relevant biomarkers, such LODs are still too large for many disease biomarkers where a LOD in the range of pg/mL or pM is often needed.[44] Therefore, there is a distinct need to lower the LOD, which can be achieved using plasmonic nanoparticles to amplify the change in complex refractive index upon biomarker binding to the laser surface and monitoring laser characteristics other than the wavelength.

We describe herein the preparation of an OS DFB laser functionalized with 12/18-mer oligodeoxyribonucleotides (ODNs). Using the Cu-catalyzed alkyne−azide cycloaddition (CuAAC) reaction or “click-chemistry”, DNA immobilization[45−48] is achieved by the formation of a 1,4-triazole on the surface by the reaction of a 5′-modified ODN sequence with an azide-modified OS surface. This enables the detection of the sequence-selective binding of silver nanoparticle (AgNP) functionalized with complementary ODN sequences. AgNPs allow confirmation of surface immobilization through SERS measurements,[49] but they also significantly increase, via localized surface plasmons, the effect on the laser characteristics. In this paper, we demonstrate sequence-selective detection of ODN analytes using a hybrid DNA/organic laser in conjunction with SERS active AgNPs, which is a recent evanescent sensor platform.

■ EXPERIMENTAL METHODS

DFB Laser Fabrication. The DFB lasers are made of a thin layer of gain material deposited on top of an epoxy grating. The grating enables feedback for laser oscillation but also provides outcoupling of the emission perpendicular to the gain material film for a vertical emission. Epoxy gratings, with a periodicity of Λ = 276 nm and a 5 mm by 5 mm surface area,[37] were fabricated by imprinting a Norland NOA65 epoxy, dropped onto an acetate mount, with a silica master grating (made by e-beam lithography) and UV curing it for 50 s under a UV lamp for a dosage of 300 J·cm^{-2} and further postcuring for 1 h to stabilize the structure after removal from the master grating. Vertically emitting DFB lasers were then obtained by forming a ≈80 nm thick nanofilm of neat T3 oligofluorene−truxene star-shaped macromolecules, consisting of truxene core and three terfluorene arms[50−52] (Tr), onto an epoxy grating. The film was deposited by spin-coating 15 mL of a 20 mg·mL^{-1} Tr in toluene solution onto an acetate mounted grating taped to a glass support at 3.2 krpm. The DFB lasers were transferred and taped into the bottom of a well in a well plate as schematized in Figure 1. This arrangement enabled easy immersion of the lasers for the different steps of surface functionalization, biohybridization, and characterization, as detailed below.

Surface Functionalization/Probe Immobilization. Azide-modified laser surfaces were prepared by exposing the amine presenting poly(phenyl-lysine) (PPL) monolayer coated OS surface to a 200 μL droplet of a 2 mg·mL^{-1} azido-PEG$_4$-NHS ester (Figure 1) solution for 15 min. This enables subsequent “click” immobilization of alkyne labeled ODNs.

For this, the OS laser surface is first washed with a 10 mM phosphate buffer solution (PBS). The laser is then coated with PPL (a polyelectrolyte containing lysine with amine ligation sites) by immersion for 10 min in PPL suspended in PBS. The laser surface

DOI: 10.1021/acs.langmuir.8b01313
Langmuir XXXX, XXX, XXX−XXX

is washed with PBS again to remove any loose material before azide modification of the adsorbed PPL layer.

For the probes, ODN sequences (ODN$_{xp}$, where x = 1, 2, or 3, corresponds to different sequences as identified in Figure 2) were purchased with an alkyne group at the 5′ end to enable click immobilization on the azide presenting laser surface. To immobilize these probes on the lasers, 17.5 nmol of an ODN$_{xp}$ in deionized water with copper(II) sulfate, 35 nmol of sodium ascorbate, and 35 nmol of THPTA were incubated for 30 min. The surface was then washed with PBS.

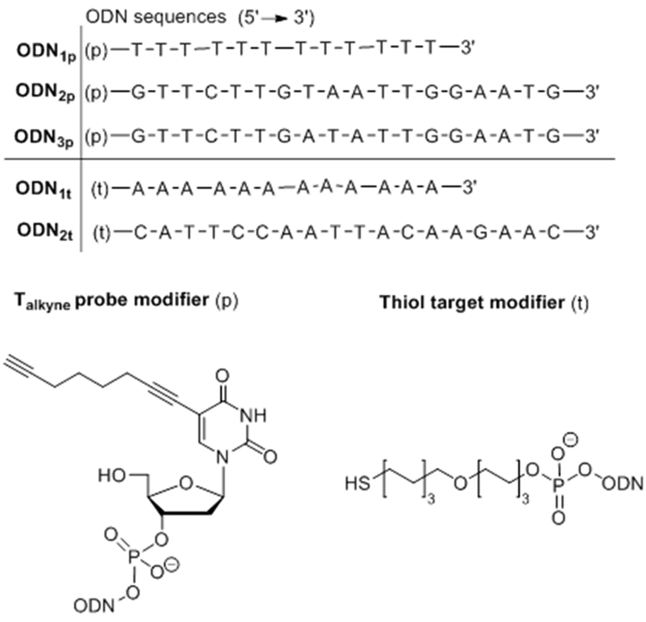

Figure 2. ODN probe/target sequences shown with (t) thiol modification for NP labeling and (p) alkyne modification for click-chemistry.

Biohybridization for Target Detection. For the targets, ODN sequences (ODN$_{yt}$, where y = 1 or 2, corresponds to two different sequences; see Figure 2) were purchased with a terminal thiol at the 5′ end. These were used to functionalize AgNPs[49] (approximately 40−45 nm in diameter) labeled with malachite green isothiocyanate (MGITC) dye that was used for SERS detection. DNA/MGITC:NP ratios of 5000:1 in excess were used for AgNP functionalization.[53] ODN$_{1t}$, a 12-mer consisting solely of adenines was matched to the probe ODN$_{1p}$, a 12-mer of the base thymine; these were used in initial experiments to confirm the anchoring of the ODN probes via click-chemistry. ODN$_{2t}$ is the complementary 18-mer to the mixed sequence probe ODN$_{2p}$. ODN$_{3p}$ is mismatched to ODN$_{2t}$ with bases 8 and 9 reversed from ODN$_{2p}$. These 18-mer ODNs were used in experiments to assess the specificity of the ODN target/analyte hybridization at the functionalized DFB surface.

For ODN analyte detection, the ODN$_{xp}$-functionalized DFB lasers were incubated with target ODN$_{yt}$ bound AgNPs in solution (PBS with 0.3 M NaCl) for 30 min (10 min for threshold comparison).

Surface-Enhanced Raman Spectroscopy 2D Mapping. Mapping was carried out using a Raman microscope (Gloucestershire, U.K.) equipped with an excitation wavelength of 514.5 nm. Light was focused on the samples using a 20× objective, and the Raman shift was calibrated using a Si standard peak fixed at 520.5 cm^{-1}. Spectra of each sample were collected for 0.5 s in a 680−6080 cm^{-1} spectral range. The SERS peak present close to 1171 cm^{-1} corresponding to the in-plane C−H bending of MGITC was used to track the AgNP distribution across the surface.[49] The SERS data was baseline corrected, and the intensity of the signature of MGITC, indicative of the presence of AgNPs, was used to generate surface maps with 0.01 μm spatial resolution.

Optical Pumping and Laser Characterization. The lasers were fixed in the wells with Kapton tape and optically pumped through the bottom of the well, perpendicular to the plane of the DFB laser surface, so the functionalized surface would not affect the incident pump laser beam. The pump laser emitted 355 nm wavelength pulses of 5 ns duration at a 10 Hz repetition rate. The DFB vertical laser emission was collected from the same side as the pump injection (i.e., from the bottom of the well) using a dichroic filter. It was coupled into a 50 μm core fiber plugged into a CCD spectrometer (Avantes, 0.13 nm resolution) for spectra and intensity acquisition. The ODN-functionalized DFB laser typically emits at 430 nm for a line width below 0.3 nm and has a threshold of 0.06 μJ (±7%) when measured in PBS with a pump spot of ≈140 μm in diameter (using the e^{-2} of the intensity maximum). More details on the PL and amplified spontaneous emission spectra of the Tr gain material can be found in the literature.[38] Figure 3 plots a typical Tr DFB laser emission spectrum in PBS alongside the extinction spectrum of ODN coated AgNPs. The laser transfer function, which is obtained by plotting the integrated spectral intensity of the laser versus the pump energy, was characterized for different target concentrations. This analysis allowed the effect of the AgNP hybridization on the DFB laser performance to be determined. The DFB laser output in the presence of AgNPs is discussed later in the text and Supporting Information. SEM images of DFBs exposed to target AgNPs in solution can be seen in SI1, SEM Imaging.

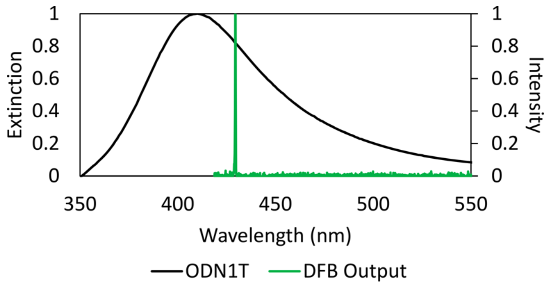

Figure 3. Normalized extinction spectrum for AgNPs coated with ODN targets with overlay of typical DFB laser output in green.

■ RESULTS AND DISCUSSION

Initially, we studied the effectiveness of our laser surface functionalization strategy using the poly-T probes ODN$_{1P}$. We did this by capturing a 2D SERS map of laser devices functionalized with ODN$_{1p}$ probes, different samples prepared with and without an intermediate PPL monolayer, and nonfunctionalized lasers consisting of only the neat Tr OS film.

Figure 4a represents the SERS spectrum of a particular point on the surface of a functionalized DFB laser before and after ODN$_{1t}$ coated AgNPs have hybridized to the ODN$_{1p}$ probes bound to the DFB surface. A 130 × 130 μm^2 2D SERS map is generated by laser excitation of the DFB laser surface under study, and it is utilized in the following to validate the laser surface functionalization and capabilities for complementary strand detection. The peak present at 1615 cm^{-1} and amplified in the samples where MGITC labeled AgNPs have bound to the surface is due to N−Ph ring vibration and C−C stretch; these features can be found in the OS layer, and 1170 cm^{-1} is a signature peak of MGITC. In Figure 4b, as evidenced by the SERS signal intensity shown in the SERS maps, it can clearly be seen that the AgNPs bound with ODN$_{1t}$ have hybridized to the fully functionalized laser (when functionalization includes the PPL layer as described in Experimental Methods) with much greater affinity than any of the other two samples.

DOI: 10.1021/acs.langmuir.8b01313
Langmuir XXXX, XXX, XXX−XXX

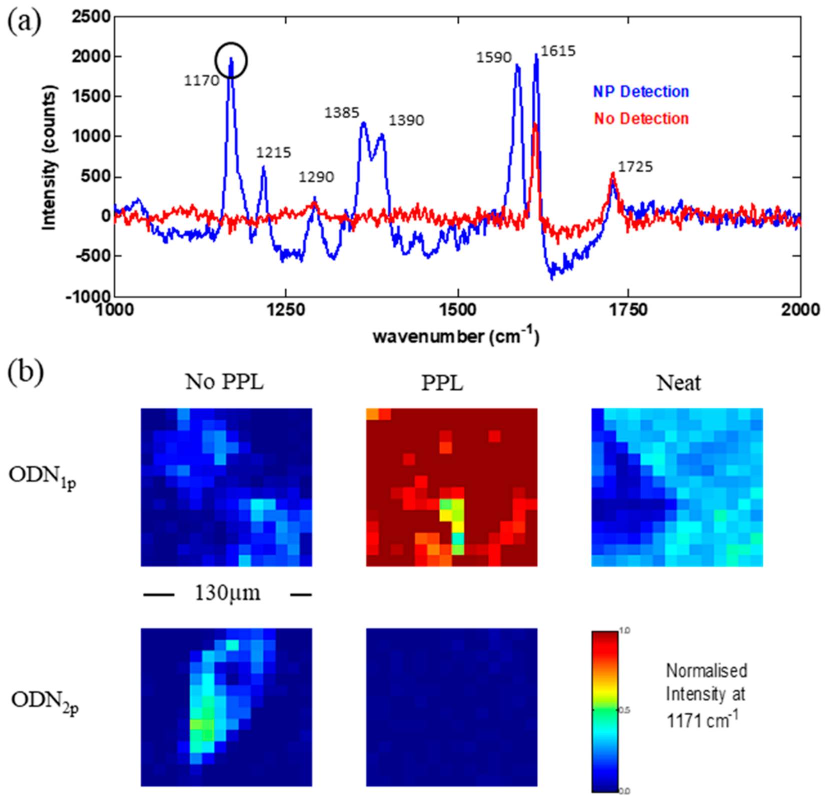

Figure 4. (a) SERS spectra of a DFB laser before (red) and after (blue) ODN_{1t} incubation. (b) SERS mapping of OS-DFB surfaces demonstrating the effects of including a PPL layer on the target bound AgNP hybridization and the specificity of NP absorption. All samples were exposed to ODN_{1t}.

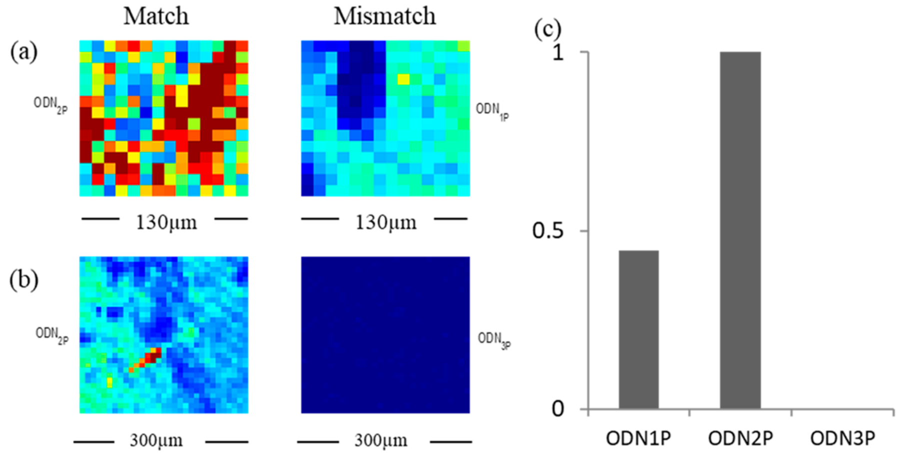

Figure 5. SERS mapping used in specificity testing of samples when exposed to mixed sequence ODN_{2T} comparing samples coated with the targeted probe ODN_{2P} to (a) ODN_{1P}, a poly-A chain, and (b) ODN_{3P}, a chain with nucleotides 8 and 9 reversed. (c) Mean intensity of samples exposed to solution containing ODN_{2T}, which is complementary to ODN_{2P}, normalized to the intensity value of the ODN_{2P} sample.

The neat DFB laser surface displays a higher MGITC signal than the partially functionalized sample; this suggests that some nonspecific adsorption (NSA) of ODN_{1t} coated AgNPs directly onto the Tr film is taking place. We suspect that the ODNs adsorb onto Tr through their hydrophobic bases leaving the hydrophilic backbone facing up. The lower level of NSA on partially functionalized samples (where PPL is omitted) is indicative of ODN probes nonspecifically adsorbed to the Tr film. The adsorbed probes cannot easily react with the targets but are impeding NSA of the latter on the laser surface.

Samples functionalized with ODN_{2p} mixed sequence probes, i.e., mismatched to ODN_{1t}, show a much lower intensity 1171 cm^{-1} signature peak for MGITC in Figure 4b demonstrating specificity in the binding. The ODN_{1t}−ODN_{1p} binding used to assess the CuAAC protocol is useful due to the high binding affinity between poly-A and poly-T ODN sequences. However, in a second set of experiments, to verify the practicality and specificity of this protocol for biosensing, we replaced these with mixed sequence ODNs. ODN_{2t} is a mixed sequence 18-mer ODN while ODN_{2p} and ODN_{3p} are the complementary and mutated sequences (two reversed base sequences),

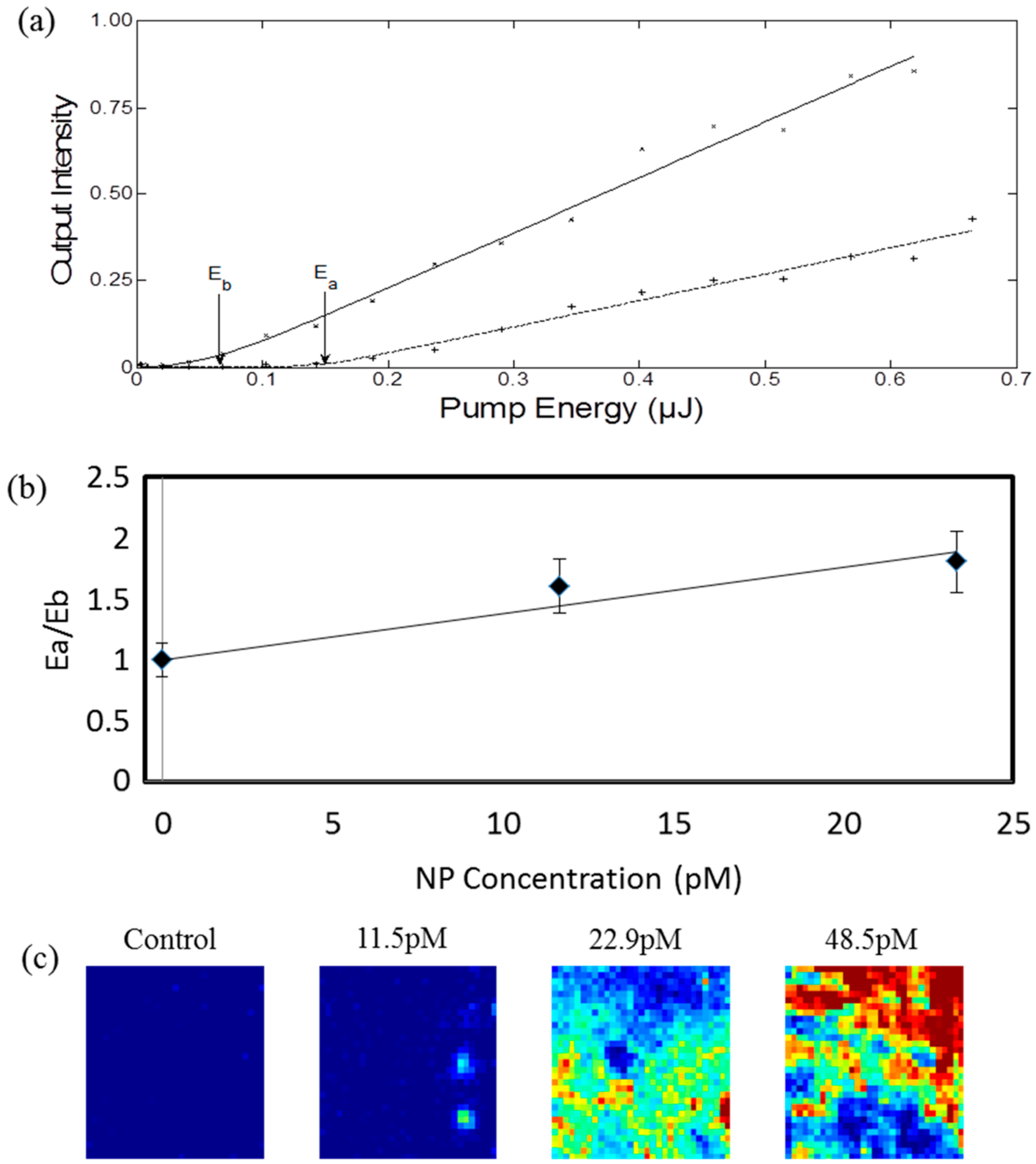

Figure 6. (a) Laser transfer function fitted curves before and after AgNP hybridization. The threshold energy after (E_a) hybridization has increased compared to that before (E_b) hybridization. (b) The ratio between the lasing threshold after (E_a) and before (E_b) incubation of a Tr DFB laser functionalized with ODN_{1p} probes exposed to varying concentrations of ODN_{1t} with a standard deviation of 7% measured in the pump beam. (c) SERS maps of the corresponding laser surfaces.

respectively. The use of 18-mer rather than the 12-mer ODN sequences is also closer to the ≈20-mer ODN sequences usually attributed to micro-RNA.[4]

ODN_{1p}-functionalized, ODN_{2p}-functionalized, and ODN_{3p}-functionalized lasers were exposed to ODN_{2t} labeled AgNPs. Results for both experiments are shown in Figure 5. The ODN_{2p}-functionalized sample demonstrates a far greater binding affinity with the target ODN_{2t} labeled NPs. In fact, the sample with ODN_{3p} probes shows very little binding to the target NPs. In Figure 5b, the sample surface was also mapped over an increased area, 300 × 300 μm^2, to give a more complete picture of the binding homogeneity across the laser surface, but this decreases the accuracy in the presence of localized regions of high intensity as a wider range of values are represented by the same 256 color scale through normalization.

Figure 5c shows the normalized comparison of the average pixel heatmap for surfaces prepared with different ODN probes across the inspected area. As can be seen, the ODN_{3p}-functionalized lasers show almost no binding while the poly-T ODN_{1t} probe does show some signs of AgNP capture; this is thought to be due to a lower specificity exhibited by the mononucleotide as opposed to mixed sequence ODN probes.

After confirmation by SERS of the immobilization of ODN probes and of the specificity of target hybridization, we characterized the effect of such hybridization on the DFB laser output using ODN_{1t} targets and ODN_{1p} surface probes. The AgNPs of bound target ODNs are immobilized at an average distance of 10−15 nm from the laser surface (added length of the PPL layer, the azido-PEG_4-NHS ester, and the ODN probe), and therefore, the laser mode is able to couple to them by evanescence.[37] Because the AgNPs absorb at the laser wavelength (the laser emission is on the red side of the localized plasmon resonance as can be seen in Figure 3), the laser threshold is seen to increase upon target binding (Figure 6a); meanwhile, the output intensity at a given pump level drops (Figure 6a). The presence of AgNPs also leads to a reduction of the slope of the laser transfer function. We surmise that the observed threshold increasing (and slope decreasing) effect of the AgNP on the DFB platform is due to the optical losses following a binding-dependent modal loss caused by immobilization of the target ODNs (see SI2, Nanoparticle Theory). In summary, the modal gain needed for laser oscillation must match the overall losses and therefore the pump intensity at threshold I_{pth} is proportional to these losses,

$$I_{\mathrm{pth}} = \frac{h\nu_{\mathrm{p}}}{\alpha_{\mathrm{p}}}\frac{\alpha + \Gamma_1\alpha_{\mathrm{NP}}}{\Gamma_{\mathrm{a}}\sigma\tau_{32}} \tag{1}$$

where α is the modal loss of the initial laser, α_{NP} is the loss due to bound AgNPs, Γ_1 is a parameter representing the overlap of the laser mode intensity with the AgNPs, α_{p} is the absorption at the pump wavelength, and $h\nu_{\mathrm{p}}$ is the energy of the pump photons. The ratio of the threshold pump energy before, E_{b}, and after, E_{a}, functionalization is then simply

$$\frac{E_{\mathrm{a}}}{E_{\mathrm{b}}} \propto \frac{I_{\mathrm{pth\_a}}}{I_{\mathrm{pth\_b}}} = \Gamma_1\frac{\alpha_{\mathrm{NP}}}{\alpha} + 1 \tag{2}$$

$I_{\mathrm{pth\_b}}$ and $I_{\mathrm{pth\_a}}$ are the pump intensities at threshold before and after functionalization, respectively. At low analyte concentration, α_{NP} is expected to be linear with the concentration x. Under these conditions the laser threshold increases linearly with x as given by (see SI2, Nanoparticle Theory)

$$\frac{E_{\mathrm{a}}}{E_{\mathrm{b}}} = Cx + 1 \tag{3}$$

C is a constant linked to the binding affinity and to α.

The transfer functions for lasers were measured before and after incubation at different analyte concentrations (0, 11.5, 23, and 48.5 pM). Figure 6a shows the example of the laser transfer functions before and after incubation with 23 pM. The thresholds E_{b} and E_{a}, identified by arrows, were calculated from energy readings taken at the same pump spot; the pump laser was blocked during incubation periods and between readings. While we focus here on laser intensity measurements and threshold, we note that no significant changes to the central emission wavelength (see SI3, NP Spectral Effects) of the laser upon target binding were detected (within a ±0.13 nm resolution); minor changes in wavelength and line width were accounted for during threshold calculations fitting the DFB laser output with a Gaussian curve.[54] The ratio $\frac{E_{\mathrm{a}}}{E_{\mathrm{b}}}$, which increases with the concentration, is plotted in Figure 6b along with the linear fit using eq 3 with $C = 0.039\ \mathrm{pM}^{-1}$. The LOD by threshold monitoring is 11.5 pM by observation; a lower limit may be obtained by increasing the resolution of AgNP concentrations that are tested. Altering the incubation time could be attempted to lower the LOD, as a longer incubation time might allow more hybridization to occur. Bringing the laser emission in alignment with the NP resonance would increase absorption and therefore should lower the LOD as well. At a concentration of 48.5 pM, the E_{a} value was unobtainable as the laser could not reach the threshold. The reason for this is that for a given DFB laser structure (i.e., a given Tr thickness), the modal gain has a maximum, called the saturated gain, which cannot be exceeded. Once the modal gain is saturated, increasing the pump energy does not increase the gain as the population of Tr molecules is fully inverted. If the added loss due to analyte hybridization makes the gain at a threshold higher than this saturated gain, then laser oscillation cannot be obtained. This effect limits the dynamic range of sensing by laser threshold monitoring. The dynamic range could be increased, however, by increasing the thickness of the Tr film, which would raise the saturated gain value.

Figure 6c shows the corresponding SERS map of the laser surface after incubation, clearly confirming the increased bound analytes for increasing concentration.

■ CONCLUSION

Our approach demonstrates the feasibility of DNA-based sensing with an organic semiconductor DFB laser. A successful, effective immobilization strategy for ODN probes on an OS surface has been identified. With silver NP-functionalized analytes, the laser threshold has been shown to respond to binding events for concentration at and above 11.5 pM; alterations to incubation time could lower this. With the use of OSs with different emission frequencies and NPs with different absorption spectra and by tuning the gain material thickness, it is expected that the sensitivity and dynamic range could be tailored for specific applications. Not only have we confirmed a polyelectrolyte-anchored, click-chemistry protocol as a viable method of DFB laser surface functionalization, but also we have demonstrated the capture of matching ODN sequences and the specificity of the protocol. With the current trends toward ODN Aptamer probes[55−57] in biosensing and the reduced complexity in comparison to traditional antibody-based sensing protocols, the novel ODN approach outlined here demonstrated with OS DFB lasers is an important stepping stone to specific, low cost optical biosensing applications.

■ ASSOCIATED CONTENT

Ⓢ Supporting Information

The Supporting Information is available free of charge on the ACS Publications website at DOI: 10.1021/acs.langmuir.8b01313.

SI1, SEM Imaging, SEM images of the surface of a DFB laser with and without probe functionalization after exposure to target bound AgNPs in solution; SI2, Nanoparticle Theory, nanoparticle effect on laser mode with equations/theory (PDF)

SI3, NP Spectral Effects: 0 pM DFB spectra and 22.9 pM DFB spectra (before/after) (PDF)

■ AUTHOR INFORMATION

Corresponding Author

*E-mail: nicolas.laurand@strath.ac.uk.

ORCID

G. McConnell: 0000-0001-8764-6127
G. A. Burley: 0000-0002-4896-113X

Present Addresses

[#]P. J. Skabara is now at the University of Glasgow School of Chemistry.
[∇]A. L. Kanibolotsky is at the University of Glasgow School of Chemistry, being on leave from The National Academy of Sciences of Ukraine.

Notes

The authors declare no competing financial interest.

All data underpinning this publication are openly available from the University of Strathclyde KnowledgeBase at http://dx.doi.org/10.15129/1316da75-360d-4cf7-b9e3-57d0b18d2190.

■ ACKNOWLEDGMENTS

This work was supported and funded by the Medical Devices CDT of Strathclyde University EPSRC grant number EP/F50036X/1. A.L.K. thanks the EPSRC for funding (EP/N009908/1). P.J.S. thanks the Royal Society for a Wolfson Research Merit Award.

■ REFERENCES

(1) Yuan, L. Q.; de Jesus Perez, V.; Liao, X. B.; Krol, M.; Yeh, C. H. MicroRNA and Cardiovascular Disease 2016. *BioMed Res. Int.* **2017**, *2017*, 3780513.

(2) Naga Prasad, S. V.; Gupta, M. K.; Duan, Z. H.; Surampudi, V. S.; Liu, C. G.; Kotwal, A.; Moravec, C. S.; Starling, R. C.; Perez, D. M.; Sen, S.; Wu, Q.; Plow, E. F.; Karnik, S. A unique microRNA profile in end-stage heart failure indicates alterations in specific cardiovascular signaling networks. *PLoS One* **2017**, *12* (3), e0170456.

(3) Cordes, K. R.; Srivastava, D. MicroRNA regulation of cardiovascular development. *Circ. Res.* **2009**, *104* (6), 724−732.

(4) Zhang, X. B.; Chen, B. S. Perspective of microRNA in cardiovascular-associated diseases. *Zhonghua Xin Xue Guan Bing Za Zhi* **2008**, *36* (7), 661−663.

(5) Justino, A.; Dias, P.; Pina, M. J.; Sousa, S.; Cirnes, L.; Sousa, A. B.; Machado, J. C.; Costa, J. L. Comprehensive massive parallel DNA sequencing strategy for the genetic diagnosis of the neuro-cardio-facio-cutaneous syndromes. *Eur. J. Hum. Genet.* **2015**, *23* (3), 347−353.

(6) Song, H.; Nan, Y.; Cheng, X. W. Circulating cf-DNA: a promising, noninvasive tool for assessment of early cardio-metabolic risk. *Atherosclerosis* **2014**, *233* (1), 307−309.

(7) Elliott, H. R.; Tillin, T.; Chaturvedi, N.; Hughes, A. D.; McArdle, W.; Smith, G. D.; Frayling, T. M.; Ebrahim, S.; Relton, C. L. DNA methylation, cardio metabolic risk and type 2 diabetes in south Asians and Europeans. *Clin. Epigenet.* **2013**, *6*, 4.

(8) Hu, R.; Li, G.; Kamijo, Y.; Aoyama, T.; Nakajima, T.; Inoue, T.; Node, K.; Kannagi, R.; Kyogashima, M.; Hara, A. Serum sulfatides as a novel biomarker for cardiovascular disease in patients with end-stage renal failure. *Glycoconjugate J.* **2007**, *24* (9), 565−571.

(9) Lindahl, B. Diagnosis and management of patients with suspected acute myocardial infarction. *Scand. J. Clin. Lab. Invest.* **2005**, *65*, 93−98.

(10) Willcox, B. J.; Abbott, R. D.; Yano, K.; Rodriguez, B. L.; Willcox, D. C.; Curb, J. D. C-reactive protein, cardiovascular disease and stroke: new roles for an old biomarker. *Expert Rev. Neurother.* **2004**, *4* (3), 507−518.

(11) Hunter, C.; Becker, G.; Breite, A.; Anderson, L. Developing peptide MRM-based assays for cardiovascular biomarker proteins in plasma using a hybrid triple quadrupole linear ion trap mass spectrometer. *Mol. Cell. Proteomics* **2005**, *4* (8), S217−S217.

(12) Hulka, B.; Wilcosky, T. Biological markers in epidemiologic research. *Arch. Environ. Health* **1988**, *43* (2), 83.

(13) Bruins Slot, M. H.; van der Heijden, G. J.; Stelpstra, S. D.; Hoes, A. W.; Rutten, F. H. Point-of-care tests in suspected acute myocardial infarction: a systematic review. *Int. J. Cardiol.* **2013**, *168* (6), 5355−5362.

(14) Reichlin, T.; Hochholzer, W.; Bassetti, S.; Steuer, S.; Stelzig, C.; Hartwiger, S.; Biedert, S.; Schaub, N.; Buerge, C.; Potocki, M.; Noveanu, M.; Breidthardt, T.; Twerenbold, R.; Winkler, K.; Bingisser, R.; Mueller, C. Early Diagnosis of Myocardial Infarction with Sensitive Cardiac Troponin Assays. *N. Engl. J. Med.* **2009**, *361* (9), 858−867.

(15) Balboni, I.; Chan, S. M.; Kattah, M.; Tenenbaum, J. D.; Butte, A. J.; Utz, P. J. MULTIPLEXED PROTEIN ARRAY PLATFORMS FOR ANALYSIS OF AUTOIMMUNE DISEASES. *Annu. Rev. Immunol.* **2006**, *24* (1), 391−418.

(16) Kost, G. J.; Tran, N. K.; Tuntideelert, M.; Kulrattanamaneeporn, S.; Peungposop, N. Katrina, the Tsunami, and Point-of-Care TestingOptimizing Rapid Response Diagnosis in Disasters. *Am. J. Clin. Pathol.* **2006**, *126* (4), 513−520.

(17) Spindel, S.; Sapsford, E. K. Evaluation of Optical Detection Platforms for Multiplexed Detection of Proteins and the Need for Point-of-Care Biosensors for Clinical Use. *Sensors* **2014**, *14* (12), 22313.

(18) Martinez-Perdiguero, J.; Retolaza, A.; Bujanda, L.; Merino, S. Surface plasmon resonance immunoassay for the detection of the TNFalpha biomarker in human serum. *Talanta* **2014**, *119*, 492−497.

(19) Morales-Vidal, M.; Boj, P. G.; Quintana, J. A.; Villalvilla, J. M.; Retolaza, A.; Merino, S.; Díaz-García, M. A. Distributed feedback lasers based on perylenediimide dyes for label-free refractive index sensing. *Sens. Actuators, B* **2015**, *220*, 1368−1375.

(20) Jackowski, G. Method and device for diagnosing and distinguishing chest pain in early onset thereof. US5604105B1, 1996/09/05/Application date, 1996.

(21) Washburn, A. L.; Gunn, L. C.; Bailey, R. C. Label-Free Quantitation of a Cancer Biomarker in Complex Media Using Silicon Photonic Microring Resonators. *Anal. Chem.* **2009**, *81* (22), 9499−9506.

(22) Baaske, M.; Vollmer, F. Optical Resonator Biosensors: Molecular Diagnostic and Nanoparticle Detection on an Integrated Platform. *ChemPhysChem* **2012**, *13* (2), 427−436.

(23) Armani, A. M.; Kulkarni, R. P.; Fraser, S. E.; Flagan, R. C.; Vahala, K. J. Label-free, single-molecule detection with optical microcavities. *Science* **2007**, *317* (5839), 783−787.

(24) Shamah, S. M.; Cunningham, B. T. Label-free cell-based assays using photonic crystal optical biosensors. *Analyst* **2011**, *136* (6), 1090−1102.

(25) Cunningham, B. T.; Li, P.; Schulz, S.; Lin, B.; Baird, C.; Gerstenmaier, J.; Genick, C.; Wang, F.; Fine, E.; Laing, L. Label-free assays on the BIND system. *J. Biomol. Screening* **2004**, *9* (6), 481−490.

(26) Chou, T. C.; Doong, R. A. ANYL 222-Gold nanoparticle-based photonic crystal biosensor for tumor markers' detection. *Abstracts of Papers of the American Chemical Society* **2009**, 238.

(27) Homola, J.; Yee, S. S.; Gauglitz, G. Surface plasmon resonance sensors: review. *Sens. Actuators, B* **1999**, *54* (1−2), 3−15.

(28) Koubova, V.; Brynda, E.; Karasova, L.; Skvor, J.; Homola, J.; Dostalek, J.; Tobiska, P.; Rosicky, J. Detection of foodborne pathogens using surface plasmon resonance biosensors. *Sens. Actuators, B* **2001**, *74* (1−3), 100−105.

(29) Haughey, A. M.; McConnell, G.; Guilhabert, B.; Burley, G. A.; Dawson, M. D.; Laurand, N. Organic Semiconductor Laser Biosensor: Design and Performance Discussion. *IEEE J. Sel. Top. Quantum Electron.* **2016**, *22* (1), 6.

(30) Heydari, E.; Buller, J.; Wischerhoff, E.; Laschewsky, A.; Döring, S.; Stumpe, J. Label-Free Biosensor Based on an All-Polymer DFB Laser. *Adv. Opt. Mater.* **2014**, *2* (2), 137−141.

(31) Shopova, S. I.; Rajmangal, R.; Nishida, Y.; Arnold, S. Ultrasensitive nanoparticle detection using a portable whispering gallery mode biosensor driven by a periodically poled lithium-niobate frequency doubled distributed feedback laser. *Rev. Sci. Instrum.* **2010**, *81* (10), 103110.

(32) Retolaza, A.; Martinez-Perdiguero, J.; Merino, S.; Morales-Vidal, M.; Boj, P. G.; Quintana, J. A.; Villalvilla, J. M.; Díaz-García, M. A. Organic distributed feedback laser for label-free biosensing of ErbB2 protein biomarker. *Sens. Actuators, B* **2016**, *223*, 261−265.

(33) Li, Z.; Zhang, Z.; Emery, T.; Scherer, A.; Psaltis, D. Single mode optofluidic distributed feedback dye laser. *Opt. Express* **2006**, *14* (2), 696−701.

(34) Tsutsumi, N.; Ishibashi, T. Organic dye lasers with distributed Bragg reflector grating and distributed feedback resonator. *Opt. Express* **2009**, *17* (24), 21698−703.

(35) Han, S. G.; Lim, J.; Shin, J.; Lee, S. M.; Park, T.; Yoon, J.; Woo, K.; Lee, H.; Lee, W. Optically pumped distributed feedback dye lasing with slide-coated TiO(2) inverse-opal slab as Bragg reflector. *Opt. Lett.* **2014**, *39* (16), 4743−4746.

(36) Katarkevich, V. M.; Rubinov, A. N.; Efendiev, T.; Anufrik, S. S.; Koldunov, M. F. Highly efficient solid-state distributed feedback dye laser based on polymer-filled nanoporous glass composite excited by a diode-pumped solid-state Nd:LSB microlaser. *Appl. Opt.* **2015**, *54* (26), 7962−7972.

(37) Haughey, A. M.; Guilhabert, B.; Kanibolotsky, A. L.; Skabara, P. J.; Burley, G. A.; Dawson, M. D.; Laurand, N. An organic semiconductor laser based on star-shaped truxene-core oligomers for refractive index sensing. *Sens. Actuators, B* **2013**, *185*, 132−139.

(38) Herrnsdorf, J.; Guilhabert, B.; Chen, Y.; Kanibolotsky, A.; Mackintosh, A.; Pethrick, R.; Skabara, P.; Gu, E.; Laurand, N.; Dawson, M. Flexible blue-emitting encapsulated organic semiconductor DFB laser. *Opt. Express* **2010**, *18* (25), 25535−25545.

(39) Liu, X.; Prinz, S.; Besser, H.; Pfleging, W.; Wissmann, M.; Vannahme, C.; Guttmann, M.; Mappes, T.; Koeber, S.; Koos, C.; Lemmer, U. Organic semiconductor distributed feedback laser pixels for lab-on-a-chip applications fabricated by laser-assisted replication. *Faraday Discuss.* **2014**, *174*, 153−164.

(40) Keefe, A. D.; Pai, S.; Ellington, A. Aptamers as therapeutics. *Nat. Rev. Drug Discovery* **2010**, *9* (7), 537−550.

(41) Song, K.-M.; Lee, S.; Ban, C. Aptamers and Their Biological Applications. *Sensors* **2012**, *12* (1), 612.

(42) Lu, M.; Choi, S. S.; Irfan, U.; Cunningham, B. T. Plastic distributed feedback laser biosensor. *Appl. Phys. Lett.* **2008**, *93* (11), 111113.

(43) Tan, Y.; Ge, C.; Chu, A.; Lu, M.; Goldshlag, W.; Huang, J.; Pokriyal, A.; George, S.; Cunningham, B. T. Plastic-based distributed feedback laser biosensors in microplate format. *IEEE Sens. J.* **2012**, *12* (5), 1174−1180.

(44) Swierczewska, M.; Liu, G.; Lee, S.; Chen, X. High-sensitivity nanosensors for biomarker detection. *Chem. Soc. Rev.* **2012**, *41* (7), 2641−2655.

(45) Rozkiewicz, D. I.; Gierlich, J.; Burley, G. A.; Gutsmiedl, K.; Carell, T.; Ravoo, B. J.; Reinhoudt, D. N. Transfer printing of DNA by "click" chemistry. *ChemBioChem* **2007**, *8* (16), 1997−2002.

(46) El-Sagheer, A. H.; Brown, T. Click chemistry with DNA. *Chem. Soc. Rev.* **2010**, *39* (4), 1388−13405.

(47) Obeid, S.; Busskamp, H.; Welte, W.; Diederichs, K.; Marx, A. Interactions of non-polar and "Click-able" nucleotides in the confines of a DNA polymerase active site. *Chem. Commun. (Cambridge, U. K.)* **2012**, *48* (67), 8320−8322.

(48) Timper, J.; Gutsmiedl, K.; Wirges, C.; Broda, J.; Noyong, M.; Mayer, J.; Carell, T.; Simon, U. Surface "click" reaction of DNA followed by directed metalization for the construction of contactable conducting nanostructures. *Angew. Chem., Int. Ed.* **2012**, *51* (30), 7586−7588.

(49) Kashmery, H. A.; Thompson, D. G.; Dondi, R.; Mabbott, S.; Graham, D.; Clark, A. W.; Burley, G. A. SERS enhancement of silver nanoparticles prepared by a template-directed triazole ligand strategy. *Chem. Commun.* **2015**, *51* (65), 13028−13031.

(50) Belton, C., R.; Kanibolotsky Alexander, L.; Kirkpatrick, J.; Orofino, C.; Elmasly Saadeldin, E. T.; Stavrinou Paul, N.; Skabara Peter, J.; Bradley Donal, D. C. Location, Location, Location - Strategic Positioning of 2,1,3-Benzothiadiazole Units within Trigonal Quaterfluorene-Truxene Star-Shaped Structures. *Adv. Funct. Mater.* **2013**, *23* (22), 2792−2804.

(51) Wang, Y.; Tsiminis, G.; Yang, Y.; Ruseckas, A.; Kanibolotsky, A. L.; Perepichka, I. F.; Skabara, P. J.; Turnbull, G. A.; Samuel, I. D. W. Broadly tunable deep blue laser based on a star-shaped oligofluorene truxene. *Synth. Met.* **2010**, *160* (13), 1397−1400.

(52) Kanibolotsky, A. L.; Berridge, R.; Skabara, P. J.; Perepichka, I. F.; Bradley, D. D. C.; Koeberg, M. Synthesis and Properties of Monodisperse Oligofluorene-Functionalized Truxenes: Highly Fluorescent Star-Shaped Architectures. *J. Am. Chem. Soc.* **2004**, *126* (42), 13695−13702.

(53) Mabbott, S.; Thompson, D.; Sirimuthu, N.; McNay, G.; Faulds, K.; Graham, D. From synthetic DNA to PCR product: detection of fungal infections using SERS. *Faraday Discuss.* **2016**, *187* (0), 461−472.

(54) Herrnsdorf, J. *Organic lasers and nanostructred organic films for hybrid integration*; University of Strathclyde: Glasgow, 2012.

(55) Ostatna, V.; Vaisocherova, H.; Homola, J.; Hianik, T. Effect of the immobilisation of DNA aptamers on the detection of thrombin by means of surface plasmon resonance. *Anal. Bioanal. Chem.* **2008**, *391* (5), 1861−1869.

(56) Li, X.; Li, W.; Zhang, S. Chemiluminescence DNA biosensor based on dual-amplification of thrombin and thiocyanuric acid-gold nanoparticle network. *Analyst* **2010**, *135* (2), 332−336.

(57) Li, X.; Xia, J.; Li, W.; Zhang, S. Multianalyte electrochemical biosensor based on aptamer- and nanoparticle-integrated bio-barcode amplification. *Chem. - Asian J.* **2010**, *5* (2), 294−300.

DOI: 10.1021/acs.langmuir.8b01313
Langmuir XXXX, XXX, XXX−XXX